Isolating Weakly and Strongly-Absorbing Classes of Carbonaceous Aerosol: Optical Properties, Abundance and Lifecycle

Final Technical Report for DoE-ASR Grant No. DE-SC0006689

Project Duration: September 2011 – September 2016

Tami C. Bond (Principal Investigator), yark@illinois.edu, 217-244-5277
Mark J. Rood (Co-Investigator), mrood@illinois.edu, 217-333-6963
Nicole Riemer (Co-Investigator), nriemer@illinois.edu, 217-244-2844

Benjamin T. Brem, Francisco C. Mena-Gonzalez, Rishabh Shah, Mariam Fawaz, Jian Tian
(Graduate Student Researchers)

Department of Civil and Environmental Engineering
University of Illinois
205 N. Mathews Ave.,
Urbana, IL 61801, USA

ABSTRACT

The goal of this project was to evaluate climate-relevant properties of carbonaceous particles and the transformations of those particles in the atmosphere, with the purpose of developing lumped classes of carbonaceous particles suitable for use in large-scale models. These climate-relevant properties included light absorption and hygroscopicity. Hygroscopicity is a measure of water affinity, which governs particle growth at humid conditions and absorption and scattering under those conditions. It also controls particles' activation into cloud droplets, which in turn affects cloud albedo and particle removal. This project used laboratory measurements of fresh and aged carbonaceous aerosol, and predictions of properties using a particle-resolved model, to identify sensitivities. The focus in this project was on aerosol from biomass pyrolysis, abbreviated BrC ("brown carbon").

We measured absorption by aerosol from biomass pyrolysis from two sources with very different composition: wood and corn stalk. For both sources, the greatest light absorption occurred at the highest generation temperature, and this maximum absorption was very similar to that of wood-generated aerosol. We suggest that pyrolysis products can be considered surrogates for a wide range of biomass aerosol.

We captured aerosol emitted from biomass pyrolysis on filters and exposed it to ultraviolet radiation, to the atmospheric trace gases ozone, ammonia (NH_3) and nitrogen oxide; and to aqueous saturated salt solutions of ammonium sulfate, ammonium nitrate, sodium chloride and sodium sulfate. Absorption increased, but by only small amounts for all of these treatments, with one exception: after aging with ammonia, absorption increased by almost a factor of four. Absorption increased more at visible wavelengths. We confirmed that a significant change occurred in the aerosol phase, by measuring absorption by suspended particles after aging with NH_3 and finding doubled aerosol absorption. Aging by NH_3 produces a mild increase in the hygroscopicity of BrC, and a greater increase in cloud condensation nucleus activity. Therefore, reactions with NH_3 form compounds that absorb more light than the original aerosol and act as surfactants, increasing the likelihood that these particles will participate in cloud formation.

The particle-resolved model PartMC was enhanced to include additional physical processes. It was calibrated against chamber results, and we needed to account for the non-spherical structure of particle agglomerates, even for ammonium sulfate. We implemented the "volatility basis set" (VBS) framework in the model. The updated PartMC-MOSAIC model was able to simulate gas and aerosol concentrations from the CARES campaign at levels similar to observations.

The PartMC model was used to evaluate plume dynamics affecting CCN activity of biomass burning aerosols early in a plume. Coagulation limits emission of CCN to about 10^{16} per kg of fuel. Co-emitted, semi-volatile organic compounds or emission at small particle sizes can homogenize composition before plume exit, and SVOC co-emission can be the main factor determining plume-exit CCN for hydrophobic or small particles. When externally-mixed, accumulation-mode particles are emitted in the absence of SVOCs, CCN can be overestimated by up to a factor of two. This means that measurements made on aerosol from all phases of combustion gathered into a single chamber may incorrectly estimate CCN properties.

Based on the findings here, we make some recommendations for use in large-scale models: (1) inventories should represent "internally" versus "externally" mixed under certain combustion conditions; (2) consideration of non-spherical particles when coagulation is important for climate-relevant properties near sources; (3) designating organic biomass particles as weakly absorbing; (4) "inherent absorption" and hygroscopicity are not altered with aging by

ozone or ultraviolet light, and inherent absorption is not altered with salt addition, but both cloud activity and absorption are altered by aging with ammonia and could require a separate class in large-scale models.

TABLE OF CONTENTS

1. Introduction 1
2. Objectives and Activities 1
   2.1 Project Objectives 2
   2.2 Other Activities 3
3. Summary of Major Findings 3
   3.1 Measurement: Light Absorption by Biomass Pyrolysis Aerosol 3
   3.2 Measurement: Evaluation of Aging Agents 4
   3.3 Measurement: Aerosol Absorption Increase 4
   3.4 Measurement: Hygroscopic Growth and Cloud Activity 4
   3.5 Modeling: Chamber Aging 4
   3.6 Modeling: Plume Aging 5
   3.7 Modeling: Comparison with Field Studies 5
   3.8 Recommendation of Climate-Relevant Classes 5
4. Publications 6
Additional Citations 7
Appendix A. Aging-Induced Change in Light Absorption of Primary Organic Biomass Pyrolysis Aerosol
Appendix B. Hygroscopic growth and cloud condensation nuclei activity of fresh and chemically-aged organic aerosol from biomass pyrolysis
Appendix C. Light absorption of organic aerosol from pyrolysis of corn stalk
Appendix D. Simulating aerosol chamber experiments with the particle-resolved aerosol model PartMC
Appendix E. A plume-exit approach to determine cloud condensation nuclei activity of aerosols from residential biofuel combustion
Appendix F. Implementation of the volatility basis set (VBS) approach into PartMC-MOSAIC to simulate the chemical aging of primary organic aerosol

1. INTRODUCTION

Primary (directly emitted) particles may be instrumental in determining concentrations of cloud condensation nuclei [*Bauer et al*., 2010] and are responsible for much of the absorption in the atmosphere [*Chung et al.*, 2012]. Large (global and regional) models that simulate aerosol transport and radiative transfer are required to determine the overall effects of aerosols. Carbonaceous and inorganic aerosols form a large fraction of the global aerosol burden. Anthropogenic particles also affect clouds in terms of reflectivity and cloud-droplet activation [*Twomey et al*., 1984; *Mann et al.*, 2014]. Models must include the emission of primary organic particles to explain observed global concentrations of cloud condensation nuclei [*Spracklen et al.,* 2011].

Aerosols that are either absorbing or non-absorbing affect cloud optical properties. Increasing the number of cloud droplets brightens clouds (first indirect effect), and the number of potential CCN depends on complex interactions between primary particles and the reactions forming secondary particles. Generally, adding primary particles increases the first indirect effect [*Lohmann and Feichter,* 2005], while in some models and under some conditions, adding such particles can decrease that cooling [*Bauer et al.,* 2010]. Aerosol absorption can also remove clouds by heating the atmosphere and evaporating droplets, or favor cloud retention by suppressing cloud uplift [*Koch and DelGenio*, 2010]. Clouds also affect aerosols: 80% of carbonaceous aerosols are removed from the atmosphere by wet deposition [e.g. *Koch et al*., 2009]. These removal rates, which affect aerosol lifetime and thus radiative forcing, are one of the major sources of diversity among aerosol models [*Textor et al*., 2006].

The physical and chemical characteristics that govern one atmospheric process, such as growth under humidity, also affect the others, such as light absorption, activation of cloud nuclei, and removal from the atmosphere. For example, coating may increase both light absorption and water affinity. Hygroscopicity and other factors determine which particles are activated as cloud nuclei and ultimately removed from the atmosphere. All these climate-relevant properties depend on the particles' composition, and cannot be examined in isolation [e.g. *Stier et al*., 2006].

2. OBJECTIVES AND ACTIVITIES

The primary goal of this project was to evaluate climate-relevant properties of carbonaceous particles and the transformations of those particles in the atmosphere, with the purpose of developing lumped classes of carbonaceous particles suitable for use in large-scale models. These climate-relevant properties included *light absorption* and *hygroscopicity.* Hygroscopicity is a measure of water affinity, and it governs particle growth at humid conditions and absorption and scattering under those conditions. It also controls particles' activation into cloud droplets, which in turn affects cloud albedo and particle removal. If classes of particles exhibit significantly different climate-relevant behavior, then aerosol representation in climate models could be improved by representing these particles as distinct classes or modes. These differences could be either caused by generation conditions, or initiated during aging in the atmosphere. This project used both *focused laboratory measurements* of climate-relevant properties of fresh and aged carbonaceous aerosol, and *predictions* of climate-relevant properties using a particle-resolved model, to identify sensitivities.

2.1 Project Objectives

Specific objectives identified in the original proposal are listed in the paragraphs below. We incorporated insights gained during analysis of a previous DoE project (DE-FG02-08ER64533), and related work on aging of black carbon funded by other programs [*Fierce et al.*, 2013; *Fierce et al.*, 2015; *Fierce et al.*, 2016] to guide the project focus, and comments on these modifications are also given after each objective.

Because the objectives were met through diverse methods ranging from wet experiments to aerosol experiments to detailed modeling, they are detailed in appendices to this report that parallel journal papers. Findings are summarized in the next section.

Objective 1. Generate fresh and aged aerosols for which the seed aerosol contains specific black or organic carbon material.

The proposal stated that this project was to focus mainly on organic carbon, but would incorporate black carbon aging when appropriate. *Fierce et al.* [2015] showed that aging of black carbon—defined as transition to particles that would activate as cloud nuclei—largely depended on condensation of secondary inorganic aerosol in the atmosphere. Organic carbon aerosol could undergo chemical reactions to produce aging, while black carbon would not; we therefore emphasized aging of organic carbon in this project.

- Generation of organic aerosol from wood pyrolysis is described in the Methods section of Appendix C.

Objective 2. *Measure key climate-relevant properties of aged aerosols: optical properties at high sub-saturated relative humidity (cloud boundaries) and cloud condensation nuclei (CCN) activity.*

- As outlined in the proposal, we first performed "screening" tests to identify the reactions that produced changes in absorption. These tests are discussed in Appendix A.
- Measurements of absorption and scattering for aging agents that increased absorption in the screening tests are also discussed in Appendix A.
- Measurements of hygroscopic growth and CCN activity were conducted with all aging agents. These measurements are described in Appendix B.
- To evaluate the representativeness of our aerosol generated from wood pyrolysis, we compared its absorption with aerosol generated from a completely different biomass source—corn stalk, which is burned in fields and homes in developing countries. This comparison is described in Appendix C.

Objective 3. Enhance a particle-resolved model with additional processes that describe particle aging, and use it to predict spectral absorption and scattering from a variety of emission and processing scenarios.

The particle-resolved model PartMC was used to describe particle aging. During the generation and capture of particles prior to measurement, rapid coagulation and redistribution of semi-volatile material occurred, and these processes had to be included in the model in order to reproduce measured properties. We recognized that these processes would occur not only in any chamber experiments, but in the high concentration of natural emission plumes.

- PartMC required modification to represent coagulation of fractal particles and semi-volatile material. The update required to match the chamber experiments is described in Appendix D.
- We used the model to study how particles evolve in the high concentrations of plumes, an environment likely to modify climate-relevant properties. This investigation is detailed in Appendix E.

4. *Determine climate-relevant classes of particles important for use in models by integrating focused laboratory work with model sensitivity analysis.*

- Following the results provided in Appendices A-E and the summary in the next section of this report, we provide a recommendation of climate-relevant classes in the next section.

5. *Evaluate predictions with comparisons to field data from ASR fixed sites and field programs.*

During most of the project, we evaluated light absorption properties at the particle scale and compared them with microphysical properties observed in field measurements. The goal, however, was to predict macroscale behavior of aerosol in the atmosphere. Until the PartMC model contained all relevant processes, it could not be compared with atmospheric measurements. Semi-volatile aerosol and secondary formation of aerosol are important not only in determining aerosol concentrations but in determining climate-relevant properties.

- The PartMC model was updated to include a Volatility Basis Set representation of semi-volatile and secondary organic aerosol. This modification, and its comparison with CARES campaign data, are discussed in Appendix F.

2.2 Other Activities

Support provided to study the role of primary, light-absorbing particles in the atmosphere and climate system also benefited the Principal Investigator's involvement as lead author on a large assessment paper [*Bond et al.*, 2013]. In addition, the identification of directly-emitted biomass aerosol as the main organic absorber, as well as laboratory-measured properties of that aerosol, was contributed to a global model of light-absorbing emissions [*Lu et al.*, 2015].

3. SUMMARY OF MAJOR FINDINGS

3.1 Measurement: Light Absorption by Biomass Pyrolysis Aerosol

Our previous work has used aerosol from biomass pyrolysis as representative of a large fraction of the organic aerosol in the atmosphere. However, there was a question about whether the wood selected for aerosol generation was representative. We conducted experiments with a very different biomass source, corn stalk, and compared absorption spectra from 360-600 nm. Generation temperatures were chosen to match regimes of thermal degradation. As with wood-generated aerosol, the greatest light absorption occurred at the highest generation temperature, and this maximum absorption was very similar to that of wood-generated aerosol. We conclude that, at least for light absorption, our generation method produces particles that can be considered surrogates for a wide range of biomass aerosol.

3.2 Measurement: Evaluation of Aging Agents

To evaluate possible causes of changes in aerosol absorption, particles from biomass pyrolysis captured on filters was exposed to ultraviolet radiation, to the atmospheric trace gases O_3, NH_3 and NO; and to aqueous saturated salt solutions of $(NH4)_2SO_4$, NH_4NO_3, NaCl and Na_2SO_4. Absorption increased by 15-60% for all of these treatments, with one exception: after aging with ammonia (NH_3), absorption increased by about 275%. This treatment preferentially increased absorption at visible wavelengths, reducing the wavelength dependence of absorption.

Visible absorption by this material is near the detection limit of our measurement method and small in comparison with that of black carbon—about 10% of the absorption per mass. For that reason, an absorption increase of 50% (from k = 0.002 to k = 0.003) was deemed scientifically interesting but less relevant to uncertainties in climate forcing. For that reason, only the NH_3 aging was pursued for the more difficult aerosol-phase optical measurements. O_3 aging was also conducted as a control in which absorption would not change.

3.3 Measurement: Aerosol Absorption Increase

Measuring absorption by suspended particles avoids some of the artifacts of filter-based absorption, but is a more difficult measurement. After aging with NH_3, aerosol absorption doubled. This increase was lower than that observed on filter extracts, but the exposure was also lower than that of the filter experiments.

The change in absorption by biomass pyrolysis aerosol aged with O_3, indicated by the aerosol co-albedo, was similar to the change in absorption in the liquid phase, less than 20%.

3.4 Measurement: Hygroscopic Growth and Cloud Activity

We investigated changes in hygroscopic growth and cloud condensation nucleus (CCN) activity of complex organic carbon particles from biomass pyrolysis after aging dry and wet particles with NH_3 and O_3. We expressed hygroscopic growth using the κ-Köhler parameterization: κ_{GF} for hygroscopic growth and κ_{CCN} for CCN activity. Simple κ-Köhler theory assumes that these two parameters should be the same.

Aging with O_3 has no measurable impact on the κ of OC particles for either hygroscopicity or CCN activity. This aging does delay cloud droplet growth, possibly because gas-phase organic compounds in the aerosol oxidize and condense as films on existing particles.

Aging by NH_3 also increases the κ_{CCN} of OC particles by 72%, suggesting formation of organic acidic groups upon aging. Furthermore, κ_{CCN} is about a factor of three larger than κ_{GF} for this aged aerosol. This finding suggests that surface tension plays a role in activation, and that reaction with NH_3 could form surfactants. We also observed formation of multiple CCN activation modes, consistent with the presence of surfactant.

Particles were aged under both dry and humid conditions. Aerosol water content during the aging period does not affect the final hygroscopicity of particles, implying that aqueous reactions do not play a role in these aging mechanisms. Our results are consistent with previously reported impacts of NH_3 and O_3 aging on the hygroscopicity of organic particles, and confirm them for more complex OC particles.

3.5 Modeling: Chamber Aging

The particle-resolved model PartMC is used for sensitivity studies to assess the response to aging in the atmosphere. For verification, this model was compared against chamber results for coagulating ammonium sulfate particles. Assuming spherical particles led to model results

that were inconsistent with the measurements, so the modeling framework was extended to include the representation of fractal particle structure and wall loss. This introduced five unknown parameters to the governing equation, which were determined by a combination of scanning electron microscopy (SEM) analysis and an objective optimization procedure. The best agreement between model and measurement was obtained for a fractal dimension of 2.3, indicating that the non-spherical structure of the particle agglomerates in the chamber needed to be taken into account.

3.6 Modeling: Plume Aging

The PartMC model was used for a sensitivity study to evaluate plume dynamics that affected CCN activity of biomass burning aerosols in a plume from emission until plume-exit. About 300 PartMC-MOSAIC simulations with varying initial conditions were conducted, covering the range of particle sizes, co-emissions, and mixing states expected in plumes.

Aerosol dynamics affect CCN activity only during the first few seconds of evolution, after which the CCN efficiency reaches a constant value. Coagulation limits emission of CCN to about 10^{16} per kg of fuel. Factors that homogenize CCN behavior among the diverse aerosols in a plume are co-emission of semi-volatile organic compounds (SVOC) or emission at small particle sizes. SVOC co-emission can be the main factor determining plume-exit CCN for hydrophobic or small particles. Hygroscopic particles in the Aitken mode can form CCN through self-coagulation, but have a small effect on the CCN activity of accumulation-mode particles, regardless of composition differences. When externally-mixed, accumulation-mode particles are emitted without SVOCs, application of a hygroscopicity representing the average chemical composition overestimates emitted CCN by up to a factor of two.

Aerosol homogenization can occur at the high concentrations of a plume, but the components must be truly co-emitted, rather than sequentially emitted. This means that measurements that are made on aerosol from all phases of combustion gathered into a single chamber may incorrectly estimate CCN properties of emissions. The experiments in this work isolated individual combustion phases.

3.7 Modeling: Comparison with Field Studies

Because of the importance of secondary organic aerosol in aging, we implemented the "volatility basis set" (VBS) framework in the particle-resolved box model PartMC-MOSAIC. Primary organic aerosol is divided into nine volatility bins and the evaporated gas phase species can undergo further oxidation to form secondary organic aerosols. While most previous studies only focused on the bulk concentration of SOA production, the new model capability uniquely provides particle-level information and mixing state of SOA-containing particles.

The updated PartMC-MOSAIC model was able to simulate gas and aerosol concentrations from the CARES campaign at similar levels compared to the observational data. Moreover, the simulation with the VBS framework showed an additional 2 $\mu g\ m^{-3}$ of secondary organic aerosol, which brought the total OA concentration closer to observed values.

3.8 Final Recommendation: Climate-Relevant Classes for Modeling

In the recommendations below, we recommend treatments for primary particles from biomass sources, which constitute a large fraction of the aerosol in the atmosphere.

1) Based on the findings of the PartMC model applied to the plume-exit approach, we recommend that emission inventories should include a designation of "internally mixed" when primary particles are co-emitted with sufficient semi-volatile material, *or* when primary particles are emitted below a certain size. When particles are emitted sequentially, or in an external mixture and without semi-volatile material, they should be designated as "externally mixed" upon emission. These designations will require attention to separating emissions by combustion phase, when relevant.
2) Based on the chamber verification of PartMC, we recommend that when coagulation is important in altering particle properties under conditions identified by *Fierce et al.* [2013], models should consider the effects of non-spherical particles.
3) Based on the comparison of light absorption from biomass sources, we recommend that all aerosol emitted from biomass be placed into a single classification titled "weakly absorbing" particles. This classification will miss some subtle absorption differences, but these are relatively small compared with absorption by black carbon.
4) Based on the exploration of aging treatments for both hygroscopicity and absorption change, we make the following recommendations for representing "inherent absorption," which we define as light absorption of the native absorbing material rather than absorption caused by particle morphology or mixing state.
   i) Aging with ozone and irradiation with ultraviolet light alters inherent absorption; and aging with ozone causes subtle differences in activation, but not enough to require distinct representation in large-scale models;
   ii) Aging by coagulation of salts to form solutions alters inherent absorption minimally, and the difference in activation can be represented using standard hygroscopic mixing rules;
   iii) Aging with ammonia alters both absorption and hygroscopic properties sufficiently that ammonia-aged particles could require a separate class in large-scale models, and the magnitude of these effects should be evaluated by sensitivity tests using such models.

Naturally, this study has examined only a selected set of the possible material in the atmosphere. We also suggest that other researchers examining changes in light absorption due to reactions, or attribution of cloud condensation nuclei to chemical composition, could evaluate their findings within the framework of climate-relevant classes as we have proposed.

4. PUBLICATIONS

Peer Reviewed Publications: Published/Accepted

Application of the stochastic particle-resolved aerosol model PartMC to chamber experiments, J. Tian, B. Brem, M. West, T. C. Bond, M. J. Rood, N. Riemer, in press at *Aerosol Science and Technology*, March 2017.

Light absorption of organic aerosol from pyrolysis of corn stalk, X. Li, Y. Chen and T. C. Bond, *Atmospheric Environment* 144, 249-256, 2016.

Peer Reviewed Publications: Submitted

Hygroscopic growth and cloud condensation nuclei activity of fresh and chemically-aged biomass-pyrolyzed organic aerosol, R. U. Shah, H. Emamipour, M. J. Rood, and T. C. Bond, submitted to *Aerosol Science and Technology* (currently in revision).

A plume-exit approach to determine cloud condensation nuclei activity of aerosols from residential biofuel combustion, F. Mena, T. C. Bond, N. Riemer, submitted to *Atmospheric Chemistry and Physics* (currently in revision).

Peer Reviewed Publications: In Progress

Aging-Induced Change in Light Absorption of Primary Organic Biomass Pyrolysis Aerosol, M. Fawaz, B. T. Brem, Y. Chen, and T. C. Bond, in preparation for *Journal of Geophysical Research.*

J. Ching, J. Tian, N. Riemer, J. Fast, M. Srivastava, and R. Zaveri. Particle-resolved modeling and measurements of aerosol mixing state during CARES, 2017, in preparation for *Atmospheric Chemistry and Physics.*

Peer Reviewed Publications: Acknowledging DoE as Funding for Related Work

T. C. Bond, S. J. Doherty, D. W. Fahey, P. M. Forster, T. Berntsen, B. J. DeAngelo, M. G. Flanner, S. Ghan, B. Kārcher, D. Koch, S. Kinne, Y. Kondo, P. K. Quinn, M. C. Sarofim, M. G. Schultz, M. Schulz, C. Venkataraman, H. Zhang, S. Zhang, N. Bellouin, S. K. Guttikunda, P. K. Hopke, M. Z. Jacobson, J. W. Kaiser, Z. Klimont, U. Lohmann, J. P. Schwarz, D. Shindell, T. Storelvmo, S. G. Warren, C. S. Zender, Bounding the role of black carbon in the climate system: A scientific assessment, Journal of Geophysical Research-Atmospheres, 118, doi:10.1002/jgrd.50171, 2013.

Lu, Z., D. G. Streets, E. Winijkul, F. Yan, Y. Chen, T. C. Bond, Y. Feng, M. K. Dubey, S. Liu, J. P. Pinto, and G. R. Carmichael, Light Absorption Properties and Radiative Effects of Primary Organic Aerosol Emissions, Environ. Sci. Technol., 49(8), 4868-4877, 10.1021/acs.est.5b00211, 2015.

ADDITIONAL CITATIONS

Bauer, S. E., S. Menon, D. Koch, T. C. Bond, and K. Tsigaridis (2010), A global modeling study on carbonaceous aerosol microphysical characteristics and radiative forcing, *Atmos. Chem. Phys*., 10, 4543-4592.

Chung, C. E., V. Ramanathan, and D. Decremer (2012), Observationally constrained estimates of carbonaceous aerosol radiative forcing, *Proc. Natl. Acad. Sci. U. S. A*., 109(29), 11624-11629, 10.1073/pnas.1203707109.

Fierce, L., T. C. Bond, S. E. Bauer, F. Mena, and N. Riemer (2016), Black carbon absorption at the global scale is affected by particle-scale diversity in composition, *Nature Communications*, *7*, 10.1038/ncomms12361.

Fierce, L., N. Riemer, and T. C. Bond (2013), When is cloud condensation nuclei activity sensitive to particle characteristics at emission?, *J. Geophys. Res.-Atmos.*, *118*(24), 13476-13488, 10.1002/2013jd020608.

Fierce, L., N. Riemer, and T. C. Bond (2015), Explaining variance in black carbon's aging timescale, *Atmos. Chem. Phys.*, *15*(6), 3173-3191, 10.5194/acp-15-3173-2015.

Koch, D., M. Schulz, S. Kinne, C. McNaughton, J. R. Spackman, Y. Balkanski, S. Bauer, T. Berntsen, T. C. Bond, O. Boucher, M. Chin, A. Clarke, N. De Luca, F. Dentener, T. Diehl, O. Dubovik, R. Easter, D. W. Fahey, J. Feichter, D. Fillmore, S. Freitag, S. Ghan, P. Ginoux, S. Gong, L. Horowitz, T. Iversen, A. Kirkevag, Z. Klimont, Y. Kondo, M. Krol, X. Liu, R. Miller, V. Montanaro, N. Moteki, G. Myhre, J. E. Penner, J. Perlwitz, G.

Pitari, S. Reddy, L. Sahu, H. Sakamoto, G. Schuster, J. P. Schwarz, O. Seland, P. Stier, N. Takegawa, T. Takemura, C. Textor, J. A. van Aardenne, and Y. Zhao (2009), Evaluation of black carbon estimations in global aerosol models, *Atmos. Chem. Phys*., 9(22), 9001-9026.

Koch, D., and A. D. Del Genio (2010), Black carbon semi-direct effects on cloud cover: review and synthesis, Atmos. Chem. Phys., 10(16), 7685-7696, 10.5194/acp-10-7685-2010.

Lohmann, U., and J. Feichter (2005), Global indirect aerosol effects: a review, *Atmos. Chem. Phys*., 5, 715-737.

Lu, Z., D. G. Streets, E. Winijkul, F. Yan, Y. Chen, T. C. Bond, Y. Feng, M. K. Dubey, S. Liu, J. P. Pinto, and G. R. Carmichael (2015), Light Absorption Properties and Radiative Effects of Primary Organic Aerosol Emissions, Environ. Sci. Technol., 49(8), 4868-4877, 10.1021/acs.est.5b00211.

Mann, G. W., K. S. Carslaw, C. L. Reddington, K. J. Pringle, M. Schulz, A. Asmi, D. V. Spracklen, D. A. Ridley, M. T. Woodhouse, L. A. Lee, K. Zhang, S. J. Ghan, R. C. Easter, X. Liu, P. Stier, Y. H. Lee, P. J. Adams, H. Tost, J. Lelieveld, S. E. Bauer, K. Tsigaridis, T. P. C. van Noije, A. Strunk, E. Vignati, N. Bellouin, M. Dalvi, C. E. Johnson, T. Bergman, H. Kokkola, K. von Salzen, F. Yu, G. Luo, A. Petzold, J. Heintzenberg, A. Clarke, A. Ogren, J. Gras, U. Baltensperger, U. Kaminski, S. G. Jennings, C. D. O'Dowd, R. M. Harrison, D. C. S. Beddows, M. Kulmala, Y. Viisanen, V. Ulevicius, N. Mihalopoulos, V. Zdimal, M. Fiebig, H. C. Hansson, E. Swietlicki, and J. S. Henzing (2014), Intercomparison and evaluation of global aerosol microphysical properties among AeroCom models of a range of complexity, *Atmos. Chem. Phys.*, *14*(9), 4679-4713, 10.5194/acp-14-4679-2014.

Spracklen, D. V., K. S. Carslaw, U. Poschl, A. Rap, and P. M. Forster (2011), Global cloud condensation nuclei influenced by carbonaceous combustion aerosol, *Atmos. Chem. Phys.*, *11*(17), 9067-9087, 10.5194/acp-11-9067-2011.

Stier, P., J. Feichter, S. Kloster, E. Vignati, and J. Wilson (2006), Emission-induced nonlinearities in the global aerosol system: results from the ECHAM4-HAM aerosol-climate model, *J. Clim.*, *19*, 3845-3862.

Textor, C., M. Schulz, S. Guibert, S. Kinne, Y. Balkanski, S. Bauer, T. Berntsen, T. Berglen, O. Boucher, M. Chin, F. Dentener, T. Diehl, R. Easter, H. Feichter, D. Fillmore, S. Ghan, P. Ginoux, S. Gong, A. Grini, J. Hendricks, L. Horowitz, P. Huang, I. Isaksen, T. Iversen, S. Kloster, D. Koch, A. Kirkevåg, J. E. Kristjansson, M. Krol, A. Lauer, J. F. Lamarque, X. Liu, V. Montanaro, G. Myhre, J. Penner, G. Pitari, S. Reddy, Ø. Seland, P. Stier, T. Takemura, and X. Tie (2006), Analysis and quantification of the diversities of aerosol life cycles within AeroCom, *Atmos. Chem. Phys*., 6, 1777-1813.

Twomey, S. A., M. Piepgrass, and T. L. Wolfe (1984), An assessment of the impact of pollution on global cloud albedo, *Tellus*, B36, 356-366.

Appendix A.

Aging-Induced Change in Light Absorption of Primary Organic Biomass Pyrolysis Aerosol

M. Fawaz, B. T. Brem, Y. Chen, M. J. Rood, and T. C. Bond

1. Introduction

Carbonaceous aerosols are abundant in the atmosphere. They are emitted from urban sources, residential sources, and biogenic sources. Carbonaceous aerosols are categorized into primary organic carbon, secondary organic carbon, and black carbon based on their chemical composition and their origin. Black carbon is a strong absorber of light [*Ramanathan and Carmichael*, 2008]. While secondary organic carbon absorb light after atmospheric processing [*Liu et al.* 2016, *Lambe et al.* 2013], primary organic carbon can absorb up to 14% of solar radiation in the visible range [*Kirchstetter and Thatcher*, 2012]. Field campaigns found evidence of BrC absorption from particles collected from regions with biomass burning [*Hand et al*., 2005; *Alexander et al*., 2008; *Adachi and Busek*, 2011]. The absorbing particles in the organic aerosol family have been termed "brown carbon," which we abbreviate as BrC to distinguish it from black carbon.

Radiative forcing studies established the need to include the contribution of brown carbon in forcing models. Including brown carbon absorption into direct radiative forcing models causes a decrease in radiative forcing and shifts the role of BrC from cooling to warming [*Lu et al*. 2015]. *Feng et al.* [2013] found that the radiative forcing of organic aerosols changes from -0.08 W/m2 to +0.025 W/m^2 when BrC absorption is included, thus predicting a climate warming effect instead of a cooling effect. The accurate representation of BrC in radiative transfer models depends on estimates of BrC absorption. Values characterizing absorption strength and spectral dependence also been applied to attribute absorbance of aerosol in the atmosphere to brown carbon [*Arola et al*. 2011].

Optical properties of freshly emitted BrC have been measured [*Hoffer et al*., 2015; *Chen and Bond*, 2010; *Saleh et al*., 2013; *Dinar et al*., 2008]. Laboratory studies measured absorption in the visible range for organic carbon emitted from biomass burning [*Chakarabarty et al.*, 2010; *Chen and Bond*, 2010; *Hoffer et al.*, 2016]. Once emitted, brown carbon may remain in the atmosphere for several days, undergoing physical and chemical transformations. Studies examined the effect of photochemical aging of brown carbon on absorption [*Zhao et al*. 2015, *Saleh et al.*, 2013; *Zhong and Jang*, 2013], where UV radiation decreases absorption due to the loss of chromophores [*Lee et al*., 2014]. In addition, there have been reports on the effect of the morphology of brown carbon on the optical properties [*Lack and Cappa*, 2010; *Saleh et al*. 2014]. Based on the assumption that brown carbon is formed on a black carbon seed, BrC absorption has been parameterized as a function of BC content [*Pokhrel et al*., 2016; *Lu et al*., 2015]. There is a need to study the coupled effect of physical and chemical processes on the light absorption of brown carbon.

Chemical processes influence optical properties. Aging of aerosols in the atmosphere may introduce compounds or reactants that change the hygroscopicity of the particles by making it more hydrophilic or more hydrophobic. Nitrated and aromatic compounds have been identified as likely absorbers [*Jacobson*, 1999; *Sun et al.*, 2007]. *Mohr et al.* [2013] observed an increase in absorption in brown carbon particles containing nitrate phenol groups. Atmospheric oxidation of organic aerosol increases the oxygen content of the particles and increases their hygroscopicity [*Jimenez* et al., 2009]. Atmospheric processing of mixed organic aerosol with OH, NO, and O_2 incorporates chromophores and is expected to enhance light absorption [*Ellison et al*., 1999].

Reported absorptive properties of BrC are summarized in Table 1. Particles' interaction with light is governed by their size and refractive index, $m = n + i\ k$, where n is the real part mainly relating to light scattering, and k is the imaginary part which primarily governs absorption. Previously observed k values for BrC aerosol range from 0.002 at λ = 532 nm of nighttime HULIS [*Hoffer et al*., 2006] to 0.270 at λ = 550 nm for BrC spheres [*Alexander et al.*, 2008]. The reason for this wide range is not entirely clear, but indicates that BrC absorption is likely dependent on the type of emission source and atmospheric processing.

The absorption Ångström exponent ($\mathring{a}_a$) describes the wavelength dependence of absorption according to the equation below:

$$\mathring{a}_a = \frac{-\ln\left(b_{ap}(\lambda_1)/b_{ap}(\lambda_2)\right)}{\ln\left(\lambda_1/\lambda_2\right)} \qquad (1)$$

where b_{ap} is the absorption coefficient of aerosol. Values of $\mathring{a}_a$ are also summarized in Table 1. Different emission sources and atmospheric processing may also explain the spread in $\mathring{a}_a$ values ranging from 1.5 [*Alexander et al.*, 2008] to 16.7 [*Chakrabarty et al.*, 2010].

The objective of this study is to evaluate the effects of aging agents or processes commonly found in the atmosphere on the absorption of primary BrC aerosol, first identifying the agents that could cause strong BrC aerosol absorption.

2. Methods and Data Analysis

We determined mass-specific properties of brown carbon (BrC) emitted from biomass pyrolysis and exposed to aging agents using filter capture followed by extraction and measurement in the liquid phase. To investigate the change of optical properties under high relative humidity (RH) conditions we used the difference between extinction and scattering. Figure 1 is a schematic of the overall setup of BrC generation from biomass pyrolysis, including collection on filters and optical measurements.

2.1.1 Aerosol Generation

A temperature-controlled wood pyrolysis reactor was operated to generate primary BrC aerosol. Nitrogen (N_2) sheath flow produced anoxic conditions in the reactor, as expected to occur in the middle of a wood piece [*Evans and Milne*, 1987]. These conditions allowed for pyrolysis that generated light absorbing BrC aerosol, while also preventing flaming and the production of elemental carbon. This wood pyrolysis reactor was previously used by *Chen and Bond* [2010] and *Brem et al.* [2012]. A proportional integral differential (PID) controller controlled the reactor temperature within 10 ˚C. Individual 2 x 2 x 2 cm (length x width x height)

oak wood blocks were pyrolyzed for 7 minutes at 425 ˚C. Three woodblocks were pyrolyzed sequentially per run. The generated aerosol was sampled 4 cm above the reactor chimney at a flow rate of 3.75 L min^{-1}. The annular dilution probe diluted the sample further with particle-free dry air to a 7:1 volume dilution ratio. Particles larger than 1 μm were removed with a two stage Berner type impactor downstream of the dilution probe.

2.1.2 Filter Exposure Experiments

The purpose of exposing particles captured on filters was to determine the aging processes that might have significant effects on absorption before committing to the more challenging measurements on suspended particles. Two parallel 47 mm filter holders (URG-2000-30RAF, URG Corp.) containing two quartz fiber filters (Tissuquartz 2500, Pall Inc.) were used to collect the aerosol particle mass. Quartz filters for collection were baked at 550 ºC in a muffle furnace for four hours and stored in petri dishes lined with baked aluminum foil prior to sampling. The filter collection flow rate was set to 8 L min^{-1}. The rest of the diluted aerosol flow (14 L min^{-1}) bypassed the sampling system. Air flow rates were checked and adjusted by comparing them to a primary standard airflow calibrator (Gilian Gilibrator, Sensidyne Inc.). At the end of the sampling period, the filters were returned to the dishes immediately and stored in a freezer until further usage.

Three types of aging agent treatments were applied to the BrC aerosol: filter punches were exposed to ultraviolet (UV) radiation; entire filters were exposed to the atmospheric trace gases O_3, NH_3 and NO; and aqueous saturated salt solutions of $(NH_4)_2SO_4$, NH_4NO_3, NaCl and Na_2SO_4 were added to filter punches.

2.1.2.1 Ultraviolet Radiation

Two filter punches with an area of 1 cm^2 were placed in a petri dish with the cover removed. A low-pressure mercury arc lamp (CE-10-C, American UV Inc.) was installed 15 cm above the petri dish. One filter punch was covered with a stainless-steel mask to shield it from the 254-nm irradiation of the UV lamp, but allowing similar exposure conditions in terms of temperature and relative humidity. The entire setup was operated in an airtight stainless steel vessel that was purged with 20 L min^{-1} of either dry ultra-zero air or laboratory grade N_2 (purity 5.0). The UV exposure for both the air and N_2 experiments was 5 hours. After exposure both the UV exposed and unexposed punches were extracted and analyzed.

2.1.2.2 Atmospheric Trace Gases

Trace gas experiments were performed by exposing the BrC filter samples to gas flows of O_3, NH_3 and NO. Concentrations much higher than those found in the atmosphere were used in order to determine whether the treatments had any effect. A corona discharge O_3 generator (Model G1-L, PCI Ozone Corp) generated 8% O_3 by mass from oxygen (purity 5.0) at a flow rate of 1 L min^{-1}. The filter holder was connected directly to the O_3 generator for an exposure time of 15 minutes.

Pressurized tanks of anhydrous NH_3 (purity 5.0) and 1000 ppm_v NO balanced with N_2 were the aging agents for the two-other atmospheric trace gas screening experiments. For both experiments, the filter holders were connected to the gas using a variable area flow meter (Rota meter, MMA-21, Dwyer Instruments) upstream for gas flow control. The flow and exposure times for the NH_3 experiment were 1 L min^{-1} and 15 minutes, respectively and 1 L min^{-1} and 120

minutes, respectively for the NO experiment. After all gas screening experiments the treated BrC aerosol mass was extracted from a 1 cm^2 filter punch and analyzed.

2.1.2.3 Saturated Salt Solutions

Two ml of saturated nanopure water solutions of 7 mol L^{-1} $(NH_4)_2SO_4$, 25 mol L^{-1} NH_4NO_3, 7 mol L^{-1} NaCl and 2 mol L^{-1} Na_2SO_4 were added to individual 1 cm^2 BrC loaded filter punches in individual 10 mL vials. The individual vials were closed and left under dark conditions for 12 hours before the treated aerosol mass was extracted and analyzed.

2.1.2.4 Filter Extraction and Absorbance Measurements

Extraction of the filter mass was performed with methanol (A.C.S. certified, Fisher Scientific Inc.). Methanol has been found previously to extract 92 to 98% of pyrolysis OC aerosol mass from quartz filters [*Chen and Bond*, 2010]. The filter punch and 4 mL of solvent were sonicated for 1 hour in an ultrasonic bath (Model 8892, Cole Parmer Inc). For the saturated salt solution experiments 2 mL of methanol were directly added to the salt solution containing the filter punch. After the first sonication, the extracts were kept under dark conditions at room temperature for 20 hours to let the solution reach equilibrium, and sonicated again for an additional hour. After the second sonication, the extracts were filtered with a 0.2 μm pore size syringe filter (Anotop 10, Whatman Inc.) to remove filter fragments and impurities so the BrC solutions could be analyzed in a spectrophotometer.

The absorbance of the aerosol extracts was measured using a spectrophotometer (Shimadzu, UV-2401) for wavelength spectra ranging from 360 to 600 nm. The instrument was operated in spectrum mode at a wavelength resolution of 0.5 nm. The extracts were analyzed in closed quartz cuvettes (29-SOG-10, Starna Cells Inc.) with 1 cm path lengths and 1.4 ml volume. Each spectrum was determined relative to a reference cuvette which contained the solvent of extraction.

2.1.2.5 Organic Carbon Mass Measurements

The mass of organic carbon in the aerosol extracts was determined using the thermal-optical-transmittance (TOT) method. 30 μL of extract were pipetted onto a blank (previously analyzed) 1 cm^2 quartz filter punch. The wet punch was dried for 30 minutes in a fume hood. Contamination in the methanol or from drying was less than 3% of the collected OC, as determined by extracting and drying blank quartz filters initially containing 30 μL of methanol with the same procedure. After the drying the filter punches were analyzed with a thermo-optical OC/EC analyzer (Sunset Laboratory, Tigard, OR). The instrument was operated according to the procedure described by *Subramanian et al.* [2009] with a temperature profile based on NIOSH Method 5040 [*NIOSH*, 2003].

2.1.3 Aerosol measurements

OC aerosol was generated by pyrolysis of oak wood biomass. Pyrolysis was controlled inside a temperature-controlled reactor [*Chen and Bond*, 2010]. The resulting OC aerosol was sampled with a diluting, porous-tube probe for 30 s and was directed to a 208 L stainless steel mixing chamber. Clean air for dilution was filtered with a high efficiency particulate air filter, a silica gel column and an NH_3 adsorbent column. A fan inside the chamber induced mixing of aerosol. Prior to OC injection, the chamber was purged with clean air to remove any residual

particles and gases from the previous test. Particle concentration inside the chamber was measured less than 5 cm^{-3} with a condensation particle counter (CPC, TSI 3010) before each test.

We used an accelerated aging process similar to *Rudich et al*. (2007) to simulate aging under atmospheric conditions. Two atmospheric trace gases were used for the aging of the particles are ammonia gas and ozone gas, at two concentrations. Ammonia gas (NH3) concentrations were 10 ppmv and 875 ppmv and particles were exposed to the gas for 10 minutes. Exposing BrC to 10 ppmv for ten minutes is equivalent to a 9 day exposure to 8 ppbv of ammonia. The concentrations of ozone used were 0.1 and 0.3 ppmv. Concentrations of O_3 were maintained throughout the 2-hour experiment, making the concentration equivalent to 35 ppb for 6 and 18 hours in the atmosphere. For further details on the aging process, refer to Shah et al. (2017).

We measure the effect of the coupled chemical and physical processes on BrC absorption using the difference method described and used in *Brem et al*. [2012]. Absorption is measured at three wavelengths (360nm, 440nm, and 660nm). The particles first pass through a short path extinction cell (SPEC) originally designed by *Virkkula et al.* [2005], which measures extinction at high RHs. The gas stream then passes through a modified TSI nephelometer (TSI 3563) which measures particle scattering. Absorption is calculated by subtracting the extinction signal from the scattering signal. Experiments were first performed with ammonium sulfate to match extinction and scattering for non-absorbing aerosol.

2.1.4 Data Analysis

We distinguish between absorption coefficient measured in solutions (α) and absorption coefficient of aerosols (b_{ap}). Both values can be reported with normalization to the concentration of organic material, giving absorption per mass (α/ρ) in the bulk solution and mass absorption cross-sections (*MAC*) for aerosol.

While both α/ρ and *MAC* have the same units ($m^2\ g^{-1}$), they cannot be compared directly, because *MAC* includes the effect of particle shape and size on interaction with light. From α/ρ, the imaginary part of the refractive index k can be derived, as described below. It can then be used in combination with the real part, n, in Mie-Lorentz or other theories to calculate absorption by suspended particulate matter. The intrinsic difference between α and b_{ap}, or α/ρ and b_{ap}, also means that absorption Ångström exponents calculated from solutions or from suspended aerosols must differ.

2.1.4.1 Filter Collection

Absorption of material extracted from filters is reported in terms of absorption cross-section divided by organic carbon density (α/ρ). This approach has been used by *Chen and Bond* [2010]. The α/ρ values are calculated from spectroscopic data according to:

$$\frac{\alpha}{\rho}(\lambda) = \frac{A(\lambda)}{cL}\ln(10) \qquad (2)$$

where A is the measured absorbance by the spectrometer measured at the wavelength λ, L is the optical path length of the cuvette used (1 cm) and c is the concentration of the organic carbon in the solution determined by the OC/EC analysis.

The imaginary part k of the refractive index was calculated from α/ρ values with the following equation:

$$k(\lambda) = \frac{\alpha}{\rho}(\lambda) \times \frac{\rho \times \lambda}{4\pi} \quad (3)$$

The value of BrC density (ρ) was assumed to be 1.2, a commonly used density for OC [*e.g. Turpin and Lim*, 2001].

Values of $å_a$ were determined according to Equation (1), using a linear regression of ln(α/ρ) versus ln(λ).

2.1.4.2 Optical Properties

The complete corrections for the extinction and scattering signals are discussed in Brem et al. (2012). The corrections include nephelometer truncation, purge air dilution, and change in temperature. The effect on optical properties is presented here as the single scattering albedo, defined as:

$$SSA = \frac{b_{sp}}{b_{sp} + b_{ap}} \quad (4)$$

where b_{sp} is the aerosol scattering coefficient. A measure of absorption is the co-albedo, or one minus the single scattering albedo. This value is 0 if there is no absorption, and 1 if the aerosol is purely absorbing.

2.2 RESULTS AND DISCUSSION

2.2.1 Exposure on Filters

2.2.1.1 Exposure to Ultraviolet Light

Absorption change due to UV exposure, in absolute values and percentage change, are shown in Figure 2. The absorption per mass of the BrC that was not exposed to UV radiation differs less than 9% from the untreated BrC, indicating that the purging of the vessel with dry air and N_2 had little effect on the absorption per mass. The absorption per mass for the UV-exposed BrC was up to 11% lower when the vessel was purged with N_2 compared to air, but this difference lies within experimental uncertainty.

The change in absorption per mass after UV radiation increased at greater wavelengths, so the absorption Ångstrom exponent was reduced (last column of Table 2). The value of $å_a$ decreased from 8.22 for the untreated BrC to 7.09 and 7.16 for the UV-exposed BrC in air and N^2, respectively. All R^2 values in the $å_a$ determination were greater than 0.99.

2.2.1.2 Exposure to Gases

The absorption spectra and percentage changes for BrC filters exposed to gaseous NH_3, O_3, and NO are presented in Figure 3, and the changes are summarized in Table 2. All three gaseous agents increase the absorption per mass of the treated BrC. The smallest change in absorption occurred for the BrC treated with O_3. The change in absorption per mass for the O_3

exposure experiment shows a slight wavelength dependence, with a constant increase ranging from 14% to 26% over the spectral range evaluated. This increase in absorption per mass with increasing wavelength results in a lower $å_a$ value of 6.71 for the O_3 treated BrC, in contrast to the $å_a$ value of 8.02 of the untreated BrC.

The BrC treated with NO is also more absorbing than the untreated BrC, but the change occurs preferentially at shorter wavelengths. This wavelength-dependent change in absorption per mass causes an increased $å_a$ value of 8.77 (Table 1) for the NO-treated BrC. NO is the only aging agent that increased the absorption Ångstrom exponent.

Exposure to NH_3 affects the BrC absorption the most of all aging agents tested. The NH_3 treatment caused an absorption change of up to 300% (λ = 600 nm), and the change was greater at longer wavelengths than at shorter wavelengths. The $å_a$ value for BrC treated with NH_3 decreased from 8.02 to 6.88.

NH_3 reactions with limonene have been found in previous studies to form absorbing secondary OC aerosol at visible wavelengths [*Updyke et al.*, 2012]. The initial step in the browning reaction was proposed to be the reaction between carbonyl groups in the SOA molecules with ammonia that forms chromophores which are conjugated nitrogen-containing species [*Bones and Phillips*, 2009; *Laskin et al.*, 2010; *Nguyen et al.*, 2012] allowing n - π^* transitions causing increased absorption. Such reactions might also occur for the complex primary BrC from biomass pyrolysis that contain carbonyl groups.

2.2.1.3 Exposure to Saturated Salt Solutions

The change in absorption per mass for the experiments in which saturated salt solutions were deposited onto filters is presented in Figure 4. The addition of saturated aqueous solutions of $(NH_4)_2SO_4$, NH_4NO_3, NaCl and Na_2SO_4 simulates mixing that would occur at high relative humidities in ambient air. Mixing with salts increases the absorption per mass of the treated BrC at wavelengths above 480 nm. The greatest change in absorption was +105% at a wavelength around 600 nm, but the absolute changes in absorption per mass were small and the changes in absorption per mass caused by the different salts are not distinguishable from each other. The increase in absorption per mass for all aqueous salt solution treatments decreases $å_a$ (Table 2).

2.2.2 Absorption by particles

Measurements of absorption by particles suspended in air (aerosol) were done following two aging treatments: NH_3 and O_3. Visible absorption by this BrC is small in comparison with that of black carbon—about 1% of the absorption per mass. For that reason, absorption increases of 50% (from k = 0.002 to k = 0.003) were deemed scientifically interesting but less relevant to uncertainties in climate forcing. NH_3 was selected because it produced the greatest change in absorption that could cause a significant change in climate-relevant properties. O_3 was chosen because it is a common atmospheric constituent that produced little change even at very high concentrations relative to those in the atmosphere.

Figure 5 shows the change of SSA at 470 nm (blue) and 530 nm (green) for aging with O_3 and NH_3, each at two concentrations. Because absorption is calculated by subtracting the extinction signal from the scattering signal, uncertainty in the single-scattering albedo was

significant—about 0.01 (Figure 5). This uncertainty was mainly caused by drift in the zero signal of the extinction cell required before and after each experiment.

SSA at the blue wavelength decreased from 0.95 to 0.88 for the treatment with the highest concentration of ammonia, a 90% increase in absorption. SSA at the green wavelength decreased from 0.94 to 0.89 with this treatment, approximately a doubling of absorption; both increases were greater than the uncertainty. While these increases are smaller than the 275% observed for aging in the filter experiments, the concentrations used in aerosol aging are also much lower than the pure ammonia used for the filter aging. SSA also decreased, by a lower amount, when a lower concentration of ammonia (10 ppm) was used for aging.

Aging with the higher concentration of ozone did not cause a difference in SSA greater than the uncertainty of the measurement, consistent with the filter-aging measurements. The lower ozone concentration appeared to slightly increase the SSA or decrease absorption, in contrast to the filter-aging experiments.

3. Summary

Aerosol from biomass pyrolysis was collected on filters and exposed to ultraviolet light, reactive gases and aqueous solutions of salts. After exposure, the absorption spectra of extracts was measured. The measured values of refractive index were in the same range of values calculated by Chakrabarty et al. (2010) for the class of brown carbon called tar balls. Aging with NH_3 increased absorption by a factor of more than three. The other treatments increased absorption by 15-50%; no treatments decreased absorption, even irradiation with UV light. In all cases, the absorption Ångstrom exponent decreased, meaning that the absorption increase preferentially occurred at longer wavelengths.

Aging with ammonia and ozone was applied to suspended particles to confirm that the phenomena appearing, or not appearing, on filter-collected aerosol would occur in the atmosphere. Absorption by particles reacting with ammonia doubled at high concentrations of the reagent, and absorption by particles exposed to ozone changed negligibly, agreeing with the filter measurements.

REFERENCES

Adachi, K., and P. R. Buseck (2011), Atmospheric tar balls from biomass burning in Mexico, *Journal of Geophysical Research: Atmospheres*, *116*.

Alexander, D. T. L., P. A. Crozier, and J. R. Anderson (2008), Brown carbon spheres in East Asian outflow and their optical properties, *Science*, *321*, 833-836.

Arola, A., G. Schuster, G. Myhre, S. Kazadzis, S. Dey, and S. N. Tripathi (2011), Inferring absorbing organic carbon content from AERONET data, *Atmospheric Chemistry and Physics*, *11*, 215-225.

Bones, D. L., and L. F. Phillips (2009), Photolysis in aqueous aerosols: 300 nm yields of Fe2+ from a ferrioxalate actinometer and of OH radical from nitrate ions, *Physical Chemistry Chemical Physics*, *11*(26), 5392-5399.

Brem, B. T., F. C. Mena Gonzalez, S. R. Meyers, T. C. Bond, and M. J. Rood (2012), Laboratory-measured optical properties of inorganic and organic aerosols at relative humidities up to 95\%, *Aerosol Science and Technology*, *46*(2), 178-190.

Chakrabarty, R., H. Moosmüller, L.-W. Chen, K. Lewis, W. Arnott, C. Mazzoleni, M. Dubey, C.

Wold, W. Hao, and S. Kreidenweis (2010), Brown carbon in tar balls from smoldering biomass combustion, *Atmospheric Chemistry and Physics*, *10*(13), 6363-6370.

Chen, Y., and T. Bond (2010), Light absorption by organic carbon from wood combustion, *Atmospheric Chemistry and Physics*, *10*(4), 1773-1787.

Dinar, E., A. A. Riziq, C. Spindler, C. Erlick, G. Kiss, and Y. Rudich (2008), The complex refractive index of atmospheric and model humic-like substances (HULIS) retrieved by a cavity ring down aerosol spectrometer (CRD-AS), *Faraday Discussions*, *137*, 279-295.

Ellison, G. B., A. F. Tuck, and V. Vaida (1999), Atmospheric processing of organic aerosols, *Journal of Geophysical Research: Atmospheres*, *104*, 11633-11641.

Evans, R. J., and T. A. Milne (1987), Molecular characterization of the pyrolysis of biomass. 1. Fundamentals, *Energy Fuel; 1*(2).

Feng, Y., V. Ramanathan, and V. Kotamarthi (2013), Brown carbon: a significant atmospheric absorber of solar radiation?, *Atmospheric Chemistry and Physics*, *13*(17), 8607--8621.

Hand, J. L., W. C. Malm, A. Laskin, D. Day, T.-B. Lee, C. Wang, C. Carrico, J. Carrillo, J. P. Cowin, J. Collett, and others (2005), Optical, physical, and chemical properties of tar balls observed during the Yosemite Aerosol Characterization Study, *Journal of Geophysical Research: Atmospheres*, *110*.

Hoffer, A., A. Gelencsér, M. Blazsó, P. Guyon, P. Artaxo, and M. Andreae (2006), Diel and seasonal variations in the chemical composition of biomass burning aerosol, *Atmospheric Chemistry and Physics*, *6*(11), 3505-3515.

Hoffer, A., A. Tóth, I. Nyirő-Kósa, M. Pósfai, and A. Gelencsér (2016), Light absorption properties of laboratory-generated tar ball particles, *Atmospheric Chemistry and Physics*, *16*, 239-246.

Jacobson, M. Z. (1999), Isolating nitrated and aromatic aerosols and nitrated aromatic gases as sources of ultraviolet light absorption, *Journal of Geophysical Research: Atmospheres*, *104*(D3), 3527-3542.

Jimenez, J. L., M. R. Canagaratna, N. M. Donahue, A. S. H. Prevot, Q. Zhang, J. H. Kroll, P. F. DeCarlo, J. D. Allan, H. Coe, N. L. Ng, and others (2009), Evolution of organic aerosols in the atmosphere, *Science*, *326*, 1525-1529.

Kirchstetter, T., and T. Thatcher (2012), Contribution of organic carbon to wood smoke particulate matter absorption of solar radiation, *Atmospheric Chemistry and Physics*, *12*(14), 6067-6072.

Lack, D. A., and C. D. Cappa (2010), Impact of brown and clear carbon on light absorption enhancement, single scatter albedo and absorption wavelength dependence of black carbon, *Atmospheric Chemistry and Physics*, *10*, 4207-4220.

Lambe, A. T., C. D. Cappa, P. Massoli, T. B. Onasch, S. D. Forestieri, A. T. Martin, M. J. Cummings, D. R. Croasdale, W. H. Brune, D. R. Worsnop, and others (2013), Relationship between oxidation level and optical properties of secondary organic aerosol, *Environmental science & technology*, *47*, 6349-6357.

Laskin, J., A. Laskin, P. J. Roach, G. W. Slysz, G. A. Anderson, S. A. Nizkorodov, D. L. Bones, and L. Q. Nguyen (2010), High-resolution desorption electrospray ionization mass spectrometry for chemical characterization of organic aerosols, *Analytical Chemistry*, *82*(5), 2048-2058.

Lee, H. J., P. K. Aiona, A. Laskin, J. Laskin, and S. A. Nizkorodov (2014), Effect of solar radiation on the optical properties and molecular composition of laboratory proxies of

atmospheric brown carbon, *Environmental science \& technology*, *48*(17), 10217-10226.
Liu, C., C. E. Chung, F. Zhang, and Y. Yin (2016), The colors of biomass burning aerosols in the atmosphere, *Scientific Reports*, *6*.
Lu, Z., D. G. Streets, E. Winijkul, F. Yan, Y. Chen, T. C. Bond, Y. Feng, M. K. Dubey, S. Liu, J. P. Pinto, and others (2015), Light absorption properties and radiative effects of primary organic aerosol emissions, *Environmental Science & Technology, 49*(8), 4868-4877.
Mohr, C., F. D. Lopez-Hilfiker, P. Zotter, A. S. H. Prevot, L. Xu, N. L. Ng, S. C. Herndon, L. R. Williams, J. P. Franklin, M. S. Zahniser, and others (2013), Contribution of nitrated phenols to wood burning brown carbon light absorption in Detling, United Kingdom during winter time, *Environmental Science & Technology*, *47*, 6316-6324.
Nguyen, T. B., P. B. Lee, K. M. Updyke, D. L. Bones, J. Laskin, A. Laskin, and S. A. Nizkorodov (2012), Formation of nitrogen-and sulfur-containing light-absorbing compounds accelerated by evaporation of water from secondary organic aerosols, *Journal of Geophysical Research: Atmospheres*, *117*(D1).
Pokhrel, R. P., N. L. Wagner, J. M. Langridge, D. A. Lack, T. Jayarathne, E. A. Stone, C. E. Stockwell, R. J. Yokelson, and S. M. Murphy (2016), Parameterization of single-scattering albedo (SSA) and absorption Ångström exponent (AAE) with EC/OC for aerosol emissions from biomass burning, *Atmospheric Chemistry and Physics*, *16*(15), 9549--9561.
Ramanathan, V., and G. Carmichael (2008), Global and regional climate changes due to black carbon, *Nature geoscience*, *1*, 221-227.
Russell, P. B., R. W. Bergstrom, Y. Shinozuka, A. D. Clarke, P. F. DeCarlo, J. L. Jimenez, J. M. Livingston, J. Redemann, O. Dubovik, and A. Strawa (2010), Absorption Angstrom Exponent in AERONET and related data as an indicator of aerosol composition, *Atmospheric Chemistry and Physics*, *10*, 1155-1169.
Saleh, R., C. J. Hennigan, G. R. McMeeking, W. K. Chuang, E. S. Robinson, H. Coe, N. M. Donahue, and A. L. Robinson (2013), Absorptivity of brown carbon in fresh and photo-chemically aged biomass-burning emissions, *Atmospheric Chemistry and Physics*, *13*, 7683-7693.
Saleh, R., E. S. Robinson, D. S. Tkacik, A. T. Ahern, S. Liu, A. C. Aiken, R. C. Sullivan, A. A. Presto, M. K. Dubey, R. J. Yokelson, and others (2014), Brownness of organics in aerosols from biomass burning linked to their black carbon content, *Nature Geoscience*, *7*(9), 647--650.
Soni, K., S. Singh, T. Bano, R. Tanwar, S. Nath, and B. Arya (2010), Variations in single scattering albedo and Angstrom absorption exponent during different seasons at Delhi, India, *Atmospheric Environment*, *44*(35), 4355--4363.
Subramanian, R., T. C. Bond, W. Thiansathit, N. T. K. Oanh, K. G. Duleep, I. Paw-armart, and E. Winijkul (2009), Source characterization to support quantification of co-benefits: a piggyback study in Bangkok, Thailand, *Environmental Science and Technology*, *43*, 4213-4218.
Sun, H., L. Biedermann, and T. C. Bond (2007), Color of brown carbon: a model for ultraviolet and visible light absorption by organic carbon aerosol, *Geophysical Research Letters* (34), L17813, doi: 17810.11029/12007GL029797.
Updyke, K. M., T. B. Nguyen, and S. A. Nizkorodov (2012), Formation of brown carbon via reactions of ammonia with secondary organic aerosols from biogenic and anthropogenic precursors, *Atmospheric Environment*, *63*, 22-31.

Virkkula, A., N. C. Ahlquist, D. S. Covert, P. J. Sheridan, W. P. Arnott, and J. A. Ogren (2005), A three-wavelength optical extinction cell for measuring aerosol light extinction and its application to determining light absorption coefficient, *Journal of Aerosol Science*, *39*, 52-67.

Zhao, R., A. Lee, L. Huang, X. Li, F. Yang, and J. Abbatt (2015), Photochemical processing of aqueous atmospheric brown carbon, *Atmospheric Chemistry and Physics*, *15*(11), 6087-6100.

Zhong, M., and M. Jang (2014), Dynamic light absorption of biomass-burning organic carbon photochemically aged under natural sunlight, *Atmospheric Chemistry and Physics*, *14*(3), 1517-1525.

FIGURES

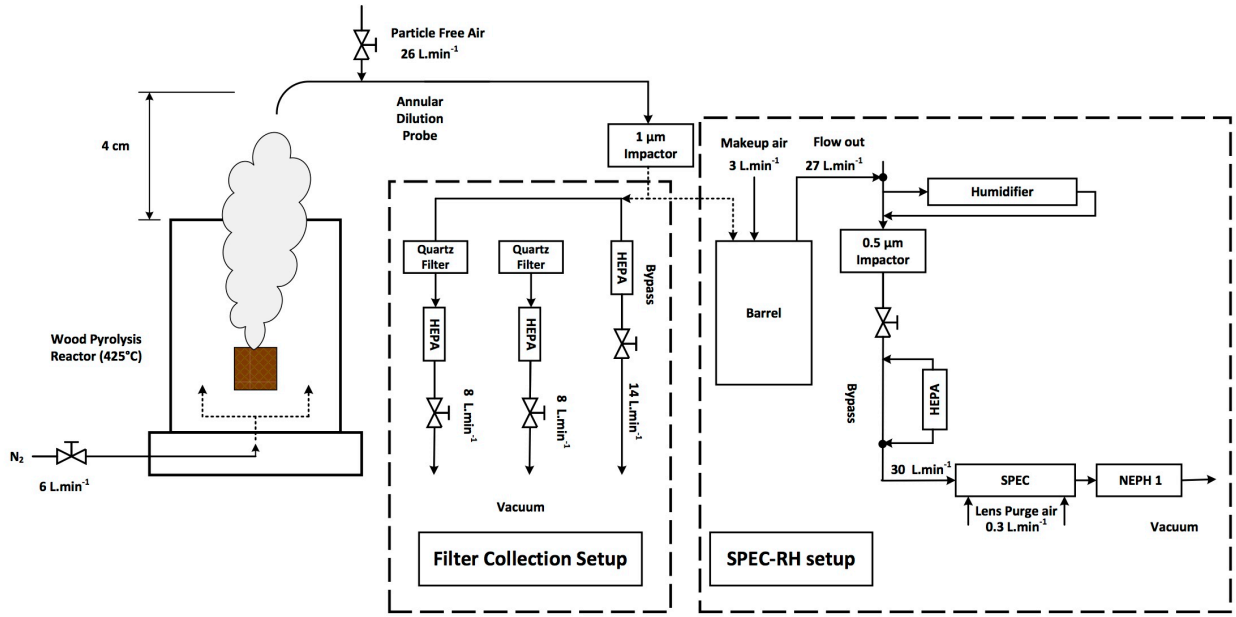

Figure 1. Schematic of the experimental setup of BrC generation, collection, and measurement using two methods: collection on filter media for measurements in liquid phase measurements, and optical properties measured for suspended particles

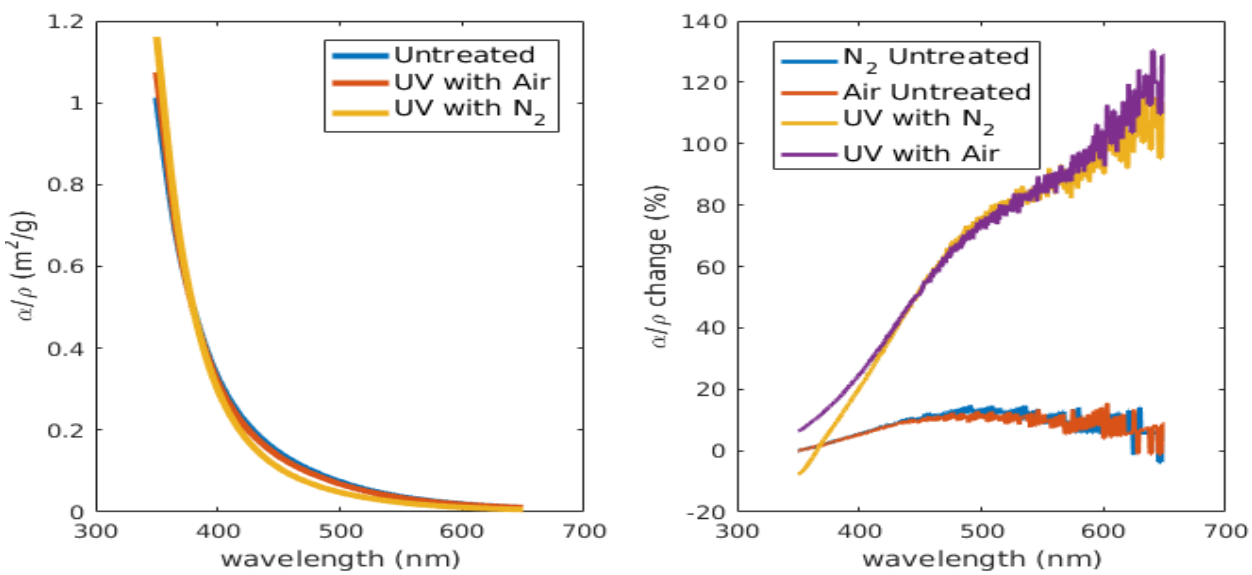

Figure 2. Absorption per mass (left) and percent change in absorption per mass (right) for extracts of BrC filter punches exposed to UV radiation in an air and N_2 purged vessel. "Untreated" punches experienced identical conditions in the vessel as the exposed punches but were shielded from UV radiation with a stainless steel mask.

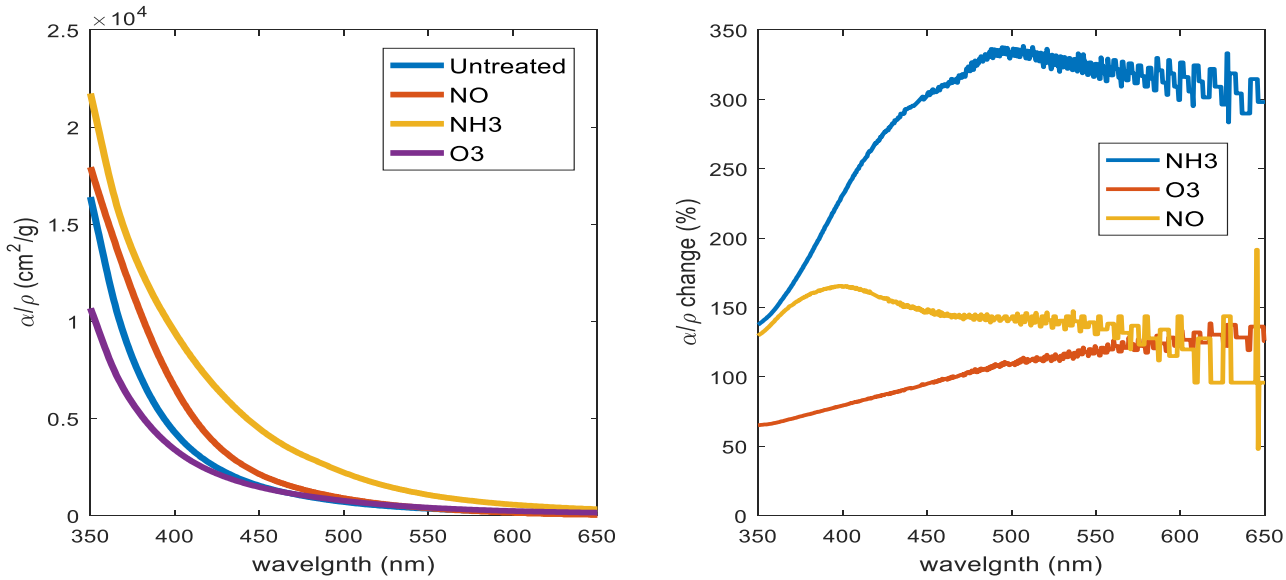

Figure 3. Absorption per mass (left) and percent change in absorption per mass (right) for extracts of BrC filters exposed to gaseous NH_3, O_3 and NO.

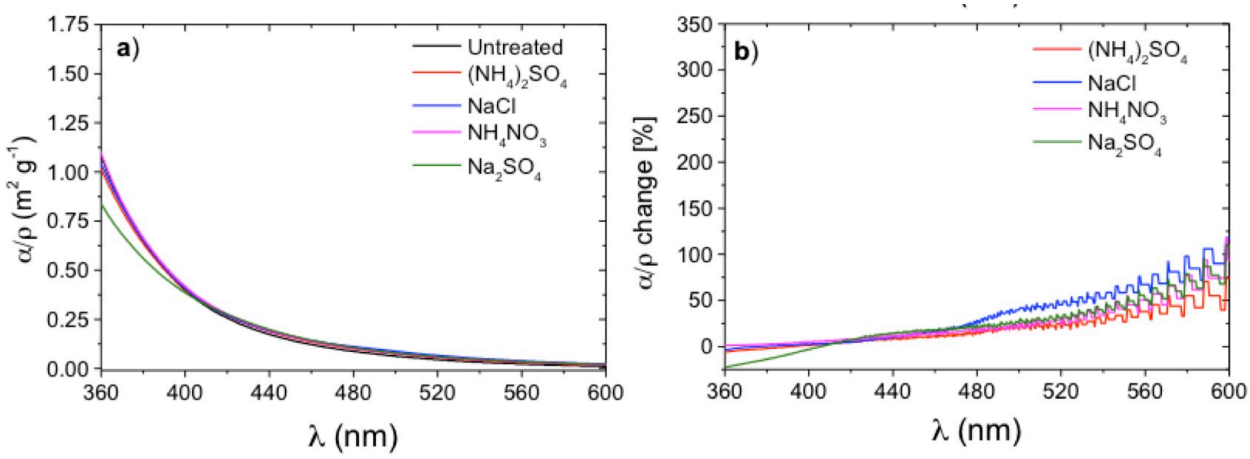

Figure 4. Absorption per mass (left) and percent change in absorption per mass (right) of BrC filter extracts treated with saturated aqueous solutions of $(NH_4)_2SO_4$, NH_4NO_3, NaCl and Na_2SO_4

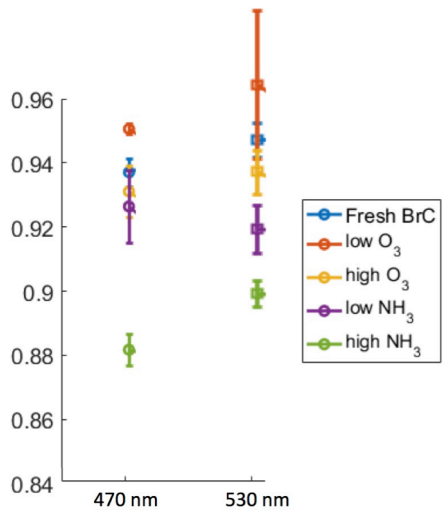

Figure 5. Change in single-scattering albedo after aging with ammonia and ozone, under dry conditions.

TABLES

Table 1. Reported values of primary BrC aerosol absorptive properties

Type	Author	Year	λ *(nm)*	k	$\mathring{a}_a$	Phase
HULIS Night	*Hoffer et al.*	2006	532	0.002	6.8	liquid
HULIS Day	*Hoffer et al.*	2006	532	0.002	6.4	liquid
BrC from Ponderosa Pine Smoke	*Chakrabarty et al.*	2010	532	0.003	16.7	aerosol
Methanol Extract of Pyrolysis OC	*Chen and Bond*	2010	530	0.004	7.8	liquid
Refractory OC from Biomass Burning	*Clarke et al.*	2007	530	0.005	15.7	aerosol
Biomass OC Methanol Extract	*Kirchstetter et al.*	2004	550	0.030	5.6	liquid
BrC from Biomass Burning	*Lack et al.*	2012	404	0.007	-	aerosol
Smoke HULIS	*Dinar et al.*	2008	532	0.048	2.8	aerosol
Pollution HULIS	*Dinar et al.*	2008	532	0.049	2.2	aerosol
Water Insoluble OC (Band Gap #2)	*Sun et al.*	2007	550	0.055	5.5	liquid
BrC spheres	*Alexander et al.*	2008	550	0.270	1.5	liquid

Table 2. Effect of aging agents on BrC absorptive properties at λ = 530 nm, for absorption in extracts. Each group of experiments began with a different biomass sample, so optical properties of untreated material varied slightly.

Treatment	α/ρ [m^2 g^{-1}]	α/ρ change [%]	ki	$\mathring{a}_a$
Untreated	0.039	-	0.0021	8.22
Air (Control)	0.043	6	0.0023	8.16
N_2 (Control)	0.041	5	0.0022	8.15
UV in Air	0.063	58	0.0034	7.09
UV in N_2	0.059	49	0.0032	7.16
Untreated	0.045	-	0.0024	8.02
NH_3	0.148	275	0.0078	6.88
O_3	0.052	15	0.0028	6.71
NO	0.058	48	0.0031	8.77
Untreated	0.038	-	0.0020	9.11
$(NH_4)_2SO_4$	0.047	24	0.0025	7.91
NaCl	0.058	50	0.0031	7.37
NH_4NO_3	0.051	35	0.0027	7.53
Na_2SO_4	0.052	37	0.0028	7.28

Appendix B.
Hygroscopic growth and cloud condensation nuclei activity of fresh and chemically-aged organic aerosol from biomass pyrolysis

R. U. Shah, H. Emamipour, M. J. Rood, and T. C. Bond

Submitted to Aerosol Science and Technology (in revision)

ABSTRACT. Biomass burning is a prominent contributor of atmospheric organic aerosols and cloud condensation nuclei (CCN). Estimates of aerosol-induced climate forcing are uncertain because atmospheric aerosol behavior is affected by both initial properties and transformations (aging). We present measurements of hygroscopic growth (<100% relative humidities; RH) as well as CCN activity and droplet sizes (>100% RH) of organic carbon (OC) aerosol emitted from biomass pyrolysis. We investigate changes in these properties after aging with NH_3, O_3 and RH. κ-Köhler parameterization of hygroscopic growth (κ_{GF}) and CCN activity (κ_{CCN}) reveal κ_{CCN} to be up to factor of three larger than κ_{GF}. This suggests that approximating surface tension of solution droplets to that of pure water, as assumed in κ-Köhler theory, does not apply to complex OC aerosol. Formation of multiple CCN activation modes confirms surfactant presence. 9-day equivalent NH_3-aging does not affect κ_{GF}, but increases κ_{CCN} of OC particles by 72%, suggesting formation of organic acidic groups upon aging. While O_3 has no measurable impact on the κ of OC particles, it delays cloud droplet growth, possibly because gas-phase organic compounds in the aerosol condense as films on particles upon oxidation. We find that aerosol water during aging at controlled RH does not affect resulting hygroscopicity of particles. Our results are consistent with previously reported impacts of NH_3 and O_3 aging on the hygroscopicity of organic particles, but confirms them for more complex OC particles. These results are important because they provide constraints on important chemical aging mechanisms for organic particles.

1. Introduction

Open burning of vegetation and biofuels burned for combustion, collectively termed "biomass burning" or BB, emit about 90% of primary organic carbon (OC) aerosols globally (Bond et al. 2004). These aerosols, along with other inorganic and black carbon (BC) emissions, affect the climate (Ramanathan et al. 2007). BB emits particles that have varying degrees of affinity for water, termed "hygroscopicity". Depending on their hygroscopicity and size, particles in the atmosphere can take up water and undergo hygroscopic growth at sub-saturated relative humidity (RH) and can also serve as cloud condensation nuclei (CCN) and activate into cloud droplets when RH is super-saturated. Cloud properties are affected by presence of CCN in the atmosphere (Andreae 2008, Hennigan et al. 2012). Twomey (1977) showed that an increase in CCN concentration leads to a reduced cloud droplet size when clouds are limited by availability of condensable water vapor, thus enhancing cloud albedo. As clouds become brighter with smaller droplets, more solar radiation is scattered upward, leading to cooling: this is termed the "first indirect effect" of aerosols. This negative radiative forcing of the climate counteracts the positive, direct forcing caused by absorption of radiation by greenhouse gases (e.g., CO_2) and some particles in the atmosphere (Andreae and Ramanathan 2013, Bond et al. 2013). Moreover, due to reduced cloud droplet size, precipitation is suppressed: this is the "second indirect effect" of aerosols (Andreae et al. 2004).

Although efforts to estimate climate forcing have spanned decades, the uncertainty in estimates of aerosol-cloud interactions is still 1.2 Wm^{-2} of the total of 2.2 Wm^{-2} uncertainty in estimating anthropogenic forcing of the climate (Myhre et al. 2013). Global model estimates of CCN concentrations from BB are highly uncertain (Spracklen et al. 2011), primarily because the impact of BB aerosols on clouds depends on the number of CCN in the aerosol, which in turn depends on the water affinity and size distribution of the aerosol particles (Andreae and Rosenfeld 2008). While freshly emitted organic aerosol particles are hydrophobic and thus serve as CCN only at very high values of supersaturation (*SS*), these particles can become hygroscopic within 24 h of emission (Stier et al. 2006). Aerosol particles in a BB plume are rapidly transformed by several processes, collectively termed "aging". Aging includes physical processes (i.e., coagulation and condensation) as well as chemical processes (i.e., surface-based chemical interaction with reactive species). It is important to identify the atmospheric chemical aging pathways that render these initially hydrophobic aerosol particles more able to serve as CCN, known as "CCN-active." Identifying aging mechanisms also aids in estimating the atmospheric lifetime of the aerosols (Slade and Knopf 2013).

A common measure of CCN activity is the diameter, D_{50}^{SS}, at which 50% of the total aerosol particles activate into cloud droplets at a given *SS*. A decrease in D_{50}^{SS} for a single size distribution indicates an increase in CCN activity due to higher soluble content of the particles. Conventional Köhler theory predicts the CCN activity of a particle based on the equilibrium between the surface tension and solute presence, quantified by the Kelvin and Raoult terms, respectively (Köhler 1936). A common representation of hygroscopic growth at sub-saturated RH is the size growth factor, GF_{RH}, or the ratio of the diameter of a particle (D_{RH}) at a reference RH to its dry diameter (D_{dry}). Both hygroscopic growth and CCN activity depend on the amount and nature of soluble matter in the particles, and these properties are collectively termed "hygroscopicity" in this paper. Hygroscopicity has been parameterized using the κ-Köhler theory (eq. 1, Petters and Kreidenweis 2007). For a particle of dry diameter D_{dry}, the hygroscopicity parameter, κ, relates its wet diameter, D_{wet}, to its water activity, a_w:

$$\frac{1}{a_w} = 1 + \kappa \left[\frac{D_{dry}^3}{D_{wet}^3 - D_{dry}^3} \right] \qquad [1]$$

Reported values of κ range from strongly hydrophobic (κ = 0 for completely insoluble particles) to strongly hygroscopic (κ = 0.6 for $(NH_4)_2SO_4$). Moreover, κ can be calculated from measurements of either GF_{RH} or D_{50}^{SS} (denoted as κ_{GF} and κ_{CCN}, respectively). Compiling previously published measurements of hygroscopic growth and CCN activity, Petters and Kreidenweis (2007) calculated κ_{GF} and κ_{CCN} for 25 organic and inorganic compounds. The agreement between κ_{GF} and κ_{CCN} was within 30% for those organic substances. These discrepancies were attributed to experimental uncertainties. Discrepancies larger than this value indicate the possible presence of surfactants or sparingly soluble matter (Dusek et al. 2003, Petters and Kreidenweis 2007). Surfactants and sparingly soluble matter alter the Kelvin and Raoult terms, respectively, that are expressed in Köhler theory, thereby affecting the overall CCN activity of the particle (Li et al. 1998).

Chemical aging of organic aerosol particles by reactive gases can affect their solubility and surface active properties, which affects their CCN activity (Petters et al. 2006). NH_3 and O_3 are observed throughout the lower atmosphere in trace amounts, with exact values varying spatially and temporally. Ambient levels of NH_3 have been observed to be as low as 0.5 ppb_v in rural locations (Lewin et al. 1986). In regions of high BB activity, ambient NH_3 as high as 8 ppb_v has been observed (Trebs et al. 2004). Accounting for uptake of NH_4^+ ions by ambient aerosol particles is important in predicting their hygroscopicity, because this mechanism neutralizes the acidic groups and affects the water-soluble content of particles (Mircea et al. 2005, Trebs et al. 2005). Surface O_3 levels of 10 to 30 ppb_v have been measured in the United States (Fiore 2003) and concentrations as high as 40-60 ppb_v have been measured in regions with high BB activity (Bela et al. 2015). Water uptake from atmospheric humidity may also participate in the chemical reactions of organic aerosol particles (Abbatt et al. 2012).

We briefly review studies that have reported changes in hygroscopicity of laboratory-generated surrogates of atmospheric organic aerosol particles due to chemical aging with NH_3 and O_3. Wu et al. (2011) showed that hygroscopicity of surrogates increased after neutralization of acidic groups by NH_4^+. Dinar et al. (2008) observed that exposure to 1 ppm_v NH_3 did not affect the κ_{GF}, but decreased the $D_{50}^{0.64\%}$ of sparingly soluble organic aerosol particles by 55%. Slade et al. (2015) showed that oxidation by O_3 had no impact on the CCN activity of single, binary and ternary mixtures of BB surrogate compounds in the laboratory. Ozonolysis has been shown to induce formation of organic films on aerosol particles due to condensation of low volatile organic vapors in the aerosol (Anttila et al. 2007). Formation of such organic films could affect the hygroscopicity of the particles (Lambe et al. 2015).

In addition to affecting hygroscopicity, organic films on particles can also impede mass transfer of water vapor to the particles and thus inhibit the rate of droplet growth at super-saturated RH (Feingold and Chuang 2002). Droplets exhibiting slower growth are prone to broaden the droplet size distribution in the atmosphere (Feingold and Chuang 2002). An implication of this effect is increased atmospheric lifetimes of these droplets (Ruehl et al. 2007).

Studies have also investigated properties of particles emitted from BB, instead of surrogates (e.g., Petters et al. 2009, Dusek et al. 2011). These studies analyzed emissions from burning different species of biomass and found κ ranging from 0.06 to 0.2 for emissions from burning of wood or branches with leaves. They found that measured κ_{GF} and κ_{CCN} for a given BB aerosol particle population differed within the aforementioned 30% uncertainty that could be ascribed to measurement error. Moreover, Petters et al. (2009) also found that the size-resolved CCN activation curves of different BB emissions differ in shape owing to chemical and morphological heterogeneity of the particles. These studies investigated BB emissions without isolating the stages of combustion. However, in a BB event, vaporized volatile compounds can either condense to form OC particles (Evans and Milne 1987) or burn in a diffusion flame to form BC particles. These sequentially-emitted particles have differing properties, and isolated OC has not been investigated separately. Characterization of isolated OC emissions from BB thus provides information on the climatically-relevant properties of a major fraction of the global OC burden.

Studies have not yet investigated the hygroscopicity of complex biomass-pyrolysis OC aerosol particles and how it evolves upon chemical aging. In this study, we address this gap by experimentally investigating the hygroscopicity of fresh and chemically-aged OC aerosol particles generated from biomass pyrolysis. We measured and compared κ_{GF} and κ_{CCN} to infer the possible presence of surface active and sparingly soluble matter. We also measured the size distribution of droplets after activation in the cloud chamber in order to infer changes in the growth rates of droplets at supersaturated RH.

Studies reviewed earlier in this section have measured hygroscopicity of either chemically-aged BB surrogate aerosols or freshly emitted BB aerosols. The unique aspect of this study is combining these two approaches by studying aerosols generated by biomass pyrolysis and then simulating atmospheric chemical aging of these aerosols to characterize the hygroscopic growth *and* CCN activity of particles before and after chemical aging. Results of this study are important in evaluating not just the hygroscopicity of aerosols emitted during biomass pyrolysis, but also the possible chemical reactions that transform them in the atmosphere. Properties of both freshly generated and aged aerosols govern their interactions with clouds and their wet removal from the atmosphere.

2. Experimental methods and data analysis

2.1 Overall approach

We measured the hygroscopic growth and CCN activity of OC aerosol generated in biomass pyrolysis. For the remainder of this paper, the term "OC" will refer to this pyrolytically generated aerosol. A schematic describing the research approach used in this study is shown in Fig. 1. All reported aerosol flow rates are standardized to 1 atm and 0 °C.

2.2 Generation and sampling of aerosol

$(NH_4)_2SO_4$ (AS; ACS Certified, Fisher Scientific A702) and 100, 200 nm polystyrene latex (PSL; Thermo Scientific Inc. 3200A) aerosols were generated using a constant output atomizer (TSI 3076) using deionized water to produce reference aerosols for calibration. Aerosol was dried (< 1% RH) using a custom-built silica gel diffusion dryer. AS is a common inorganic salt, the hygroscopic properties of which have been well-characterized. Hence AS was used for calibrating instruments that measure the hygroscopic properties of aerosols. PSL spheres were used for evaluating the particle sizing instrumentation.

OC aerosol was generated by pyrolysis of oak wood biomass. Pyrolysis was controlled inside a reactor (Chen and Bond 2010) and is briefly described here for clarity. Oxygen-deficient conditions were created by passing gaseous N_2 (99.95% purity by mass) at 12.4 ± 0.1 slpm into the bottom of the reactor, with a residence time of 3.7 s at standard conditions. The temperature at the bottom of the reactor was maintained at 300 °C using a 650 W proportional-integral-derivative (PID) controlled heater (Watlow VC403A06A). The biomass used in a single batch test was 0.32 ± 0.01 g, measured using an analytical balance (Mettler-Toledo AB204-S). OC aerosol was drawn from top of the reactor at 2.03 ± 0.02 slpm and was diluted immediately in an annular sampling probe by mixing with clean air at 25.88 ± 0.21 slpm. Sampling and dilution of OC was done for 30 s and was directed

to a 208 L stainless steel mixing chamber. Clean air for dilution was generated by passing compressed air through a high efficiency particulate air filter, a silica gel column and an NH_3 adsorbent (AmmoSorb™, Imtek Environmental) column. A fan inside the chamber induced mixing of aerosol. Prior to OC injection, the chamber was purged with clean air to remove any residual particles and gases from the previous test. Particle concentration inside the chamber was measured less than 5 cm^{-3} with a condensation particle counter (CPC, TSI 3010) before each test.

2.3 Aging of aerosol

The atmospheric lifetime of primary organic aerosols typically considered in models is 4.3 to 11.1 days (Kanakidou et al. 2005). It is, however, challenging to chemically age organic aerosols over such time periods in laboratory studies. One experimental approach is assuming that the reaction between a gas-phase chemical and aerosol particles follows pseudo-first order kinetics (Rudich et al. 2007), reducing exposure time and increasing reactant concentration so that the exposure-time product is same as that occurring in the atmosphere. This equivalence has been used in experimental studies (Engelhart et al. 2008, Lambe et al. 2015) and is also the principle behind some of the tests reported here. Experimental test conditions are summarized in Table 1, which also shows the unique aging IDs assigned to each set of conditions.

With the exception of AS, the initial aerosol for all aging tests was OC. Moreover, as shown in Table 1, hygroscopic growth measurements were done only when RH during aging inside the mixing chamber was less than 1%. For simplicity, we refer to all RH values less than 1% as 0% in this paper.

Two concentrations of NH_3 were used in this study: 10 and 875 ppm_v. The duration of aging of OC between injection into chamber and drawing out for measurements was 10 min. A 10 min aging with 10 ppm_v NH_3 is equivalent to 9 days of atmospheric aging at an 8 ppb_v ambient NH_3 level. A higher NH_3 concentration of 875 ppm_v was also used as an upper bound aging condition to observe whether changes in hygroscopicity occurred after aging OC for 10 min at this very high concentration. In tests with 10 ppm_v NH_3 aging, a 700 mL pulse of 3000 ppm_v NH_3 was injected into the mixing chamber using a syringe and hypodermic needle immediately after it was filled with OC particles. For achieving 875 ppm_v NH_3 in the mixing chamber, reagent grade 3000 ppm_v NH_3 in N_2 from a compressed gas cylinder was diluted with clean air and the mixing chamber was flushed with this mixture for a minimum of 30 min to achieve steady-state concentration.

Two concentrations of O3, 0.1 and 0.3 ppmv, were used in this study. After maintaining controlled O_3 concentration in the chamber for 5 min, aerosol was sampled by instruments as described in Sec. 2.4 and 2.5. While sampling, a make-up flow equal to sampling flow was provided to the chamber. O_3 in the make-up flow was controlled to ensure constant O_3 inside the chamber. Sampling lasted for 120 min, causing a total equivalent atmospheric aging of 6 hr and 18 hr (assuming average ambient O_3 of 35 ppb_v). As will be discussed in Section 2.5, all CCN activity tests were done by measuring particles of successively greater diameters. Hence, particles drawn out of the chamber first experienced a shorter duration of O_3 aging. The direction of size-scanning was also reversed and the test was duplicated to ensure that this difference in aging time did not

affect the results. O_3 was generated by passing 0.45 slpm clean air through a variable output O_3 generator (Jelight 610) and diluted with clean air to achieve steady-state O_3 concentration in the mixing chamber prior to OC injection.

For every concentration of reactant (NH_3 and O_3), RH was controlled at 0, 70 and 85% in the mixing chamber during aging to investigate whether aerosol water would participate in the chemical aging process. RH inside the mixing chamber was achieved by a custom annular humidifier that controls water vapor diffusion through a GoreTex™ membrane (Winter 2002). RH was measured using a capacitance-based RH sensor (Vaisala, HMP 330). Periodic calibration of the RH sensors was done in the 43% to 97% RH range using saturated solution cells of K_2CO_3 and K_2SO_4. Due to PID-based control of RH, the instantaneous RH of clean air entering the mixing chamber fluctuated within $\pm$5% of the control value. However, these fluctuations were damped inside the mixing chamber and the measured steady-state RH inside the chamber was within $\pm$2% of the control value.

2.4 Hygroscopic growth measurement

A controlled RH humidified-tandem differential mobility analyzer (H-TDMA) setup (Rader and McMurry 1986), shown in Fig. 2, was used for measuring the hygroscopic growth of aerosols at subsaturated humidity conditions.

Aerosol from the chamber was passed through a custom-built silica gel diffusion dryer. Dried aerosol (< 10% RH) was first passed through a ^{210}Po charger (Amstat Corp. 2U500) to achieve equilibrium charge distribution and a constant voltage was used to select an electric mobility diameter of 100 nm with a custom-built differential mobility analyzer (DMA), previously used by Brem et al. (2012). Size-selected dry aerosol was humidified to controlled RH with a smaller replica of the humidifier described in Winter (2002). The humidified particle size distribution was then measured using a scanning mobility particle sizing (SMPS) system. The SMPS consists of an electrostatic classifier (TSI 3071), in which the voltage is scanned, and the number of particles selected at each voltage is measured by a CPC (TSI 3022A). The DMA and the EC were both operated with a 10:1 sheath-to-sample flow ratio with total flow being 10.13 ± 0.08 slpm. As shown in Fig. 2, four capacitance-based relative humidity sensors (Sensirion SHT-75) were used to measure RH through the setup.

2.5 CCN activity measurement

The experimental setup used for measuring CCN activity in this study is shown in Fig. 3. Particles were selected based on their electric mobility diameter by a DMA. Mobility diameters between 50 and 180 nm were typically scanned in increasing order with increments of 15 nm and sampled by three instruments: a CPC (TSI 3010), an SMPS and a continuous flow streamwise thermal gradient CCN counter (Roberts and Nenes 2005, Lance et al. 2006; DMT CCN-100). Each diameter was fixed for 6 min (2 min for equilibration, 4 min of data averaging). Thus, nominal time for scanning the entire particle range was 1 hr.

This CCN counter is described here briefly. A sheath-to-sample flow ratio of 10:1 was used with total aerosol inlet flow of 0.56 ± 0.004 slpm. Pressure inside the cloud

chamber was 985.7 ± 8.4 mbar. Sample aerosol was exposed to a constant supersaturation by applying a temperature gradient across a cloud chamber with wetted walls. An atmospherically relevant *SS* of 0.3% was used in all CCN tests. Typical atmospheric values of *SS* are as low as 0.01% to as high as 1% at cloud base (Andreae and Rosenfeld 2008). In this range, 0.3% is the midpoint in logarithmic space.

2.6 Data analysis

2.6.1 SMPS data inversion for hygroscopic growth tests

As discussed in Section 1, GF_{RH} is the ratio of the particle diameter at a given elevated, controlled RH (D_{RH}) to the reference diameter at RH < 10% (D_{dry}). The raw SMPS data were inverted using TDMA*inv*, a data inversion toolkit by Gysel et al. (2009). In this toolkit, raw SMPS data from scans done at RH < 10% (GF_{RH} = 1) were used to calculate corrections for sizing offsets and the width of the DMA's transfer function. A piecewise linear function was then fit to the corrected SMPS data and the true mean GF_{RH} values were retrieved.

2.6.2 Calculation of κ_{GF}

GF_{RH} values were measured between 10 and 92% RH and κ_{GF} was calculated with the assumption that κ-Köhler theory is valid (Petters and Kreidenweis 2007). According to this simplified version of Köhler theory, the water vapor saturation ratio, *S*, over an aqueous solution droplet of diameter, *D*, is given as

$$S = a_w \exp\left(\frac{A}{D}\right) \qquad [2]$$

$$A = \frac{4\sigma_w M_w}{\rho_w RT} \qquad [3]$$

where, a_w = water activity; σ_w = surface tension of pure water (0.072 Nm^{-1}); M_w = molecular weight of water; ρ_w = density of water; R = universal gas constant; T = absolute temperature. The water activity, a_w, is given in Equation (4), GF_{RH} is shown in Equation (5), and κ_{GF} is calculated by iterative solution of Equations (4) and (5) from the measured GF_{RH} values.

$$a_w = \frac{D_{RH}^3 - D_{dry}^3}{D_{RH}^3 - D_{dry}^3(1-\kappa)} \qquad [4]$$

$$GF_{RH} = \left[1 + \frac{a_w \kappa_{GF}}{1 - a_w}\right] \qquad [5]$$

2.6.3 Calculation of κ_{CCN}

Petters and Kreidenweis (2007) derived an approximate expression for κ_{CCN}, shown in Equation (6), by fitting paired D_{50}^{SS}-SS measurements to the maxima of Equation (2).

$$\kappa_{CCN} = \frac{4A^3}{27(D_{50}^{SS})^3 \ln^2 SS} \qquad [6]$$

where the constants in Equation (3) are combined to give A = 2.1 nm (at 25 °C). Equation (6) was used in this study to calculate κ_{CCN} from a measured D_{50}^{SS}. This method of representing CCN activity assumes that water activity of particles of diameter D_{50}^{SS} is characteristic of particles of all sizes.

2.6.4 Effects of surfactants on κ

The κ-Köhler theory approximates the effective surface tension of a solution droplet (σ') as σ_w. While this assumption may hold for calculating κ_{GF}, it may result in an overestimation of κ_{CCN} for BB aerosol, if σ' is affecting its CCN activity (Dusek et al. 2011, Li et al. 1998). This effect was explored in this study by setting κ_{CCN} in Equation 6 equal to the measured value of κ_{GF}. Iterative solution of Equations 3 and 6 using the measured value of $D_{50}^{0.3\%}$ then returned a fitted value for σ'.

2.6.5 Droplet size distribution

The CCN counter, in addition to counting the number of particles that activate into droplets at a given S value, also measures the diameters of activated droplets, D_{drop}, downstream of the cloud chamber. The output from the CCN counter is in the form of frequency distribution of droplet numbers classified into 0.5 μm-wide "bins" between 0 and 10 μm. All CCN in this study were exposed to the same SS for the same time inside the cloud chamber. The factors that can affect the D_{drop} downstream of the cloud chamber include sample pressure, SS in the cloud chamber, sample flow rate, critical SS of particles, CCN concentration and the water uptake rate of the activated CCN (Lathem and Nenes 2011). As described in Section 2.5, the first three factors in the previous sentence were maintained constant during all CCN activity tests. We measured the size distribution of droplets that activated from CCN of 130.5 $\pm$ 3.2 nm mobility diameter, a value that is well above the largest $D_{50}^{0.3\%}$ measured in this study (i.e., 108.5 nm). Thus, all particles of this size were expected to activate and any differences in size distribution between two tests reflects the effect of water uptake rate, assuming the particles were all uniform in composition. Depletion of condensable water vapor does not affect D_{drop} by more than 10% if the CCN concentration is less than 5000 cm^{-3} (Lathem and Nenes 2011). The absolute number concentration of the 130 nm size-selected particles entering the cloud chamber varied between 1000 and 2000 cm^{-3}. To aid comparison of frequency distribution of droplet diameters measured in different tests, the frequencies in each test were normalized to the total number of droplets.

3. Results and Discussion

In this section, instrumentation performance is discussed in Section 3.1. We begin with an examination of apparent hygroscopic behavior as typically presented, comparing hygroscopic growth (represented by κ_{GF}) and CCN activity (represented by κ_{CCN}) in Section 3.2 for fresh and aged OC. Also discussed is the possible effect of surfactant presence on the inferred values of κ_{CCN} by accounting for an effective surface tension of solution droplets. The use of κ_{CCN} neglects any dependence of CCN activity on particle size, so Section 3.3 discusses observed changes in differential CCN activation spectra with aging. Lastly, size distributions of activated droplets measured downstream of the cloud chamber are presented in Section 3.3, and inferences for kinetic inhibition are discussed.

3.1 Instrumentation performance

Accuracy of the SMPS was verified by calibration with PSL spheres within 2%. Measured hygroscopic growth, CCN activity and activated droplet size distribution of AS are shown in Fig. 4.

Calculated values of κ_{GF} *and* κ_{CCN} (as outlined in Section 2.6.2) are κ_{GF} = 0.59 and κ_{CCN} = 0.61 for AS. These values agree within 3% and are also consistent with previously reported values for AS (Petters and Kreidenweis 2007). Moreover, diameters of droplets activated from initially dry AS particles at 0.3% *SS* are in the 3 to 4 μm diameter range, consistent with previously reported measurements (Engelhart et al. 2008, Asa-Awuku et al. 2010). Reproducibility of chemical aging results was tested by duplicating all CCN tests at least once. The measured $D_{50}^{0.3\%}$ in each test was always within 8% in duplicate tests.

3.2 Hygroscopic growth and CCN activation of fresh and aged OC particles

3.2.1 Hygroscopic growth

Hygroscopic growth factors of fresh and chemically-aged OC particles are shown in Fig. 5. The dependence of GF_{RH} on RH, as predicted by κ-Köhler theory, is consistent with values measured in this study (Fig. 5). The measured κ_{GF} = 0.06 of fresh OC is within the range of κ = 0.02 to 0.15 measured by Dusek et al. (2011) and 0.05 to 0.20 measured by Petters et al. (2009) for particles emitted from burning of wood fuels. Measured GF_{RH} values for chemically aged, 100 nm OC particles appear same as those for fresh, 100 nm OC particles. This suggests that aging with NH_3 or O_3 has no effect on the hygroscopic behavior of these particles at subsaturated RH.

3.2.2 Cumulative CCN activation spectra

Size-resolved, cumulative CCN activation spectra for fresh aerosol are shown in Fig. 6. The CCN activity of OC is not affected by chemical participation of aerosol water during aging, as shown by comparing tests Fresh-RH0, Fresh-RH70 and Fresh-RH85.

The departure from a sigmoidal shape implies that inference of κ_{CCN} from the single-point measurement of $D_{50}^{0.3\%}$ does not capture the full complexity of aerosol behavior. To discuss this departure, we discuss CCN activity of chemically-aged OC in two ways. First,

in Fig. 7, we show singular hygroscopicity parameters (κ) for each test, derived from $D_{50}^{0.3\%}$, to quantify the overall change in hygroscopic behavior upon aging. In Section 3.2.3, we present differential CCN activation spectra to show heterogeneity across the range of particle diameters.

Aging with NH_3 increases CCN activity without affecting hygroscopic growth (tests NH3-10-RH0 and NH3-875-RH0 in Fig. 7). κ_{CCN} increases by 84% and 109%, respectively. Compared to fresh, dry OC, values of $D_{50}^{0.3\%}$ after aging with NH_3 are smaller by 18% and 22%, respectively. For all values of RH during aging, there is a consistent reduction in $D_{50}^{0.3\%}$and an increase in κ_{CCN}. Therefore, water taken up in the mixing chamber does not participate in modifying the aerosol, even when the aging reactant is soluble.

The fact that κ_{CCN} increases after NH_3 aging, but κ_{GF} does not, suggests that the combination of NH_3 and biomass OC yields organic acidic groups of sparing solubility. With such low solubility, the material does not dissolve into the aerosol-bound water even at 92% RH, the highest RH measured in the H-TDMA measurements. However, as RH approaches 100% and the droplets become further dilute, organic acidic groups do undergo dissolution (Dusek et al. 2003), and there is an abrupt increase in the GF_{RH} (and κ_{GF}) (Dinar et al. 2008). This dissolution increases κ_{CCN}.

The $D_{50}^{0.3\%}$ (and subsequently, κ_{CCN}) of dry OC is also unaffected by O_3 (tests O3-0.1-RH0 and O3-0.3-RH0 in Fig. 7). For tests where RH was held at 70 and 85% RH during aging, aerosol water also does not participate in chemical aging (Fig. 7). Slade et al. (2015) observed that 0 to 120 ppb_v O_3 exposure did not affect the hygroscopicity of single, binary and ternary mixtures of BB surrogate aerosols; these results confirm that finding for realistic laboratory generated BB aerosol.

While the measured κ_{GF} and κ_{CCN} of the fresh and aged OC aerosol particles are within previously reported ranges of κ for biomass burning particles (Petters et al. 2009, Dusek et al. 2011), discrepancies as large as factors of three occur between κ_{CCN} and κ_{GF} for each test. By setting κ_{CCN} equal to κ_{GF} in Eq. 7, the effective surface tension σ' was calculated (see Section 2.6.3). The average and standard deviation of σ' calculated for all hygroscopic growth tests was 0.053 ± 0.006 Nm^{-1}, 25% lower than the surface tension of pure water. Therefore, approximating the surface tension of a solution droplet with that of pure water underestimates the κ_{CCN} of complex organic aerosol emitted from biomass pyrolysis, especially when particles are aged with NH_3.

3.2.3 Differential CCN spectra

Differential CCN activation spectra can show chemical heterogeneity across a range of particle diameters. These spectra are shown in Fig. 8 for each aging condition described earlier (Table 1).

The CCN activation spectra for fresh OC tend to have a single major peak, seen in the spectra as $D_{50}^{0.3\%}$. The aged OC activation curves, however, exhibit an increased fraction of activated sub- and super-$D_{50}^{0.3\%}$mobility diameter particles (or, "activation modes"). These activation modes were also observed in duplicate tests. An activation mode in the 70 to 100 nm diameter range (e.g., NH3-875-RH85 in Fig. 8) could be observed if surfactant solutions are present in these droplets. Even if particles have uniform chemical composition

at different diameters (in other words, the fraction of surfactant is equal in 70 and 100 nm particles), droplets formed by condensation of water on 70 nm particle would contain more concentrated surfactant than droplets formed on 100 nm particles. This is a possible explanation for the enhanced activation of sub-$D_{50}^{0.3\%}$particles after aging with NH_3 and O_3. This reasoning is also consistent with the findings of Dusek et al. (2011). Some of the activation curves in Fig. 8 also exhibit another activation mode for particles larger than $D_{50}^{0.3\%}$. For instance, a second activation mode is observed for the 110 to 170 nm mobility diameter particles aged with 0.1 ppm_v O_3 in dry conditions for test O3-0.1-RH0. Similar activation modes have been observed previously for BB particles in this diameter range by Petters et al. (2009). They suggested that chemical aging induces heterogeneity in the aerosol, so that particles in the 110 to 170 nm range of mobility diameters have different chemical mechanisms are more CCN active after aging. To confirm this, κ_{CCN} must be measured only for particles of mobility diameter in this range (by determining the supersaturation at which 50% of the particles in this size range activate) in the future and then compared to the overall κ_{CCN} measured for the entire 50 to 170 nm range.

3.3 Droplet growth

In this section, we present the results of droplet size distributions measured as the activated droplets exit the cloud chamber. Size distributions of droplets resulting from activation of differently-aged particles (Table 1) are compared to infer the effect of aging mechanisms on droplet growth kinetics. This additional measurement capability of the CCN counter has been utilized to this end in previous studies (Engelhart et al. 2008).

Figs. 9 a and b show the normalized distribution of activated droplet diameters exiting the cloud chamber after activation of 130 nm particles at 0.3% *SS*. The figures show evidence of reduced droplet growth of the O_3-aged particles compared to fresh OC particles (tests O3-0.1-RH0 and O3-0.3-RH0). A possible mechanism causing this retardation is that the formation of condensed films on the OC particles after O_3 aging (Anttila et al. 2007) impedes droplet growth after activation of CCN inside the cloud chamber (Chuang 2003). The droplet growth appears unaffected for particles aged with 0.1 ppm_v O_3 in the presence of humidity during aging (test O3-0.1-RH85; results at 70% RH not shown). However, with a higher concentration of O_3 (0.3 ppm_v, O3-0.3-RH85), reduced droplet growth does occur after aging under humid conditions. Aging with NH_3 at different RH values showed no droplet growth retardation, which further implies that organic particle precursors within the aerosol are condensing as films on pre-existing OC particles after oxidation.

4. Summary, conclusions and atmospheric implications

The hygroscopic growth and CCN activity of complex biomass pyrolysis OC aerosol was experimentally measured with and without controlled conditions of relative humidity (RH) and chemical aging by atmospherically relevant tracer species, NH_3 and O_3. The role of these aging conditions in the enhancement of hygroscopicity of organic aerosols was investigated. From measurements of hygroscopic growth at subsaturated RH and CCN activity at supersaturated RH, we measured the hygroscopicity parameters, κ_{GF} and κ_{CCN}, respectively. Discrepancies between the κ_{GF} and κ_{CCN} of each aerosol population suggest the presence of surfactants in these aerosol particles. Therefore, approximating the surface tension of droplets to that of pure water, which is the basis of κ-Köhler theory,

underestimates the CCN activity of biomass pyrolysis particles, especially when particles are aged with NH_3. Surfactant presence in OC particles is also indicated by the enhanced CCN activation of particles in the 70 to 100 nm mobility diameter range.

Increase in κ_{CCN} of NH_3-aged OC particles, while κ_{GF} remains unaffected, suggests sufficient insoluble or sparingly soluble organic acidic groups to influence the overall hygroscopicity of the particles. This finding suggests that increased CCN activity of organic particles can result from reaction with gas-phase NH_3. Effects in activating clouds depend on this increase, but also on several other factors such as mixing of aerosol particles with other hygroscopic or hydrophobic particles, updraft velocity of the parcel carrying those particles, availability of condensable water vapor and number of CCN competing for the water (Roberts et al. 2003, Petters et al. 2006). Reutter et al. (2009) modeled deep clouds formed above BB fires (pyro-convective clouds) using a cloud parcel model, and showed that the cloud droplet number concentration, N_{CD}, is sensitive to changes in κ of aerosol particles, when κ is lower than 0.2. For instance, an 81% increase in κ (as measured in this study) of particles having initial κ = 0.057 can cause a 20% increase in N_{CD}. However, given that the measured increase in hygroscopicity of organic particles is still significantly smaller than that of commonly observed inorganic particles, inorganic substances that affect these particles either by coagulation or condensation may also have strong effects on the hygroscopic growth and CCN of ambient atmospheric particles. For instance, Fierce et al. (2013) showed that at SS > 0.2%, CCN activity of hydrophobic particles is most sensitive to rapid aging by condensation of other species.

We confirm the findings of Slade et al. (2015) that O_3-aging has no effect on the measured hygroscopicity of OC aerosol. However, our findings suggest the formation of organic films on particles after O_3 oxidation and condensation of organic gases in the aerosol, because growth of activated droplets in the cloud chamber is inhibited. Although cloud chamber studies do not simulate limitations on the amount of condensable water available for droplets to grow, these limitations exist in the atmosphere (Roberts et al. 2003). As shown by Feingold and Chuang (2002) and Ruehl et al. (2007), in such conditions of competition, CCN coated with such growth-retarding organic films could grow slower compared to other uncoated CCN, leading to broadened size distributions and possibly prolonged lifetimes of droplets in the atmosphere.

References

Abbatt, J. P. D., Lee, A. K. Y., and Thornton, J. A., 2012. Quantifying trace gas uptake to tropospheric aerosol: recent advances and remaining challenges. *Chem. Soc. Rev.*, 41 (19), 6555–6581.

Andreae, M. O., 2008. Correlation between cloud condensation nuclei concentration and aerosol optical thickness in remote and polluted regions. *Atmos. Chem. Phys. Discuss.*, 8 (3), 11293–11320.

Andreae, M. O. and Ramanathan, V., 2013. Climate's dark forcings. *Science*, 340 (6130), 280–1.

Andreae, M. O. and Rosenfeld, D., 2008. Aerosol-cloud-precipitation interactions. Part 1. The nature and sources of cloud-active aerosols. *Earth-Science Rev.*, 89, 13–41.

Andreae, M. O., Rosenfeld, D., Artaxo, P., Costa, A. A., Frank, G. P., Longo, K. M., and Silva-Dias, M. A. F., 2004. Smoking rain clouds over the Amazon. *Science*, 303 (5662), 1337–42.

Anttila, T., Kiendler-Scharr, A., Mentel, T. F., and Tillmann, R., 2007. Size dependent partitioning of organic material: Evidence for the formation of organic coatings on aqueous aerosols. *J. Atmos. Chem.*, 57 (3), 215–237.

Asa-Awuku, A., Nenes, A., Gao, S., Flagan, R. C., and Seinfeld, J. H., 2010. Water-soluble SOA from Alkene ozonolysis: composition and droplet activation kinetics inferences from analysis of CCN activity. *Atmos. Chem. Phys.*, 10 (4), 1585–1597.

Bela, M. M., Longo, K. M., Freitas, S. R., Moreira, D. S., Beck, V., Wofsy, S. C., Gerbig, C., Wiedemann, K., Andreae, M. O., and Artaxo, P., 2015. Ozone production and transport over the Amazon Basin during the dry-to-wet and wet-to-dry transition seasons. *Atmos. Chem. Phys. Discuss.*, 14 (10), 14005–14070.

Bond, T. C., Doherty, S. J., Fahey, D. W., Forster, P. M., Berntsen, T. K., Deangelo, B. J., Flanner, M. G., Ghan, S., Kärcher, B., Koch, D., Kinne, S., Kondo, Y., Quinn, P. K., Sarofim, M. C., Schultz, M. G., Schulz, M., Venkataraman, C., Zhang, H., Zhang, S., Bellouin, N., Guttikunda, S. K., Hopke, P. K., Jacobson, M. Z., Kaiser, J. W., Klimont, Z., Lohmann, U., Schwarz, J. P., Shindell, D., Storelvmo, T., Warren, S. G., and Zender, C. S., 2013. Bounding the role of black carbon in the climate system: A scientific assessment. *J. Geophys. Res. Atmos.*, 118 (11), 5380–5552.

Bond, T. C., Streets, D. G., Yarber, K. F., Nelson, S. M., Woo, J., and Klimont, Z., 2004. A technology-based global inventory of black and organic carbon emissions from combustion. *J. Geophys. Res.*, 109 (D14), D14203.

Brem, B. T., Mena Gonzalez, F. C., Meyers, S. R., Bond, T. C., and Rood, M. J., 2012. Laboratory-Measured Optical Properties of Inorganic and Organic Aerosols at Relative Humidities up to 95%. *Aerosol Sci. Technol.*, 46 (2), 178–190.

Chen, Y. and Bond, T. C., 2010. Light absorption by organic carbon from wood combustion. *Atmos. Chem. Phys.*, 10 (4), 1773–1787.

Chuang, P. Y., 2003. Measurement of the timescale of hygroscopic growth for atmospheric aerosols. *J. Geophys. Res.*, 108 (D9), 1–13.

Dinar, E., Anttila, T., and Rudich, Y., 2008. CCN activity and hygroscopic growth of organic aerosols following reactive uptake of ammonia. *Environ. Sci. Technol.*, 42 (3), 793–799.

Dusek, U., Covert, D. S., Wiedensohler, A., Neusüss, C., Weise, D., and Cantrell, W., 2003. Cloud condensation nuclei spectra derived from size distributions and hygroscopic properties of the aerosol in coastal south-west Portugal during ACE-2. *Tellus, Ser. B Chem. Phys. Meteorol.*, 55 (1), 35–53.

Dusek, U., Frank, G. P., Massling, A., Zeromskiene, K., Iinuma, Y., Schmid, O., Helas, G., Hennig, T., Wiedensohler, A., and Andreae, M. O., 2011. Water uptake by biomass burning aerosol at sub- and supersaturated conditions: closure studies and implications for the role of organics. *Atmos. Chem. Phys.*, 11 (18), 9519–9532.

Engelhart, G. J., Asa-Awuku, A., Nenes, A., and Pandis, S. N., 2008. CCN activity and droplet growth kinetics of fresh and aged monoterpene secondary organic aerosol. *Atmos. Chem. Phys.*, 8 (14), 3937–3949.

Evans, R. J. and Milne, T. A., 1987. Molecular characterization of the pyrolysis of biomass. 1. Fundamentals. *Energy & Fuels*, 1 (2), 123–137.

Feingold, G. and Chuang, P. Y., 2002. Analysis of the Influence of Film-Forming Compounds on Droplet Growth: Implications for Cloud Microphysical Processes and Climate. *J. Atmos. Sci.*, 59 (12), 2006–2018.

Fierce, L., Riemer, N., and Bond, T. C., 2013. When is cloud condensation nuclei activity sensitive to particle characteristics at emission? *J. Geophys. Res. Atmos.*, 118 (24), 13,476-13,488.

Fiore, A., 2003. Variability in surface ozone background over the United States: Implications for air quality policy. *J. Geophys. Res.*, 108 (D24).

Gysel, M., McFiggans, G., and Coe, H., 2009. Inversion of tandem differential mobility analyser (TDMA) measurements. *J. Aerosol Sci.*, 40, 134–151.

Hennigan, C. J., Westervelt, D. M., Riipinen, I., Engelhart, G. J., Lee, T., Collett, J. L., Pandis, S. N., Adams, P. J., and Robinson, A. L., 2012. New particle formation and growth in biomass burning plumes: An important source of cloud condensation nuclei. *Geophys. Res. Lett.*, 39 (9), 1–5.

Kanakidou, M., Seinfeld, J. H., Pandis, S. N., Barnes, I., Dentener, F. J., Facchini, M. C., Van Dingenen, R., Ervens, B., Nenes, a., Nielsen, C. J., Swietlicki, E., Putaud, J. P., Balkanski, Y., Fuzzi, S., Horth, J., Moortgat, G. K., Winterhalter, R., Myhre, C. E. L., Tsigaridis, K., Vignati, E., Stephanou, E. G., and Wilson, J., 2005. Organic aerosol and global climate modelling: a review. *Atmos. Chem. Phys.*, 5 (4), 1053–1123.

Köhler, H., 1936. The nucleus in and the growth of hygroscopic droplets. *Trans. Faraday Soc.*, 32 (0), 1152–1161.

Lambe, A. T., Ahern, A. T., Wright, J. P., Croasdale, D. R., Davidovits, P., and Onasch, T. B., 2015. Oxidative aging and cloud condensation nuclei activation of laboratory combustion soot. *J. Aerosol Sci.*, 79, 31–39.

Lathem, T. L. and Nenes, A., 2011. Water Vapor Depletion in the DMT Continuous-Flow CCN Chamber: Effects on Supersaturation and Droplet Growth. *Aerosol Sci. Technol.*, 45 (5), 604–615.

Lewin, E. E., De Pena, R. G., and Shimshock, J. P., 1986. Atmospheric gas and particle measurement at a rural northeastern U.S. site. *Atmos. Environ. - Part A Gen. Top.*, 20 (1), 59–70.

Li, Z., Williams, A. L., and Rood, M. J., 1998. Influence of Soluble Surfactant Properties on the Activation of Aerosol Particles Containing Inorganic Solute. *J. Atmos. Sci.*, 55 (10), 1859–1866.

Mircea, M., Facchini, M. C., Decesari, S., Cavalli, F., Emblico, L., Fuzzi, S., Vestin, A., Rissler, J., Swietlicki, E., Frank, G., Andreae, M. O., Maenhaut, W., Rudich, Y., and Artaxo, P., 2005. Importance of the organic aerosol fraction for modeling aerosol hygroscopic growth and activation: a case study in the Amazon Basin. *Atmos. Chem. Phys. Discuss.*, 5 (4), 5253–5298.

Myhre, G., Shindell, D., Bréon, F.-M., Collins, W., Fuglestvedt, J., Huang, J., Koch, D., Lamarque, J. F., Lee, D., Mendoza, B., Nakajima, T., Robock, A., Stephens, G., Takemura, T., and Zhang, H., 2013. 2013: Anthropogenic and Natural Radiative Forcing. *Clim. Chang. 2013 Phys. Sci. Basis. Contrib. Work. Gr. I to Fifth Assess. Rep. Intergov. Panel Clim. Chang.*, 659–740.

Petters, M. D., Carrico, C. M., Kreidenweis, S. M., Prenni, A. J., DeMott, P. J., Collett, J. L., and Moosmüller, H., 2009. Cloud condensation nucleation activity of biomass burning aerosol. *J. Geophys. Res. Atmos.*, 114 (22).

Petters, M. D. and Kreidenweis, S. M., 2007. A single parameter representation of hygroscopic growth and cloud condensation nucleus activity. *Atmos. Chem. Phys.*, 7 (8), 1961–1971.

Petters, M. D., Prenni, A. J., Kreidenweis, S. M., DeMott, P. J., Matsunaga, A., Lim, Y. B., and Ziemann, P. J., 2006. Chemical aging and the hydrophobic-to-hydrophilic conversion of carbonaceous aerosol. *Geophys. Res. Lett.*, 33 (24), 1–5.

Rader, D. J. and McMurry, P. H., 1986. Application of the tandem differential mobility analyzer to studies of droplet growth or evaporation. *J. Aerosol Sci.*, 17 (5), 771–787.

Ramanathan, V., Ramana, M. V., Roberts, G. C., Kim, D., Corrigan, C., Chung, C., and Winker, D., 2007. Warming trends in Asia amplified by brown cloud solar absorption. *Nature*, 448 (7153), 575–578.

Reutter, P., Trentmann, J., Su, H., Simmel, M., Rose, D., Wernli, H., Andreae, M. O., and Pöschl, U., 2009. Aerosol- and updraft-limited regimes of cloud droplet formation: influence of particle number, size and hygroscopicity on the activation of cloud condensation nuclei (CCN). *Atmos. Chem. Phys. Discuss.*, 9 (2), 8635–8665.

Roberts, G. C., Nenes, A., Seinfeld, J. H., and Andreae, M. O., 2003. Impact of biomass burning on cloud properties in the Amazon Basin. *J. Geophys. Res.*, 108 (D2).

Rudich, Y., Donahue, N. M., and Mentel, T. F., 2007. Aging of organic aerosol: Bridging the gap between laboratory and field studies. *Annu. Rev. Phys. Chem.*

Ruehl, C. R., Chuang, P. Y., and Nenes, A., 2007. How quickly do cloud droplets form on atmospheric particles? *Atmos. Chem. Phys. Discuss.*, 7 (5), 14233–14264.

Slade, J. H. and Knopf, D. A., 2013. Heterogeneous OH oxidation of biomass burning organic aerosol surrogate compounds: assessment of volatilisation products and the role of OH concentration on the reactive uptake kinetics. *Phys. Chem. Chem. Phys.*, 15 (16), 5898–5915.

Slade, J. H., Thalman, R., Wang, J., and Knopf, D. A., 2015. Chemical aging of single and multicomponent biomass burning aerosol surrogate-particles by OH: implications for cloud condensation nucleus activity. *Atmos. Chem. Phys. Discuss.*, 15 (5), 6771–6819.

Spracklen, D. V., Carslaw, K. S., Pöschl, U., Rap, A., and Forster, P. M., 2011. Global cloud condensation nuclei influenced by carbonaceous combustion aerosol. *Atmos. Chem. Phys.*, 11 (17), 9067–9087.

Stier, P., Feichter, J., Kloster, S., Vignati, E., and Wilson, J., 2006. Emission-induced nonlinearities in the global aerosol system: Results from the ECHAM5-HAM aerosol-climate model. *J. Clim.*, 19 (16), 3845–3862.

Trebs, I., Meixner, F. X., Slanina, J., Otjes, R., Jongejan, P., and Andreae, M. O., 2004. Real-time measurements of ammonia, acidic trace gases and water-soluble inorganic aerosol species at a rural site in the Amazon Basin. *Atmos. Chem. Phys. Discuss.*, 4 (1), 1203–1246.

Trebs, I., Metzger, S., Meixner, F. X., Helas, G., Hoffer, A., Rudich, Y., Falkovich, A. H., Moura, M. L., Da Silva, R. S., Artaxo, P., Slanina, J., and Andreae, M. O., 2005. The NH4+-NO3 --Cr-SO4 2--H2O aerosol system and its gas phase precursors at a pasture site in the Amazon Basin: How relevant are mineral cations and soluble organic acids? *J. Geophys. Res. Atmos.*, 110 (7), 1–18.

Twomey, S., 1977. The Influence of Pollution on the Shortwave Albedo of Clouds. *J. Atmos. Sci.*, 34, 1149–1152.

Winter, K. E., 2002. Control of Relative Humidity in an Automated Nephelometer System for Ambient Aerosol Measurements. Master's Thesis, Master’s Thesis, University of Illinois at Urbana-Champaign.

Wu, Z. J., Nowak, A., Poulain, L., Herrmann, H., and Wiedensohler, A., 2011. Hygroscopic

behavior of atmospherically relevant water-soluble carboxylic salts and their influence on the water uptake of ammonium sulfate. *Atmos. Chem. Phys.*, 11 (24), 12617–12626.

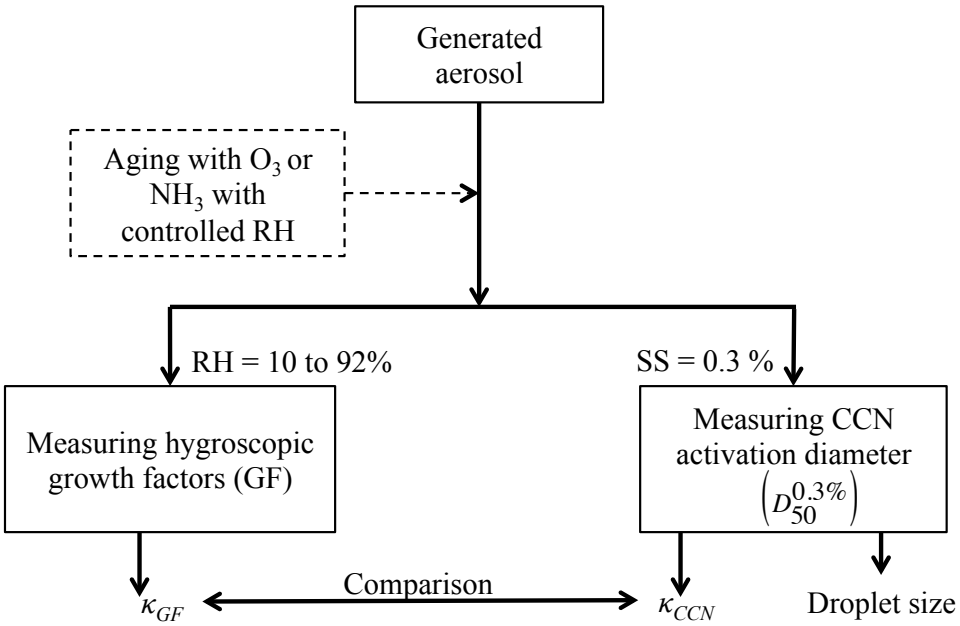

Figure 1. Overview of research approach (dashed borders indicate activities that were only implemented in some tests).

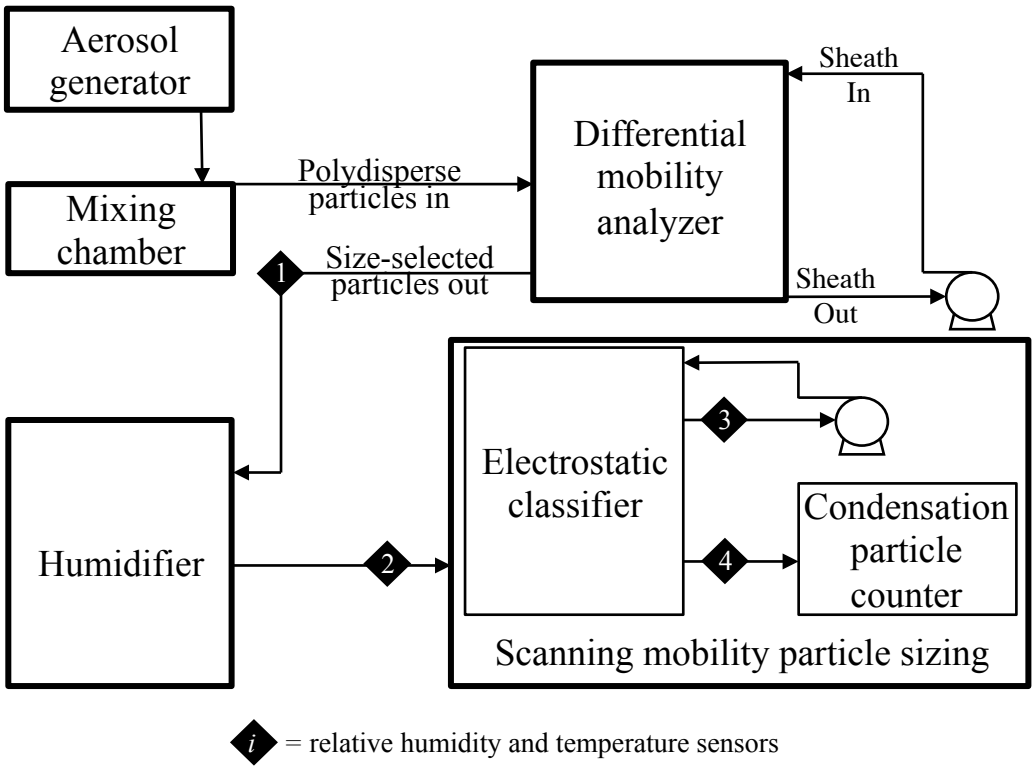

Figure 2. Experimental setup for hygroscopic growth measurements.

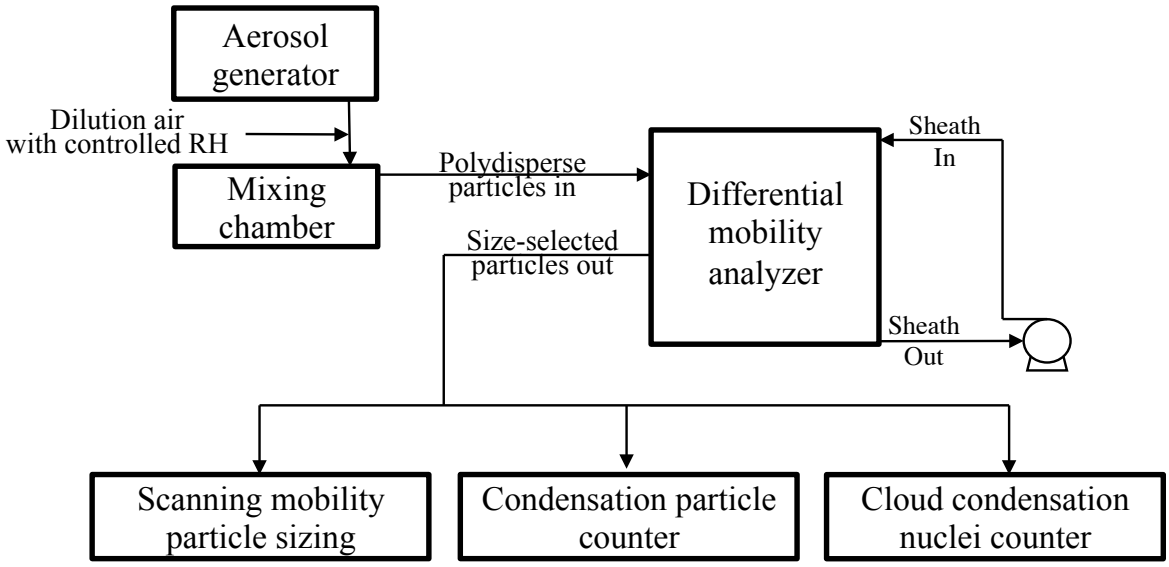

Figure 3. Experimental setup for CCN activity measurements.

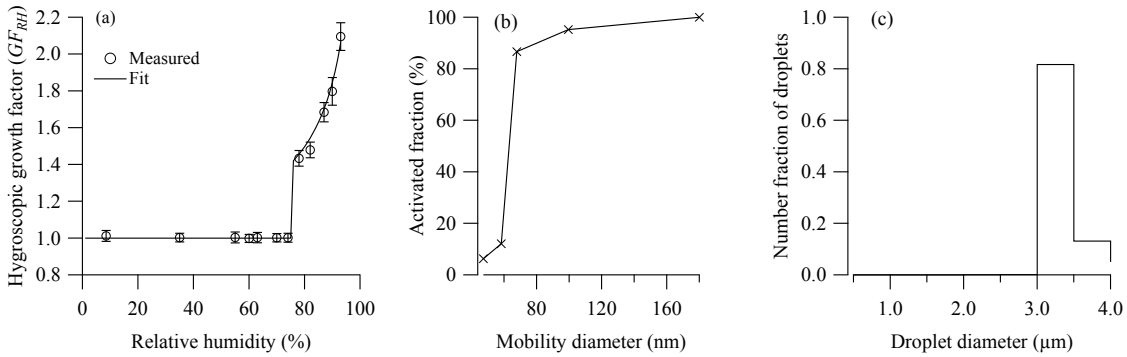

Figure 4. Results of tests with ammonium sulfate: (a) hygroscopic growth of particles of 100 nm dry diameter, (b) Size-resolved CCN activity at 0.3% *SS* and (c) size distribution of droplets activated at 0.3% *SS*.

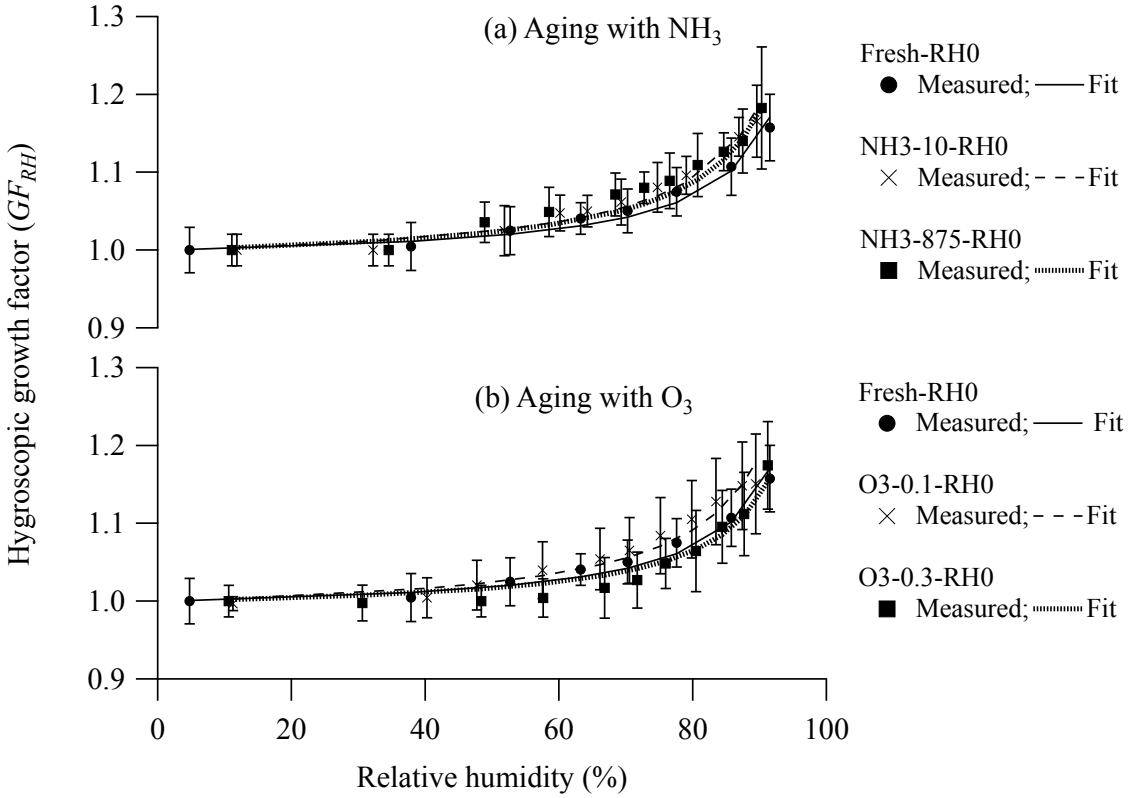

Figure 5. Hygroscopic growth of OC particles fresh and aged with (a) 10 and 875 ppm_v NH_3 and (b) 0.1 and 0.3 ppm_v O_3.

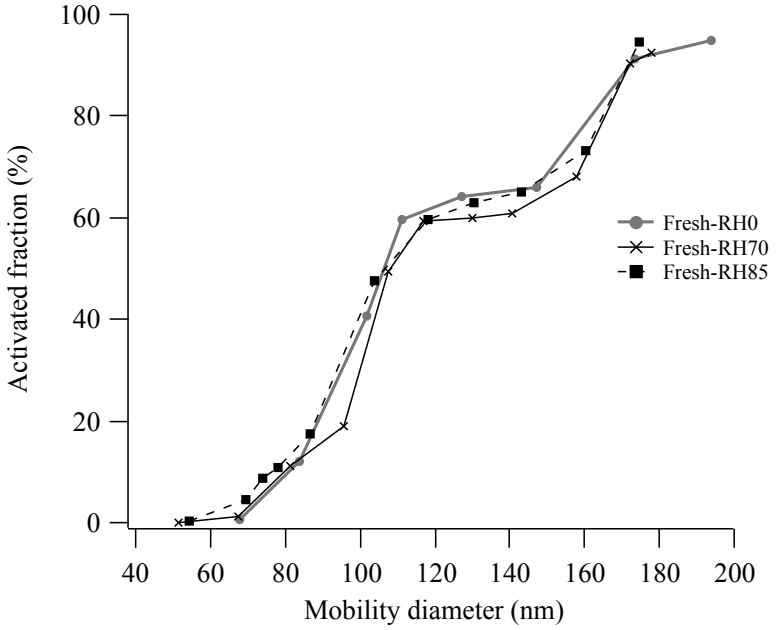

Figure 6. Effect of water vapor aging on CCN activation of fresh OC particles at 0.3% *SS*.

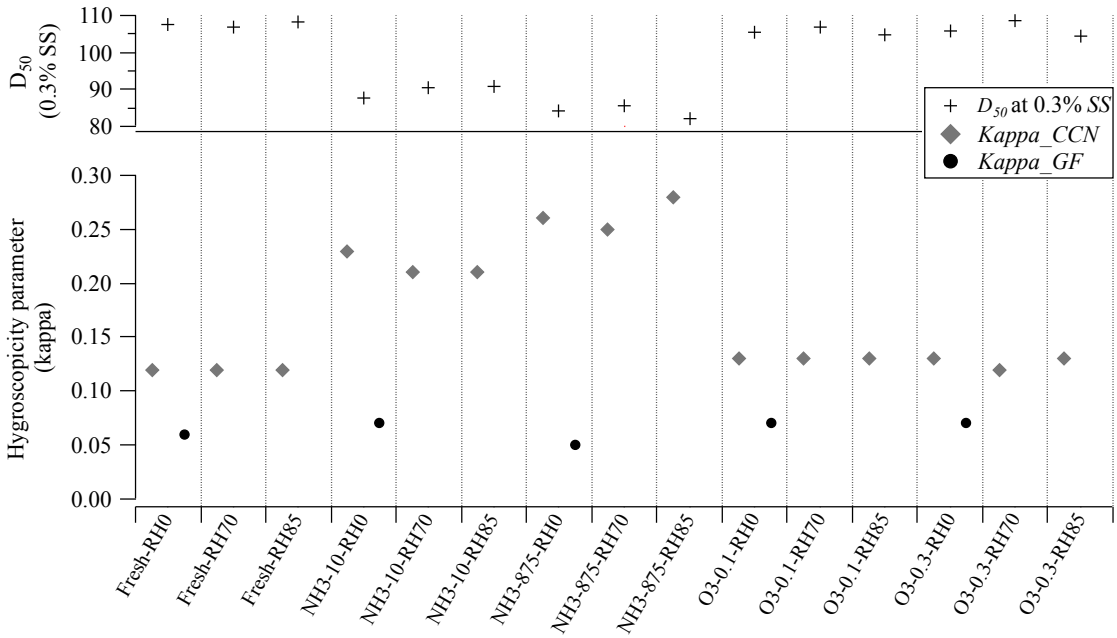

Figure 7. Summary of inferred values describing hygroscopic growth and CCN activity.

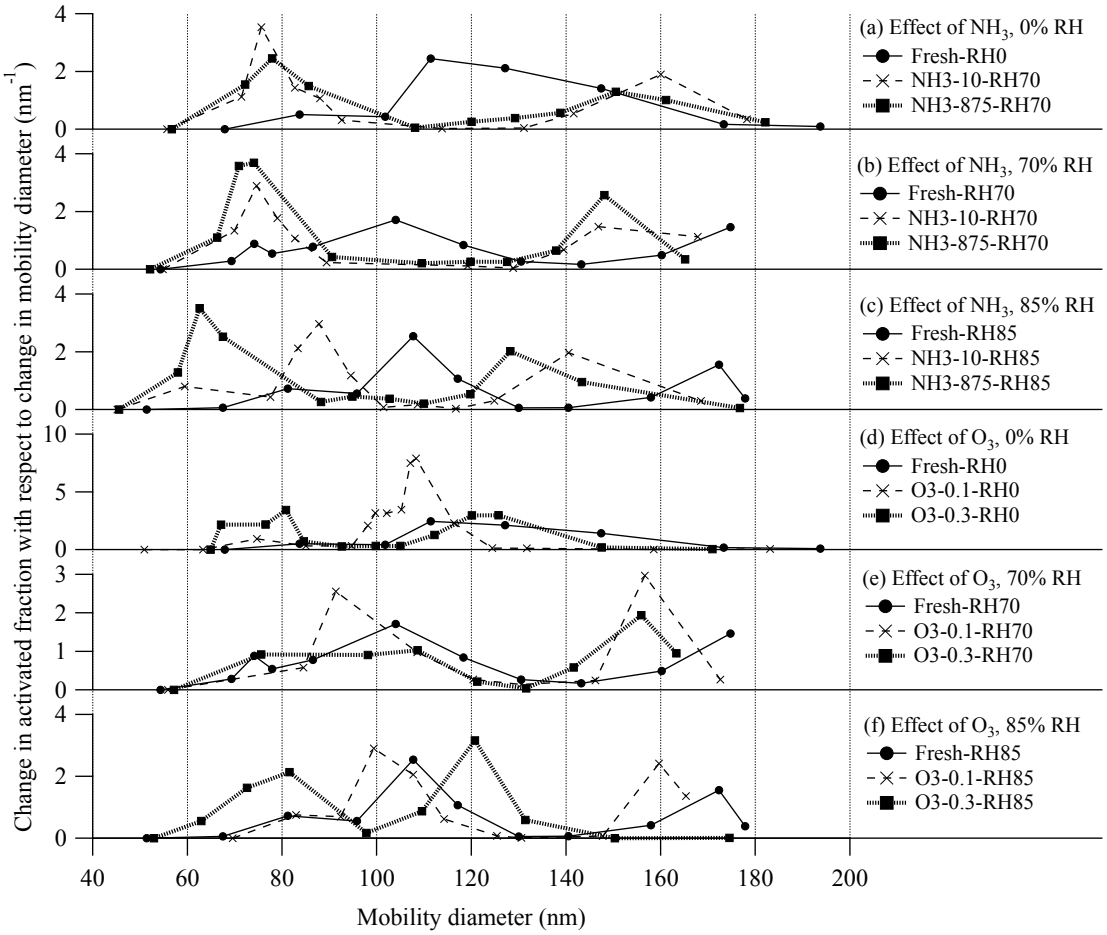

Figure 8. Differential CCN activation spectra of fresh and aged OC particles.

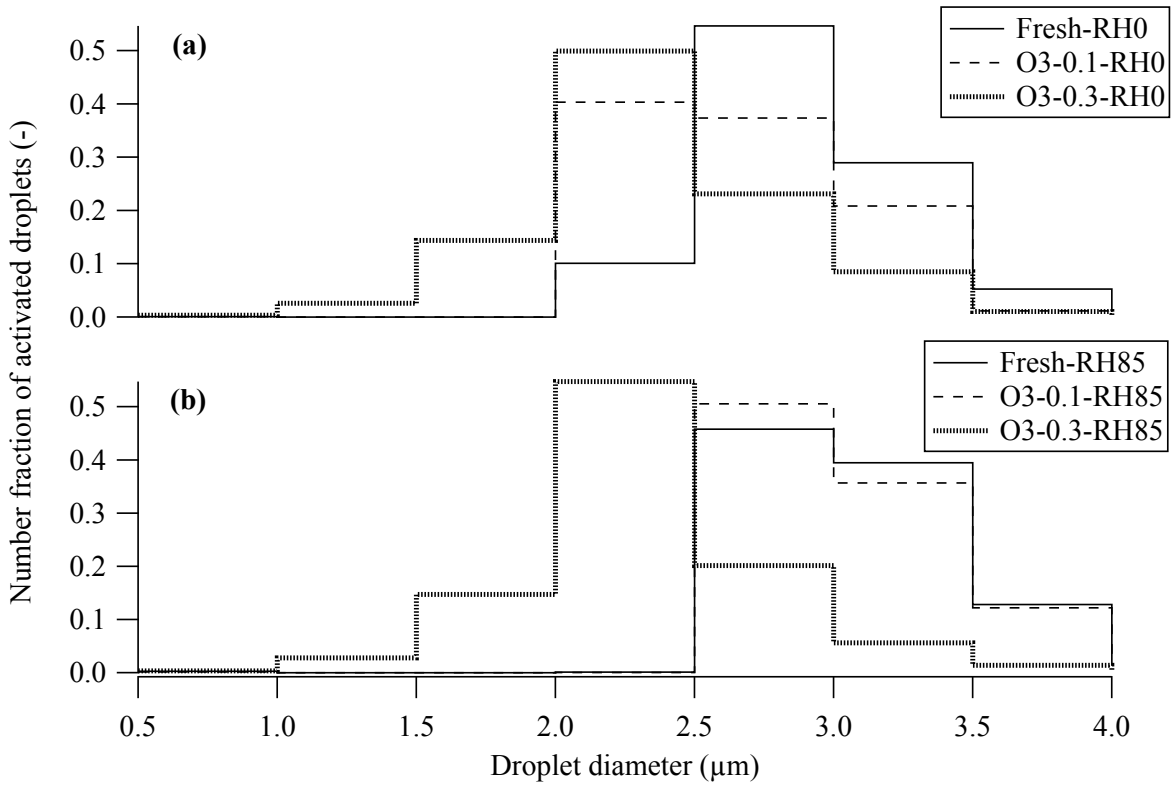

Figure 9. Size distribution of droplets exiting cloud chamber after activation of 130 nm CCN at 0.3% SS; Particles initially aged in 0.1 and 0.3 ppm_v O_3 with (a) 0% RH and (b) 85% RH.

Table 1. Summary of GF_{RH} and CCN activity tests.

Aging ID	GF_{RH} measured?	Aging conditions			
		Chemical	ppm_v of chemical	RH during aging (%)	Duration of aging (min)
AS*	Yes	N/A	N/A	0	N/A
Fresh-RH0	Yes	N/A	N/A	0	N/A
Fresh-RH70	No	N/A	N/A	70	N/A
Fresh-RH85	No	N/A	N/A	85	N/A
NH3-10-RH0	Yes	NH_3	10	0	10
NH3-10-RH70	No	NH_3	10	70	10
NH3-10-RH85	No	NH_3	10	85	10
NH3-875-RH0	Yes	NH_3	875	0	10
NH3-875-RH70	No	NH_3	875	70	10
NH3-875-RH85	No	NH_3	875	85	10
O3-0.1-RH0	Yes	O_3	0.1	0	5
O3-0.1-RH70	No	O_3	0.1	70	5
O3-0.1-RH85	No	O_3	0.1	85	5
O3-0.3-RH0	Yes	O_3	0.3	0	5
O3-0.3-RH70	No	O_3	0.3	70	5
O3-0.3-RH85	No	O_3	0.3	85	5

*AS = ammonium sulfate; N/A = not applicable; OC was the seed aerosol in all tests except AS

Appendix C.
Light absorption of organic aerosol from pyrolysis of corn stalk

X. Li, Y. Chen, and T. C. Bond

Summary of paper published in Atmospheric Environment

ABSTRACT. Organic aerosol (OA) can absorb radiation in the low-visible and ultra-violet wavelengths thereby modifying radiative forcing. Agriculture waste burning emits a large quantity of organic carbon in many developing countries. In this work, we examined light absorbing properties of primary OA from pyrolysis of corn stalk, a major agriculture waste in developing countries. Light absorption of bulk liquid extracts of OA was measured using a UV-vis recording spectrophotometer. OA can be extracted by methanol at 95%, close to full extent, and shows polar character. Light absorption of organic aerosol has strong spectral dependence (Absorption Ångström exponent = 7.7) and should not be negligible at shorter wavelengths. Higher pyrolysis temperature produced OA with higher absorption. Imaginary refractive index of organic aerosol (k_{OA}) are 0.041 at 400nm wavelength and 0.005 at 550nm wavelength, respectively. An inter-comparison study of different methods to determine light absorbing properties of OC is suggested to conduct in the future.

1. Rationale

Since biofuel combustion and biomass open burning contributes about 90% of total primary OC (Bond et al., 2004), investigation on the light absorbing properties of primary OC has been focused on this type of source. However, most of them concern wood combustion, duff combustion, savanna and forest fire (Kirchstetter et al. 2004; Chen and Bond 2010; Chakrabarty et al., 2010; Lack et al., 2012; Saleh et al., 2013; 2014). Agriculture wastes are often burned in the field after harvesting and used as fuel for cooking and heating in the developing countries (Li et al, 2007, 2009). They contribute 9% to global annual OC emission and 27.5% to its emission in China (Bond et al., 2004; Cao et al., 2006). Only two studies have examined light absorption of OA from burning of rice straw (Favez et al., 2009; Saleh et al., 2014), and it is not known whether OA from waste of other crops, which is structurally different, has similar properties.

2. Method

Corn stalks were collected after harvest from a field near the University of Illinois at Urbana-Champaign (UIUC). The corn stalks were put in the lab and dried for over a week and then cut into pieces about 4 cm in length.

Organic aerosol was generated by pyrolyzing pieces of corn stalks in a temperature-controlled pyrolysis reactor as described by Chen and Bond (2010) and Brem et al. (2011). Before installation in the reactor, corn stalk pieces were purged with N_2 and vacuumized, and then soaked in N_2 for over one day, which can remove oxygen within the corn stalk and prevent BC production during the pyrolysis. In order to investigate the effect of pyrolysis temperature on OC absorption, the experiments were carried out under 3 different temperatures, 210 ^{o}C, 270 ^{o}C, 360 ^{o}C based on biomass

thermal degradation behavior (White and Dietenberger, 2001). In each run, 3 pieces of corn stack were pyrolyzed sequentially and the pyrolysis lasted for about 10 minutes. The pyrolysis procedure was aimed to simulate the release of organic aerosol from corn stalk smoldering combustion. Due to relatively low temperature at the smoldering stage, pyrolysis product was released from the corn stalk and escaped from the reactor and then part of the pyrolysis product formed organic aerosol through condensation in the cooling plume. Sampling occurred as described in Appendix B and absorption measurements were as in Chen and Bond (2010).

3. Results

In this study, we investigated three different pyrolysis temperatures: 210 oC, 270 oC, 360 oC. Actual temperature varied 10oC from the nominal temperature. Figure 1 shows average and standard deviation of absorption per mass of organic carbon (α/ρ) at three pyrolysis temperatures. It illustrates that α/ρ increases with increasing pyrolysis temperatures in this temperature range. For example, an increase from 210 oC to 270 oC and 210 oC to 360 oC results in approximately 20% and 50% increase of α/ρ (average in ultraviolet range), respectively. However, the degree of α/ρ increase with temperature is much lower than that of wood pyrolysis (Chen and Bond, 2010). Difference in α/ρ with wood pyrolysis generated at 210 oC and 360 oC was consistently observed. The discrepancy may due to the difference in fuel structure. It has been supposed that polymerization resulted in greater absorption per mass (Chen and Bond, 2010). Corn stalk has a looser fiber structure relative to wood. OC precursors may release from corn stalk more easily than wood, and hence have less residence time in the corn stalk, which may increase heating rate but weaken polymerization at higher temperatures. Nevertheless, Figure 1 shows that maximum absorption is very similar to that of wood pyrolysis aerosol.

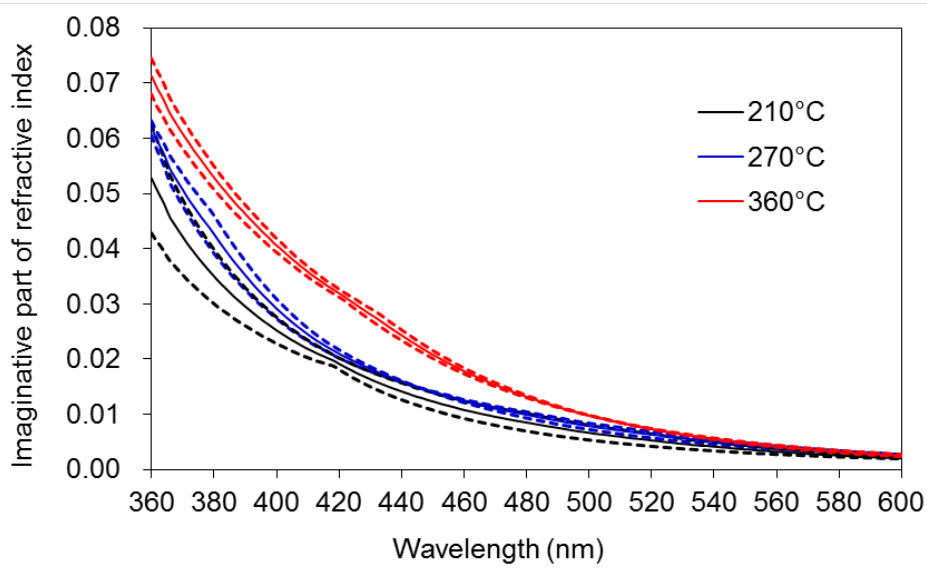

Figure 1 Average imaginary part of refractive index (kOA) at three pyrolysis temperatures. Dashed lines with the same color indicate upper and lower range.

Appendix D.

AEROSOL SCIENCE AND TECHNOLOGY
http://dx.doi.org/10.1080/02786826.2017.1311988

Simulating aerosol chamber experiments with the particle-resolved aerosol model PartMC

J. Tian[a], B. T. Brem[b], M. West[c], T. C. Bond[d], M. J. Rood[d], and N. Riemer[a]

[a]Department of Atmospheric Sciences, University of Illinois at Urbana-Champaign, Urbana, Illinois, USA; [b]Advanced Analytical Technologies Laboratory, EMPA, Dübendorf, Switzerland; [c]Department of Mechanical Science and Engineering, University of Illinois at Urbana-Champaign, Urbana, Illinois, USA; [d]Department of Civil and Environmental Engineering, University of Illinois at Urbana-Champaign, Urbana, Illinois, USA

ABSTRACT
This article presents a verification and validation study of the stochastic particle-resolved aerosol model PartMC. Model verification was performed against self-preserving analytical solutions, while for validation three experiments were performed where the size distribution evolution of coagulating ammonium sulfate particles was measured in a cylindrical stainless steel chamber. To compare with the chamber measurements, PartMC was extended to include the representation of fractal particle structure and wall loss. This introduced five unknown parameters to the governing equation, which were determined by a combination of scanning electron microscopy (SEM) analysis and an objective optimization procedure. Excellent agreement between modeled and measured size distributions was achieved using the same set of parameters for all three experiments. Assuming spherical particles led to model results that were inconsistent with the measurements. The best agreement between model and measurement was obtained for the fractal dimension of 2.3, indicating that the non-spherical structure of the particle agglomerates in the chamber needed to be taken into account.

ARTICLE HISTORY
Received 29 September 2016
Accepted 9 March 2017

EDITOR
Yannis Drossinos

1. Introduction

Stochastic particle methods are widely used across different communities in science and engineering. Gillespie (1975) set a milestone in applying this technique to the evolution of physical particle populations by developing the exact stochastic simulation algorithm (SSA) to simulate the collision of cloud droplets. Since then many studies have developed this method further (Eibeck and Wagner 2001; Gillespie et al. 2009; Roh et al. 2011). Variants of this method have been used to investigate the evolution of specific particle systems, for example, for aerosol applications in industry (Wells et al. 2006; Shekar et al. 2012), astrophysics (Ormel and Spaans 2008; Okuzumi et al. 2009), oceanography (Jokulsdottir and Archer 2016), and atmospheric sciences (Shima et al. 2009; Riemer et al. 2009).

This article applies the stochastic particle-resolved "Particle Monte Carlo" model PartMC (Riemer et al. 2009) to the simulation of aerosol particles in an aerosol chamber. PartMC was developed to simulate the evolution of aerosol particles in the atmosphere. Atmospheric aerosol particles typically consist of a complex mixture of different chemical species, with sizes ranging from a few nanometers to tens of micrometers (Pöschl 2005; Seinfeld and Pandis 2006; Kolb and Worsnop 2012). The particle-resolved approach is suitable for modeling such a system, as it explicitly resolves the full composition space without any *a priori* assumptions about particle composition. Since the per-particle composition governs the aerosols' optical properties and their ability to form cloud droplets, these details are important for determining the aerosol impact on climate (Zaveri et al. 2010).

The PartMC model was coupled with the state-of-the-art aerosol chemistry model MOSAIC (Zaveri et al. 2008) to treat gas chemistry, particle phase thermodynamics, and dynamic gas-particle mass transfer. PartMC-MOSAIC has been used to simulate aerosol processes in the atmosphere for a wide range of topics. For example, Riemer et al. (2010) and Fierce et al. (2015) applied the model to quantify black carbon aging time

CONTACT N. Riemer nriemer@illinois.edu Department of Atmospheric Sciences, University of Illinois at Urbana-Champaign, 105 S Gregory St., Urbana, IL 61801, USA.

Color versions of one or more of the figures in the article can be found online at www.tandfonline.com/uast.

Supplemental data for this article can be accessed on the publisher's website.

© 2017 American Association for Aerosol Research

scales. Ching et al. (2012) and Ching et al. (2016) investigated the impact of aerosol mixing state on cloud droplet formation. Other model applications included the heterogenous oxidation of soot surfaces (Kaiser et al. 2011), and the characterization of the aerosol evolution in ship plumes (Tian et al. 2014).

The contributions of this study are the verification and validation of PartMC to simulate aerosol processes in a chamber environment. We use the term "verification" here to refer to "the process of determining that a computational model accurately represents the underlying mathematical model and its solution," and "validation" to refer to "the process of determining the degree to which a model is an accurate representation of the real world from the perspective of the intended uses of the model" (ASME 2006). This study not only necessitated implementing chamber-specific loss processes such as wall loss and sedimentation, but also required representing fractal-like agglomerates and developing an objective optimization procedure to estimate required model parameters. As such, this article lays the foundation for using PartMC as a tool to interpret and design aerosol chamber experiments in the future.

The manuscript is organized as follows. Section 2 states the governing equation for the evolution of the population in the chamber environment and describes the treatments of wall loss and fractal particle dynamics in our PartMC model. Section 3 presents the verification of the coagulation code using self-preserving size distributions. Section 4 describes the chamber experiments and presents the code validation procedure, and Section 5 summarizes our findings.

2. Model description

2.1. Governing equation for the chamber environment

Our aim was to simulate the evolution of an aerosol particle population after it is introduced into an aerosol chamber. To isolate the impact of coagulation and wall loss on the size distribution evolution, additional particle emissions are not introduced after the start of the simulation. Further, we consider only the evolution of a single, non-volatile aerosol species in the chamber, excluding gas-to-particle conversion and aerosol chemistry in our current model framework. The relevant processes are therefore coagulation, dilution, and wall losses due to diffusion and sedimentation. We assume that the aerosol population in the chamber is well-mixed, which justifies a box model approach. The differential equation governing the time evolution of the aerosol size distribution $n(\mu,t)$ in the chamber environment is

$$\begin{aligned}\frac{\partial n(\mu,t)}{\partial t} = & \underbrace{\frac{1}{2}\int_0^{\mu} K(\nu,\mu-\nu)n(\nu,t)n(\mu-\nu,t)d\nu}_{\text{coagulation gain}} \\ & - \underbrace{\int_0^{\infty} K(\mu,\nu)n(\mu,t)n(\nu,t)d\nu}_{\text{coagulation loss}} \\ & - \underbrace{n(\mu,t)\lambda_{\text{dil}}(t)}_{\text{dilution}} - n(\mu,t)(\underbrace{\alpha_{\mu}^{\text{D}}(t)}_{\text{wall diffusion}} \\ & + \underbrace{\alpha_{\mu}^{\text{S}}(t)}_{\text{sedimentation}}). \end{aligned} \quad [1]$$

In Equation (1), $K(\mu,\nu)$ (m^3s^{-1}) is the coagulation coefficient between particles with constituent masses μ and ν, $n(\mu, t)$ ($\text{m}^{-3}\,\text{kg}^{-1}$) is the aerosol number distribution at time t, $\lambda_{\text{dil}}(t)$ (s^{-1}) is the dilution rate, and $\alpha^{\text{D}}(t)$ (s^{-1}) and $\alpha^{\text{S}}(t)$ (s^{-1}) are the wall loss rate coefficients due to diffusion and sedimentation, respectively.

2.2. The PartMC simulation algorithm

PartMC is a 0-D or box model that solves Equation (1). It explicitly resolves the composition of many individual aerosol particles within a well-mixed computational volume, making this a "particle-resolved" simulation. A detailed description of the numerical methods used in PartMC is given in Riemer et al. (2009) and DeVille et al. (2011). The code is open-source under the GNU General Public License (GPL) version 2 and can be downloaded at http://lagrange.mechse.illinois.edu/partmc/.

In brief, the particle population in the volume of interest is resolved by a large number of discrete computational particles, in our applications typically on the order of 10^4 to 10^6. The relative positions of particles within the computational volume are not tracked. Over the course of the simulation, the mass of each constituent species within each particle is tracked. The relevant processes for this study, namely, Brownian coagulation, dilution, and wall losses due to diffusion and sedimentation, are simulated with a stochastic Monte Carlo approach by generating a realization of a Poisson process. Using the "weighted flow algorithm" by DeVille et al. (2011) improves the model efficiency and reduces ensemble variance.

We used 10^5 computational particles to initialize the simulations shown in this article. If the number of computational particles drops below half of the initial number because of the various loss processes, the number of particles is doubled by duplicating each particle, which corresponds to a doubling of the computational volume. This is a common Monte Carlo particle modeling approach to maintain accuracy (Liffman 1992). To quantify the stochastic error of the PartMC simulations, we repeated each simulation with different random seeds and calculated means and standard deviations. The number of repeats, N_{run}, was set to 10 in our case. The standard deviation of the size distribution obtained from the ensemble runs is the uncertainty from PartMC, denoted by σ_{partmc}, which is divided by $\sqrt{N_{\mathrm{run}}}$ to obtain the uncertainty in the mean (the SEM or standard error of the mean).

For the code development in this study, we branched from PartMC version 2.2.0 to implement the chamber wall loss treatment (Section 2.3), and extended the treatment of Brownian coagulation to include fractal particles (Section 2.4). The additions are available in version 2.4.0.

2.3. Chamber wall loss treatment

A challenge for chamber studies arises from quantifying wall losses due to particle diffusion and sedimentation to the chamber wall. Misestimation of these wall losses can result in inaccurate interpretation of the experimental results, as shown, for example, for secondary aerosol yield measurements by Matsunaga and Ziemann (2010). Modeling wall loss is difficult because the process can depend on aerosol particle size, the material of the chamber, the electric charge distribution, and the turbulence in the chamber. Past studies have proposed detailed formulations to quantify the wall loss rate (Crump and Seinfeld 1981; McMurry and Rader 1985; Park et al. 2001; Verheggen and Mozurkewich 2006). They often introduce parameters that are difficult to constrain and that might vary between different experiments. Therefore, inverse approaches that use size distribution measurements to constrain these unknown parameters are often conducted to obtain the functional forms of wall loss rate (Pierce et al. 2008).

In this study, we followed the method to parameterize wall losses by Naumann (2003), which is based on Fuchs (1964) and van de Vate and ten Brink (1980). The wall loss rates due to diffusion and sedimentation are size-dependent and given by

$$\alpha_\mu^{\mathrm{D}} = \frac{D\left(R_{\mathrm{me},\mu}\right) A_{\mathrm{D}}}{\delta_{\mathrm{D}} V} \quad \text{and} \qquad [2]$$

$$\alpha_\mu^{\mathrm{S}} = \frac{4\pi\rho R_{\mathrm{m},\mu}^3 g D\left(R_{\mathrm{me},\mu}\right) A_{\mathrm{S}}}{3kTV}. \qquad [3]$$

In Equations (2) and (3), $D\left(R_{\mathrm{me},\mu}\right)$ ($\mathrm{m^2 s^{-1}}$) is the diffusion coefficient for particle μ, $R_{\mathrm{me},\mu}$ (m) is the particle mobility equivalent radius of particle μ, A_{D} ($\mathrm{m^2}$) is the diffusional deposition area, δ_{D} (m) is diffusional boundary layer thickness, and V ($\mathrm{m^3}$) is the volume of the chamber. The thickness δ_{D} has the following formulation based on Fuchs (1964) and Okuyama et al. (1986),

$$\delta_{\mathrm{D}} = k_{\mathrm{D}} \left(\frac{D}{D_0}\right)^a, \qquad [4]$$

where k_{D} (m) is a chamber-specific parameter that can vary between different experimental set-ups. The constant a is a coefficient that was theoretically determined by Fuchs (1964) to be 0.25, and $D_0 = 1\ \mathrm{m^2\,s^{-1}}$ is the unit diffusion coefficient, which is formally needed to obtain dimensional consistency. In Equation (3), $R_{\mathrm{m},\mu}$(m) is particle mass-equivalent radius of particle μ, and A_{S} ($\mathrm{m^2}$) is the sedimentation area. As shown in Section 4.2, the unknown parameters in the wall loss equations, k_{D} and a, are determined through an optimization procedure based on particle size distribution measurements.

2.4. Fractal particle treatment

Irregular, fractal-like particles, including soot (Lapuerta et al. 2006; Moldanová et al. 2009) and soot-inorganic mixtures (Wentzel et al. 2003), are ubiquitous in both natural environments and technical applications. In addition, fractal-like agglomerates can also be formed from packing of spherical primary particles (Eggersdorfer and Pratsinis 2014). These particles exhibit significantly different dynamics and optical properties from those of spherical particles (Chen et al. 1990; Wu and Friedlander 1993; Sorensen 2001; Pranami et al. 2010), such as enhanced coagulational growth due to the increased collision cross-section. In this study, we implemented the formalism of fractal particles described in Naumann (2003). As we will show in Section 4.3, this is essential to successfully model the evolution of the observed size distributions. Details of the model implementation can be found in Section 1 of the online supplemental information (SI). In general, the number of monomers, N, in a fractal-like agglomerate can be related to the particle geometric radius R_{geo} by

$$N = \frac{1}{f}\left(\frac{R_{\mathrm{geo}}}{R_0}\right)^{d_{\mathrm{f}}}, \qquad [5]$$

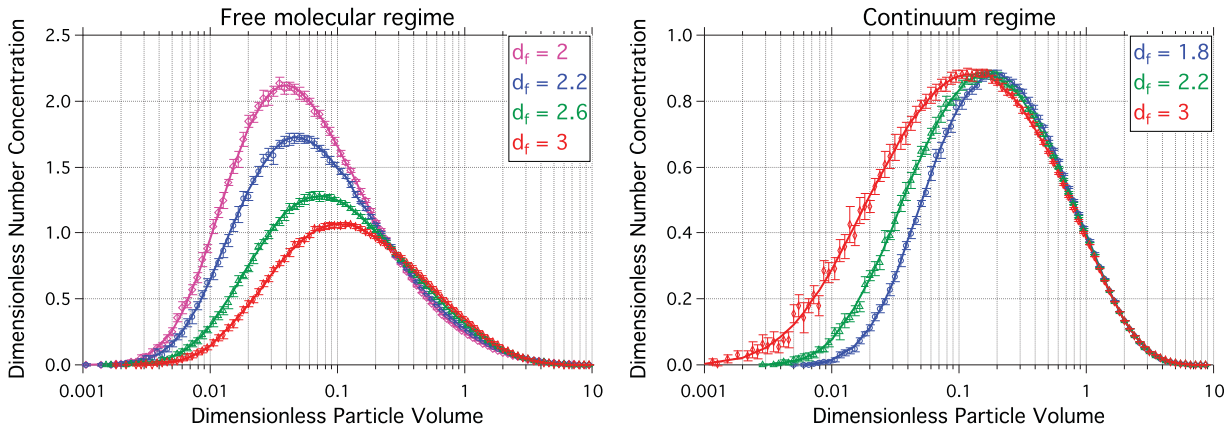

Figure 1. Self-preserving size distributions in the free molecular regime (left panel) and continuum regime (right panel) obtained from PartMC simulations (symbols) and the Vemury and Pratsinis (1995) code (lines) at different fractal dimensions (d_f). The error bars represent 95% confidence intervals from 10 ensemble runs. The self-preserving size distribution is defined in Equation (S-12).

where f is the volume filling factor quantifying how much of the available volume will be occupied by spherical monomers, R_0 (m) is the radius of the monomers, and d_f is the fractal (or Hausdorff) dimension that determines the growth rate of fractal agglomerates due to collision processes (Wu and Friedlander 1993). Similar to the wall loss parameters k_D and a, the fractal dimension d_f is an unknown parameter in our simulation, which will also be determined by the optimization procedure detailed in Section 4.2.

An important, implicit assumption of the Naumann (2003) formalism is that the number of monomers N is sufficiently large, i.e., larger than 100, as shown by the analysis in Sorensen (2011). Since in our case N is smaller than 100, care has to be taken with interpreting the results, and we will discuss this issue in detail in Section 4.3. We further assume the primary particles constructing the fractal agglomerates are non-overlapping, equal-size spheres (constant R_0) with homogenous density, which is a common assumption in theoretical analyses (Ulrich and Subramanian 1977; Koch and Friedlander 1990). We also assume that d_f and f will not change during the evolution of particles, although studies have argued that the fractal dimension may change as the size distribution of fractal agglomerates evolves (Kostoglou and Konstandopoulos 2001; Artelt et al. 2003). We will justify these assumptions in Section 4.2.1.

3. Model verification of fractal treatment

When Brownian coagulation is the dominant mechanism for particle growth, particle size distributions assume an asymptotic shape after a sufficiently long time, independent of the initial size distribution (Friedlander and Wang 1966; Friedlander 2000). These so-called self-preserving size distributions are represented by graphing the dimensionless particle number density function $\psi(\eta)$ as a function of the dimensionless particle volume η (Equation (S-12)). The detailed formalism is provided in Section 2 in the SI.

In this study, the implementation of the fractal particle treatment in PartMC was verified by comparing the simulated self-preserving size distributions to those from theoretical results reported in Vemury and Pratsinis (1995) in both free molecular and continuum regimes. We followed the scenario set-up and model initialization of Vemury and Pratsinis (1995) as well as Naumann (2003).

Figures 1 and 2 show the verification of the size distributions and the total number concentrations, respectively, for different fractal dimensions. Perfect agreement is observed, confirming the successful implementation of the fractal particle treatment in PartMC. The error bars in Figure 1 show the 95% confidence intervals from 10 ensemble PartMC runs. They were too small to be visible in Figure 2. The decay of normalized number concentrations in Figure 2 is graphed vs. dimensionless times τ_f (free molecular regime) and τ_c (continuum regime). The dimensionless times τ_f and τ_c are defined in Equations (S-13) and (S-14), respectively.

4. Comparison with measurements for validation

4.1. Chamber measurements

Experiments were conducted in a 209 L, cylindrical, stainless steel chamber (Figure S-1) that was electrically grounded. The chamber was filled during the first 6 or 10 min (see below for details) of each experiment with dried, poly-disperse, charge-neutralized ammonium

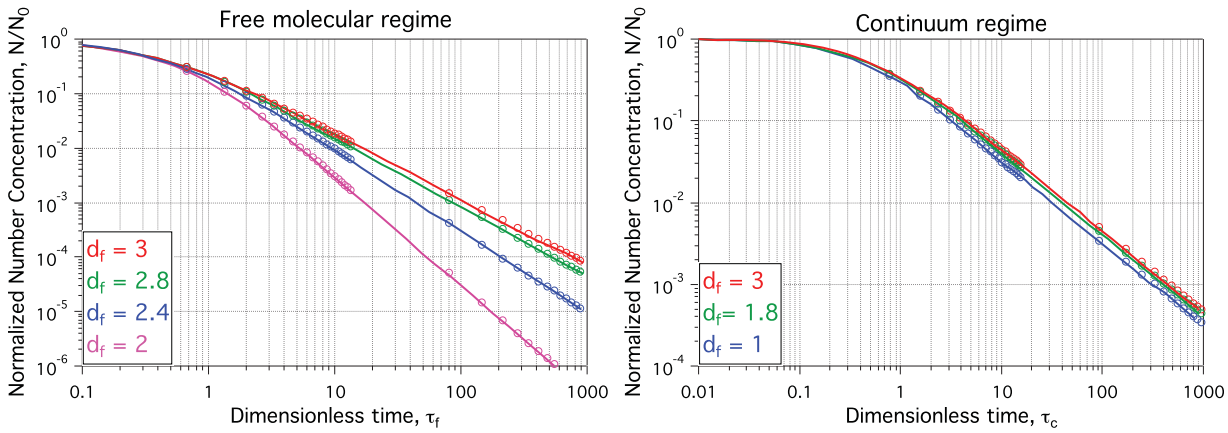

Figure 2. Normalized number concentration decay as a function of dimensionless time obtained from PartMC simulations (symbols) and the Vemury and Pratsinis (1995) code (lines) for various d_f values in free-molecular regime (left panel) and continuum regime (right panel). The dimensionless time is defined in Equation (S-13) for the free molecular regime and Equation (S-14) for the continuum regime.

sulfate aerosol that was generated by atomizing an aqueous 0.0001 g cm^{-3} ammonium sulfate solution with a constant output atomizer (Model 3076, TSI Inc., Shoreview, MN, USA; Figure S-1a). The aerosol generated was dried with a custom silica gel diffusion dryer and charge neutralized with a custom neutralizer (BMI Inc., Hayward, CA, USA) containing four 500 μC Polonium 210 sources (Staticmaster 2U500, Amstat Corp., Mundelein, IL, USA). The aerosol was then diluted with 26.5 L min^{-1} of dry, particle-free air (generated by passing through a high efficiency particle air [HEPA] filter), and particles with an aerodynamic diameter greater than 500 nm were removed with a greased two-stage Berner-type impactor (Berner et al. 1979) before entering the chamber. The pressure during filling was equilibrated by leaving the sampling port open into the laboratory fume hood.

After filling the chamber with atomized aerosol, the atomizer setup was disconnected from the chamber and the evolution of the size distribution was measured every 7 min with a modified scanning mobility particle sizer instrument (SMPS, TSI Instruments, 3934, Figure S-1b). This instrument consisted of a Polonium 210 neutralizer (Amstat Corp., Staticmaster 2U500), a differential mobility analyzer (DMA, TSI3071A), and a condensation particle counter (CPC, TSI 3022A) operating in low flow mode (0.3 L min^{-1}). A modification of the original instrument's configuration was the use of a HEPA-filtered recirculating sheath airflow that was set to 2.4 L min^{-1}. Air flow rates were checked and adjusted by comparing them to a primary standard airflow calibrator (Gilian Gilibrator, Sensidyne Corp., St. Petersburg, FL, USA) for each experiment. The voltage up-scan time was set to 300 s and the down-scan time was set to 60 s. These settings allowed a sizing range of particle diameters between 15.4 and 1000 nm. The delay time and sizing accuracy of the SMPS system was evaluated by performing up- and down-scans for 200 ± 5 nm and 350 ± 6 nm mono-disperse polystyrene latex (PSL) spheres (3200A/3350A, Thermo Scientific Corp., Waltham, MA, USA). The aerosol instrument manager software (TSI AIM Version 9.0, TSI Inc.) was used to collect and process the data from the SMPS system. The embedded multiple particle charge correction inversion algorithm from the TSI aerosol instrument manager software accounted for multiply charged particles. The pressure during sampling was equilibrated by having a bleed port at the chamber inlet. The measurements have estimated uncertainties of 1.5% for the flow rate (σ_{flow}), and of 5% for determining the particles size (σ_{size}). In addition, Poisson statistics were applied to approximate the raw count uncertainty (σ_{count}).

Three experiments were performed with Experiments 1 and 2 having a chamber filling time of 6 min and Experiment 3 having a filling time of 10 min. The initial size distributions for the simulations were taken to be the measured distributions after filling was completed. The code directly read in the particle number counts in the SMPS size bins. As a summary, the initial number concentrations, mean diameters, and standard deviations are listed in Table 1.

The evolution of the particle size distribution was tracked in each experiment for a minimum of 5 h. The

Table 1. Initial conditions for ammonium sulfate experiments from UIUC chamber measurements.

Exp. ID r	Initial conc. (cm^{-3})	Initial mean diam. (nm)	Initial standard dev. (nm)
1	$4.275 \cdot 10^5$	114	53.9
2	$3.548 \cdot 10^5$	93.2	53.8
3	$1.196 \cdot 10^6$	71.5	48.9

relative humidity and temperature monitored near the inlet and at the outlet of the chamber ranged from 3.2 to 9.1% and from 19.5 to 22.2°C, respectively, for all experiments. Temperature and relative humidity were measured with a Sensirion SHT-75 sensor (Sensirion Corp., Stäfa, Switzerland).

Filter samples were collected at the end of each experiment by drawing the barrel's remaining contents through 47 mm PTFE Membrane Filters (FGLP04700, Merck Millipore, Billerica, MA, USA). These samples were then used in scanning electron microscopy (SEM) imaging to obtain information about the microstructure of particles. The instrument was an FEI Company (Hillsboro, OR, USA) XL30 ESEM-FEG environmental scanning electron microscope, operated in HiVac mode. The imaging parameters were 5 kV and spot size 3 (2.1 nm) at a 10-mm working distance. The samples were received dry, mounted on aluminum stubs with double-stick carbon tabs (SPI Supplies, West Chester, PA, USA), sputter coated (Desk-2 turbo sputter coater, Denton Vacuum, Moorestown, NJ, USA) with ca. 6 nm of gold-palladium, and grounded using Flash-Dry (SPI Supplies) silver paint before imaging.

4.2. Determination of model parameters

Including wall loss and fractal dynamics introduces five unknown parameters in the governing equation, namely, two parameters in Equation (4) for the wall loss treatment (prefactor k_D and exponent a), and three in Equation (5) (fractal dimension d_f, radius of primary particles R_0, and volume filling factor f). As we will show in Section 4.2.1, we used SEM images to estimate the parameters f and R_0. We determined the remaining three parameters by a global optimization procedure as described in Section 4.2.2.

4.2.1. Determination of parameters f and R_0

Figure 3 shows the SEM images of the filters at the end of Experiment 1, after about 6 h of evolution. The particles show as bright agglomerates, some of which are highlighted with red circles in Figure 3. Note that the fibrous and smoother agglomerated material is the Teflon filter. The images reveal that over the course of the experiment, the dry ammonium sulfate particles formed agglomerates consisting of spherical primary particles.

SEM images were analyzed using image analysis software (ImageJ version 10.2, NIH) to estimate the values of the radius of primary particles R_0 and the volume filling factor f. The primary particles are not mono-disperse, but show a size distribution with a number-based median diameter of about 90 nm. Figure S-2 shows the histogram of the size distribution of 130 particles identified from the SEM images. Since in the current model implementation, the primary particle size is set to a constant value during the entire simulation time, we tested the sensitivity of the predicted size distribution to different R_0 values.

Figure S-3 shows the comparison of the number distribution at t = 280 min from Experiment 1 using three

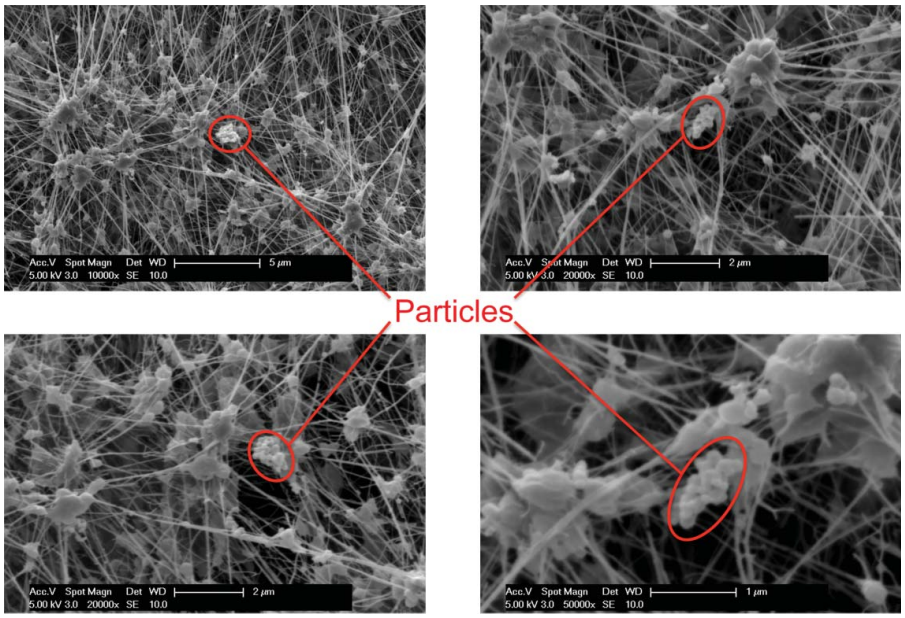

Figure 3. Scanning electron microscope (SEM) images of the particle filter from Experiment 1 at different resolutions. The fibrous and smoother agglomerated material is the Teflon filter.

R_0 values: 15 nm (the smallest), 45 nm (medium), and 80 nm (maximum). All other parameters are kept constant for the three simulations. The resulting size distributions have a maximum percentage difference (between the simulations with R_0 = 15 nm, and 80 nm) of 24% at a particle diameter of 100 nm, and 5% at 200 nm. Based on the uncertainty quantification as described below in Section 4.2.2, we can estimate the overall measurement uncertainty as 40% and 15% at 100 nm and 200 nm, respectively (see the light gray [orange band] in Figure 4). We therefore conclude that even extreme variations in R_0 values cause variations of the results that remain within the measurement uncertainties. This justifies setting R_0 to a fixed value, and we chose 45 nm, which is the median radius from the sample.

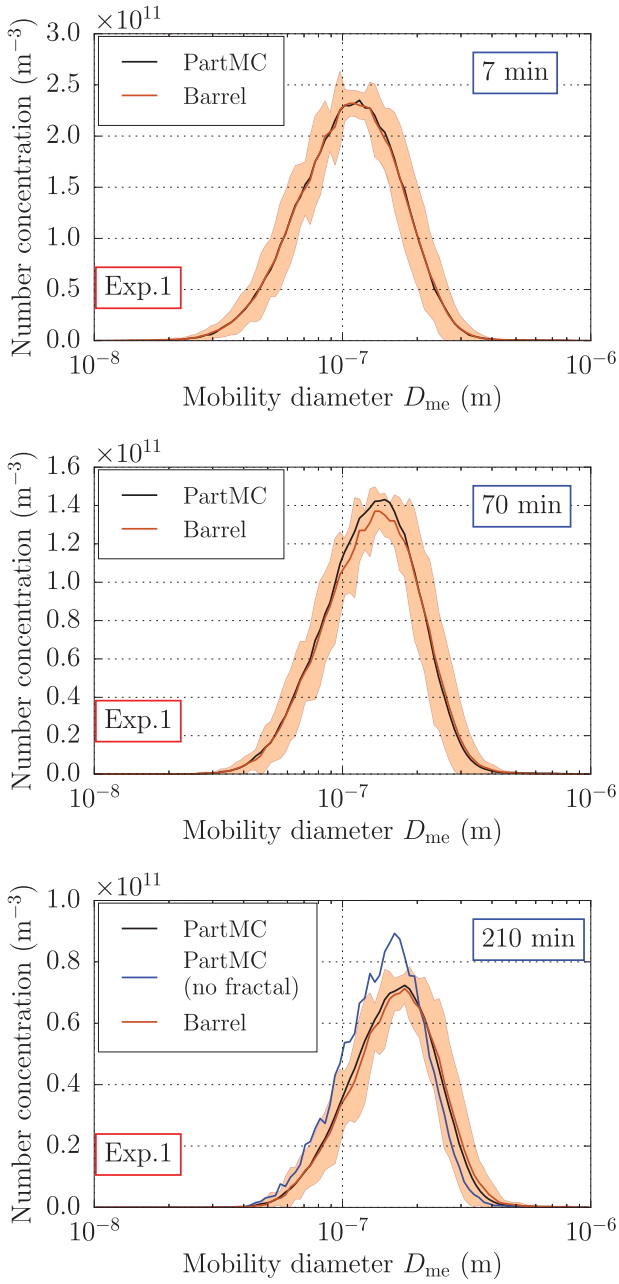

Figure 4. Simulated ("PartMC") and measured ("Barrel") particle size distributions from Experiment 1 at 7 min, 70 min, and 210 min (top to bottom). Shaded areas represent $\pm$ 3σ as described in Equation (7). The highest line (blue curve) in the bottom panel represents the simulated distribution assuming d_f = 3.

The volume filling factor f accounts for the fact that the spherical primary particles can occupy only as much as 74% of the available volume. Given the closely packed structure as shown in Figure 3, we assumed that 70% of the available volume would be occupied by the monomers (close to the extreme case), corresponding to an f value of 1.43. Similarly to the sensitivity test regarding R_0, we tested the sensitivity to the choice of parameter f. Figure S-4 shows the number distribution comparison from simulation results using f = 1.35, 1.43, and 2.0, corresponding to the monomers occupying 74%, 70%, and 50% of the available volume, respectively. The maximum percentage difference (between f = 1.35 and 2.0) is again small, being equal to 25% at a particle diameter of 100 nm and 14% at 200 nm. Therefore, a fixed f value of 1.43 was chosen for the model simulation.

4.2.2. Optimization procedure

With the determination of R_0 and f values in the previous section, the governing equation described in Section 2 now has three unknown parameters remaining: k_D and a in Equation (4) for the wall loss calculation, and d_f in Equation (5) for the fractal formalism. To find the appropriate values for these unknown parameters, inverse approaches using non-linear least-square fitting optimization on size distribution measurements have often been conducted (Pierce et al. 2008). We applied a similar approach in this study. To determine the combination of free parameters that gives the best agreement between simulation and measurements, we produced an ensemble of simulations for which we varied the parameters systematically between simulations. The best fit was determined when a chosen error metric was minimized across all simulations.

We jointly optimized k_D, a, and d_f by exhaustively searching over a pre-defined parameter domain. We considered all combinations of (k_D, a, d_f) with k_D varying from 0.025 m to 0.095 m with increments of 0.005 m, a varying from 0.22 to 0.27 with increments of 0.01, and d_f varying from 1.5 to 3.0 with increments of 0.1. These values are within the ranges reported in previous studies (Bunz and Dlugi 1991; Naumann 2003) and included the minimum in the interior of the domain. This amounts to a total of 14,400 simulations, generated by 15 × 6 × 16

cases, with each case repeated 10 times with different random seeds.

We define $E_{r,j}$ to be the weighted ℓ^2-norm of the difference in the discretized number size distributions of simulation and measurement at time j for experiment number r:

$$E_{r,j} = \sqrt{\sum_{i=1}^{N_{\text{bin}}} \frac{1}{(\sigma_{r,i,j})^2} \left(n_{\text{sim},r,i,j} - n_{\text{mea},r,i,j}\right)^2}, \qquad [6]$$

where $n_{\text{sim},r,i,j}$ and $n_{\text{mea},r,i,j}$ are the simulated and measured number concentration densities in size bin i at time j for experiment r, respectively, and N_{bin} is the number of size bins. The weighting factor $\sigma_{r,i,j}$ is the uncertainty that arises from both the measurement and the simulation. Similar to the approach in Moore et al. (2010), the total uncertainty at time j for the ith size bin and experiment r is

$$\sigma_{r,i,j} = \sqrt{\sigma_{\text{flow}}^2 + \sigma_{\text{size}}^2 + \left(\sigma_{\text{count},r,i,j}\right)^2 + \frac{1}{N_{\text{run}}} \left(\sigma_{\text{partmc},r,i,j}\right)^2}. \qquad [7]$$

The total error metric, ε_r, for experiment r is defined as the root mean square of the relative errors over the entire simulation period:

$$\varepsilon_r = \sqrt{\frac{1}{N+1} \sum_{j=0}^{N} \left(E_{r,j}\right)^2}, \qquad [8]$$

where N is the total number of time steps. The three experiments are combined by taking the root mean square error to give the total error ε by

$$\varepsilon = \sqrt{(\varepsilon_1)^2 + (\varepsilon_2)^2 + (\varepsilon_3)^2}. \qquad [9]$$

The best-fit values for k_{D}, a, d_{f} are found by determining the minimum value of ε:

$$(k_{\text{D}}, a, d_{\text{f}}) = \text{argmin}_{k_{\text{D}}', a', d_{\text{f}}'}\, \varepsilon\left(k_{\text{D}}', a', d_{\text{f}}'\right). \qquad [10]$$

Care has to be taken regarding the physical interpretation of the d_{f} value obtained, since our aggregates only contain a small number of monomers. The implications of this fact are discussed in the next section.

4.3. Results

With datasets from three experiments available, we performed the optimization procedure on the data from all experiments combined. We obtained $k_{\text{D}} = 6.0$ cm, $a = 0.26$, and $d_{\text{f}} = 2.3$ as best fit estimates with the errors $\varepsilon_1 = 8.09$, $\varepsilon_2 = 9.62$, and $\varepsilon_3 = 14.91$ for Experiments 1, 2, and 3, respectively.

The coefficient k_{D} is proportional to the laminar boundary layer and can vary between different experimental setups (Bunz and Dlugi 1991). Our best estimate for k_{D} (6.0 cm) is very similar to the results by van de Vate and ten Brink (1980) who determined $k_{\text{D}} = 4.8$ cm as their best fit. Bunz and Dlugi (1991), in contrast, found best agreement by reducing k_{D} to 0.5 cm. For the parameter a, Bunz and Dlugi (1991) reported a value of 0.25 from previous theoretical derivations by Fuchs (1964) and 0.274 from their experiments. Our optimal values for a is 0.26, close to these previously reported values. Our optimal fractal dimension of 2.3 is clearly below the value of 3 for spherical particles, but it is significantly higher than the value of 1.78 ± 0.1 predicted by diffusion-limited cluster-cluster aggregation (DLCA) theory (Sorensen 2011).

In our case, the reason that d_{f} is higher than the theoretically expected value can be explained by the fact that the aggregates only contain a small number of monomers ($N < 100$). As described in Sorensen (2011), in this case the scaling of the mobility diameter R_{me} can be written as

$$R_{me} = \beta R_{\text{g}} \propto \beta N^{1/\hat{d}_{\text{f}}} \propto N^{-0.13} N^{1/\hat{d}_{\text{f}}}, \qquad [11]$$

where $\hat{d}_{\text{f}}$ is the true fractal dimension. As detailed in the SI, Equation (S-3), we are using the Naumann (2003) relationship

$$R_{\text{me}} = h_{\text{KR}} R_{\text{geo}} = h_{\text{KR}} R_0 (fN)^{1/d_{\text{f}}} \propto N^{1/d_{\text{f}}}. \qquad [12]$$

Importantly, h_{KR} does not depend on N, and so we see that in the small-N case the parameter d_{f} in the Naumann (2003) model that we use is in fact the mass-mobility scaling exponent D_{m} described by Sorensen (2011), which is defined by the relationship $R_{\text{me}} \propto N^{1/D_{\text{m}}}$.

Equating Equations (11) and (12) gives a relationship between the fitted parameter d_{f} and the true fractal dimension $\hat{d}_{\text{f}}$:

$$N^{-0.13} N^{1/\hat{d}_{\text{f}}} \propto R_{\text{me}} \propto N^{1/d_{\text{f}}}. \qquad [13]$$

From our optimization procedure, we obtain the value $d_{\text{f}} = 2.3$, so equating the exponents of N in (13) allows us to compute that the true fractal dimension implied by our model is $\hat{d}_{\text{f}} = 1.78$. This matches the theoretically expected value of 1.78 ± 0.1 for DLCA processes (Sorensen 2011).

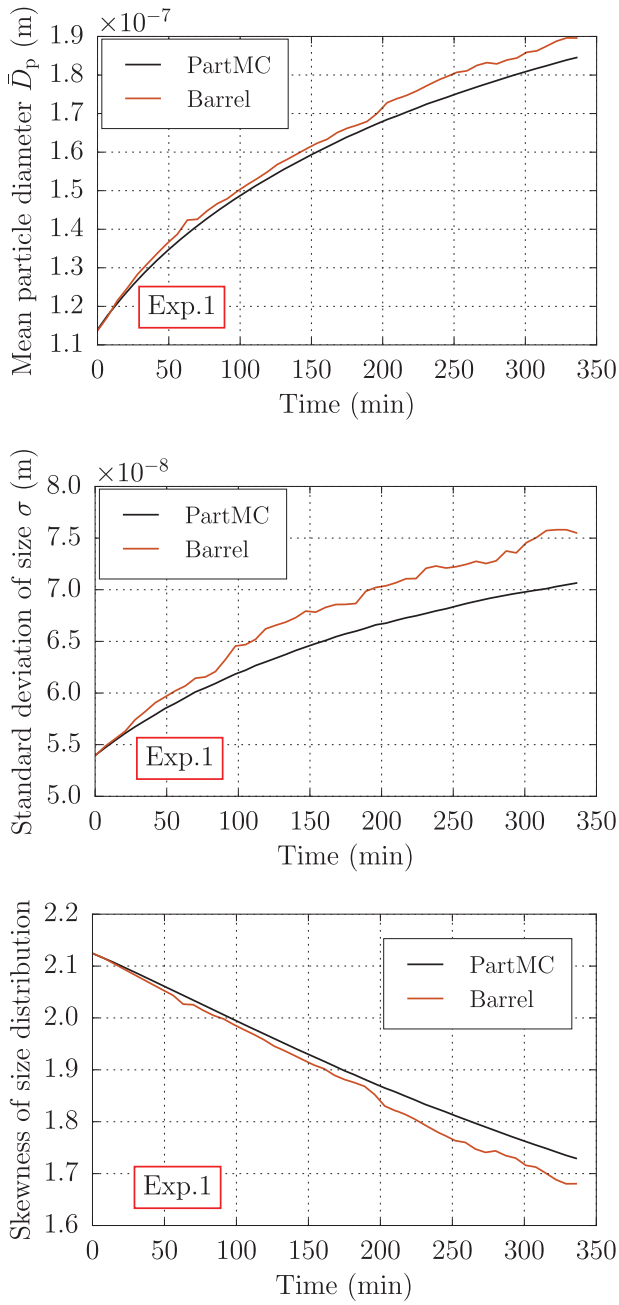

Figure 5. Time evolution of simulated ("PartMC") and experimentally determined ("Barrel") mean diameter, standard deviation of size distribution, and skewness of size distributions (top to bottom) for Experiment 1.

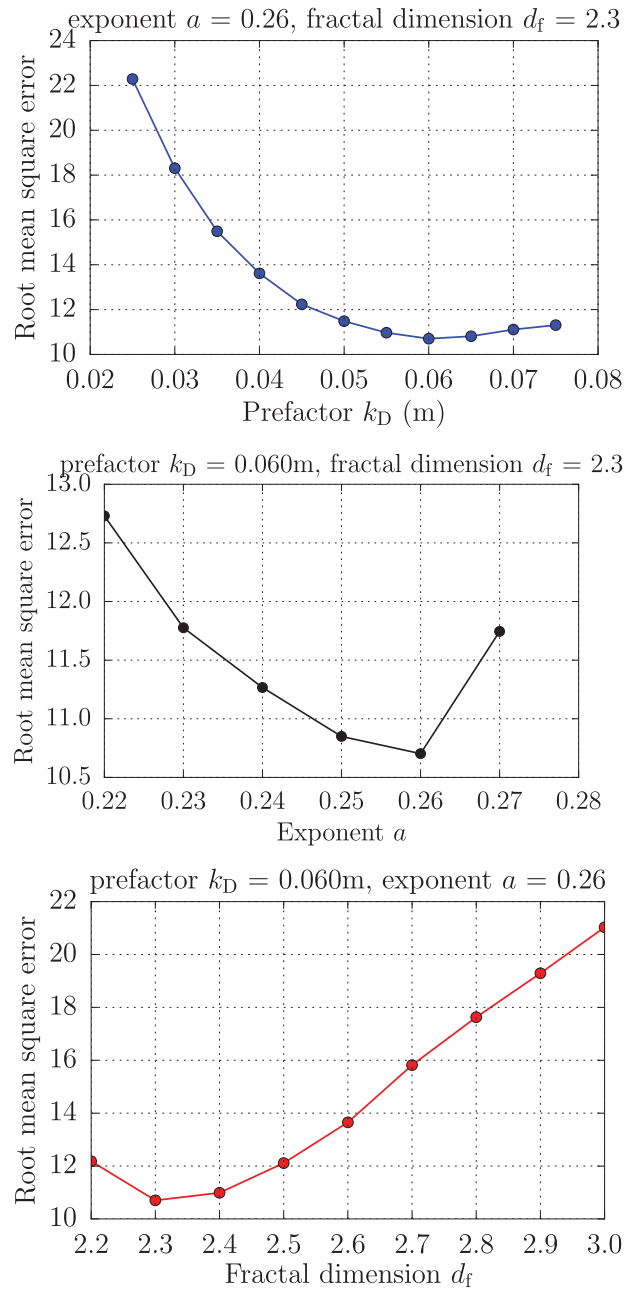

Figure 6. Sensitivity of free parameters k_D, a, and d_f on model-measurement comparison results described by the value of root mean square error ε for the combined optimization procedure. When a parameter was varied, the other two parameters were fixed at their optimal value.

Figure 4 shows the evolution of measured and simulated number size distributions at 7 min, 70 min, and 210 min for Experiment 1 using the best-estimate parameters for this experiment. The number size distributions in Figure 4 and similar figures are shown as a function of mobility diameter. The shaded areas indicate the estimated uncertainty based on Equation (7) with the width of 3σ, i.e., we expect 99% of the values to be within the bounds of the shaded range. Note that the maximum values on the vertical axes change between the three panels to ensure readability. For the entire simulation time of about 3.5 h, the simulated distributions match the experimental results within the uncertainties. This is further shown by displaying the time evolution of several key parameters of measured and simulated size distributions, including mean diameter, standard deviation, and skewness, as shown in Figure 5. For comparison, we also simulated the size distribution when spherical particles are assumed throughout the entire simulation (blue trace

in the right-most panel of Figure 4). This simulation result does not capture the measured distribution, confirming the need to include the treatment for fractal particles.

Figures S-5 and S-6 in the SI show the results for all three experiments. Except for one occasion (Experiment 3, after 7 min) all model results are within the range of the uncertainties. Overall, the good agreement between PartMC simulations and chamber measurement indicates that the model is able to capture the evolution of particles in a chamber environment undergoing Brownian coagulation and wall losses.

We further quantified the relative importance of particle loss due to coagulation and wall loss with two additional sensitivity runs for which coagulation and wall loss were disabled, respectively (Figure S-7). For Experiment 1, after around 5 h, wall loss and coagulation accounted for an additional 5% and 20% of particle loss, respectively, hence both processes are important in shaping the aerosol size distribution, but coagulation dominates.

A potential concern with an optimization procedure as used in this work is that different combinations of free parameters may result in errors of similar magnitude. To investigate this, we show in Figure 6 the dependence of ε on each of the three parameters individually, while keeping the other two constant and equal to their optimal values. These curves should exhibit a clear minimum within the range of parameters used, which then indicates the optimal parameter combination. From this figure we also learn that the fractal dimension d_f is always the dominant factor determining ε, compared to k_D and a. This is in agreement with our finding that coagulation is relatively more important than wall loss (Figure S-7) and in line with the results by Naumann (2003).

Lastly, we checked to what extent the parameters k_D, a, and d_f and the error ε change when the optimization procedure is performed on each experiment individually. As expected, the error decreases when the optimization is performed individually, namely, by 15%, 24%, and 4.5% for Experiments 1, 2, and 3, respectively. While the optimal parameter values are not identical for the three experiments, they remain in a relatively small range, with k_D between 0.040 m and 0.070 m, a between 0.22 and 0.26, and d_f between 2.2 and 2.4 (Table 2). This finding is consistent with our initial approach of performing the optimization procedure on the data from all experiments combined.

Table 2. Comparison of the optimal parameters obtained by optimizing over all three experiments combined and optimizing over each experiment individually.

Optimization	k_D (m)	a	d_f
combined	0.060	0.26	2.3
Indiv. Exp. 1	0.060	0.26	2.2
Indiv. Exp. 2	0.070	0.22	2.3
Indiv. Exp. 3	0.040	0.25	2.4

5. Conclusions

We conducted verification and validation of the stochastic particle-resolved aerosol model PartMC. Verification was performed against self-preserving analytical solutions, while for validation we performed three experiments with coagulating ammonium sulfate particles in a cylindrical stainless steel chamber under a range of input conditions and measured the evolving aerosol size distributions.

To compare with the chamber measurements, we extended PartMC to include the representation of fractal particle structure and wall loss. Including wall loss and fractal dynamics in the governing equation introduced five unknown parameters. We constrained two of them (radius of the primary particles R_0 and volume filling factor f) using SEM images and determined the remaining three parameters (wall loss parameters k_D and a, and fractal dimension d_f) by a global optimization procedure to fit the experimental data.

We showed that excellent agreement between modeled and measured size distributions can be achieved using the same set of parameters for all three experimental conditions, and we checked that estimating the parameters for each experiment individually did not substantially improve the fit. This creates the foundation for a model framework that can be applied to more complex experiments, for example, to investigate the evolution of aerosol mixing state when secondary aerosol material is coating the particles.

While the aim of this study was to verify and validate PartMC, we reach the following broader conclusions. The fact that our fitted value of $a = 0.26$ is close to the theoretically derived value of 0.25 is an excellent indication that our approach is valid. It would be interesting to determine the value of k_D for other chambers of similar design (i.e., stainless steel chambers) or of different type (e.g., teflon chambers). Further, it is likely that for aerosols generated as it was done in this study, a fractal dimension smaller than 3 is appropriate. These hypotheses should be tested on additional chamber datasets.

Currently, the model uses a constant value of fractal dimension throughout the simulation period. From the comparison of the model results to the experimental data, we conclude that using a constant d_f value is a good approximation for simulating coagulating particle

populations in these experiments. At the same time, the strong sensitivity of the results to the fractal dimension value may justify the implementation of a more sophisticated model treatment, which, for example, would allow the simulation of particle restructuring during more complex mixing and coating processes. This could be easily achieved by adding fractal dimension as an additional per-particle entry in the particle-resolved representation using the PartMC model. At the same time, this would necessitate more detailed particle size measurements to constrain the rate of change of d_f during the evolution of particles in the chamber.

Acknowledgments

The authors thank Cate Wallace, Beckman Institute for Advanced Science and Technology, University of Illinois at Urbana-Champaign, for performing the SEM imaging. The authors thank the editor, Dr. Yannis Drossinos, for insightful comments that greatly improved the manuscript.

Funding

J. T., B. T. B., T. C. B, M. J. R., and N. R. acknowledge DOE-ASR funding from grant DE-SC0006689. N. R. and M. W. acknowledge support from DOE-ASR DE-SC0011771, and M. W. acknowledges support from NSF CMMI 11-50490.

References

Artelt, C., Schmid, H.-J., and Peukert, W. (2003). On the Relevance of Accounting for the Evolution of the Fractal Dimension in Aerosol Process Simulations. *J. Aerosol Sci.*, 34(5):511–534.

ASME., (2006). *Guide for Verification and Validation in Computational Solid Mechanics (ASME V&V 10-2006)*. American Society of Mechanical Engineers, New York. Reaffirmed 2016.

Berner, A., Lürzer, C., Pohl, F., Preining, O., and Wagner, P. (1979). The Size Distribution of the Urban Aerosol in Vienna. *Sci. Total. Environ.*, 13(3):245–261.

Bunz, H., and Dlugi, R. (1991). Numerical Studies on the Behavior of Aerosols in Smog Chambers. *J. Aerosol Sci.*, 22 (4):441–465.

Chen, H., Iskander, M., and Penner, J. (1990). Light Scattering and Absorption by Fractal Agglomerates and Coagulations of Smoke Aerosols. *J. Mod. Optic.*, 37(2):171–181. DOI:10.1080/09500349014550251.

Ching, J., Riemer, N., and West, M. (2012). Impacts of Black Carbon Mixing State on Black Carbon Nucleation Scavenging: Insights from a Particle-Resolved Model. *J. Geophys. Res.-Atmos.*, 117(D23). DOI:10.1029/2012JD018269.

Ching, J., Riemer, N., and West, M. (2016). Black Carbon Mixing State Impacts on Cloud Microphysical Properties: Effects of Aerosol Plume and Environmental Conditions. *J. Geophys. Res.*, 121:5990–6013.

Crump, J., and Seinfeld, J. (1981). Turbulent Deposition and Gravitational Sedimentation of an Aerosol in a Vessel of Arbitrary Shape. *J. Aerosol Sci.*, 12(5):405–415.

DeVille, R., Riemer, N., and West, M. (2011). Weighted Flow Algorithms (WFA) for Stochastic Particle Coagulation. *J. Geophys. Res.*, 230(23):8427–8451. DOI:10.1016/j.jcp.2011.07.027.

Eggersdorfer, M. L., and Pratsinis, S. E. (2014). Agglomerates and Aggregates of Nanoparticles Made in the Gas Phase. *Adv. Powder Technol.*, 25(1):71–90. DOI:10.1016/j.apt.2013.10.010.

Eibeck, A., and Wagner, W. (2001). Stochastic Particle Approximations for Smoluchoski's Coagulation Equation. *Ann. Appl. Probab.*, 11(4):1137–1165.

Fierce, L., Riemer, N., and Bond, T. C. (2015). Explaining Variance in Black Carbon's Aging Timescale. *Atmos. Chem. Phys.*, 15:3173–3191. DOI:10.5194/acp-15-3173-2015.

Friedlander, S., and Wang, C. (1966). Self-Preserving Particle Size Distribution for Coagulation by Brownian Motion. *J. Colloid Interface Sci.*, 22(2):126–132. DOI:10.1016/0021-9797(66)90073-7.

Friedlander, S. K. (2000). *Smoke, Dust and Haze: Fundamentals of Aerosol Dynamics*. Oxford University Press, New York; Oxford.

Fuchs, N. A. (1964). *Mechanics of Aerosols*. Pergamon, New York.

Gillespie, D. T. (1975). An Exact Method for Numerically Simulating Stochastic Coalescence Process in a Cloud. *J. Atmos. Sci.*, 32(10):1977–1989.

Gillespie, D. T., Roh, M., and Petzold, L. R. (2009). Refining the Weighted Stochastic Simulation Algorithm. *J. Chem. Phys.*, 130(17):174103. DOI:10.1063/1.3116791.

Jokulsdottir, T., and Archer, D. (2016). A Stochastic, Lagrangian Model of Sinking Biogenic Aggregates in the Ocean (SLAMS 1.0): Model Formulation, Validation and Sensitivity. *Geosci. Model Dev.*, 9(4):1455–1476.

Kaiser, J. C., Riemer, N., and Knopf, D. A. (2011). Detailed Heterogeneous Oxidation of Soot Surfaces in a Particle-Resolved Aerosol Model. *Atmos. Chem. Phys.*, 11(9):4505–4520. DOI:10.5194/acp-11-4505-2011.

Koch, W., and Friedlander, S. (1990). The Effect of Particle Coalescence on the Surface Area of a Coagulating Aerosol. *J. Colloid Interf. Sci.*, 140(2):419–427. DOI:10.1016/0021-9797(90)90362-R.

Kolb, C. E., and Worsnop, D. R. (2012). Chemistry and Composition of Atmospheric Aerosol Particles. *Annu. Rev. Phys. Chem.*, 63(1):471–491. DOI:10.1146/annurev-physchem-032511-143706.

Kostoglou, M., and Konstandopoulos, A. G. (2001). Evolution of Aggregate Size and Fractal Dimension During Brownian Coagulation. *J. Aerosol Sci.*, 32(12):1399–1420.

Lapuerta, M., Ballesteros, R., and Martos, F. J. (2006). A Method to Determine the Fractal Dimension of Diesel Soot Agglomerates. *J. Colloid Interf. Sci.*, 303(1):149–158.

Liffman, K. (1992). A Direct Simulation Monte-Carlo Method for Cluster Coagulation. *J. Comput. Phys.*, 100:116–127.

Matsunaga, A., and Ziemann, P. J. (2010). Gas-Wall Partitioning of Organic Compounds in a Teflon Film Chamber and Potential Effects on Reaction Product and Aerosol Yield Measurements. *Aerosol Sci. Technol.*, 44(10):881–892.

McMurry, P., and Rader, D. (1985). Aerosol Wall Losses in Electrically Charged Chambers. *Aerosol Sci. Technol.*, 4 (3):249–268.

Moldanová, J., Fridell, E., Popovicheva, O., Demirdjian, B., Tishkova, V., Faccinetto, A., and Focsa, C. (2009). Characterisation of Particulate Matter and Gaseous Emissions From a Large Ship Diesel Engine. *Atmos. Environ.*, 43:2632–2641.

Moore, R. H., Nenes, A., and Medina, J. (2010). Scanning Mobility CCN Analysis - A Method for Fast Measurements of Size-Resolved CCN Distributions and Activation Kinetics. *Aerosol Sci. Technol.*, 44(10):861–871. DOI:10.1080/02786826.2010.498715.

Naumann, K. (2003). COSIMA—A Computer Program Simulating the Dynamics of Fractal Aerosols. *J. Aerosol Sci.*, 34 (10):1371–1397.

Okuyama, K., Kousaka, Y., Yamamoto, S., and Hosokawa, T. (1986). Particle Loss of Aerosols With Particle Diameters Between 6 and 2000 nm in Stirred Tank. *J. Colloid Interf. Sci.*, 110(1):214–223.

Okuzumi, S., Tanaka, H., and Sakagami, M. (2009). Numerical Modeling of the Coagulation and Porosity Evolution of Dust Aggregates. *The Astrophys. J.*, 707(2):1247–1263.

Ormel, C. W., and Spaans, M. (2008). Monte Carlo Simulation of Particle Interactions at High Dynamic Range: Advancing Beyond the Googol. *Astrophys. J.*, 684(2):1291–1309. DOI:10.1086/590052.

Park, S., Kim, H., Han, Y., Kwon, S., and Lee, K. (2001). Wall Loss Rate of Polydispersed Aerosols. *Aerosol Sci. Technol.*, 35(3):710–717.

Pierce, J. R., Engelhart, G. J., Hildebrandt, L., Weitkamp, E. A., Pathak, R. K., Donahue, N. M., Robinson, A. L., Adams, P. J., and Pandis, S. N. (2008). Constraining Particle Evolution From Wall Losses, Coagulation, and Condensation-Evaporation in Smog-Chamber Experiments: Optimal Estimation Based on Size Distribution Measurements. *Aerosol Sci. Technol.*, 42(12):1001–1015.

Pöschl, U. (2005). Atmospheric Aerosols: Composition, Transformation, Climate and Health Effects. *Angew. Chem. Int. Ed.*, 44(46):7520–7540. DOI:10.1002/anie.200501122.

Pranami, G., Lamm, M. H., and Vigil, R. D. (2010). Molecular Dynamics Simulation of Fractal Aggregate Diffusion. *Phys. Rev. E*, 82, 051402.

Riemer, N., West, M., Zaveri, R., and Easter, R. (2010). Estimating Black Carbon Aging Time-Scales with a Particle-Resolved Aerosol Model. *J. Aerosol Sci.*, 41(1, SI):143–158. DOI:10.1016/j.jaerosci.2009.08.009.

Riemer, N., West, M., Zaveri, R. A., and Easter, R. C. (2009). Simulating the Evolution of Soot Mixing State with a Particle-Resolved Aerosol Model. *J. Geophy. Res.*, 114:D09202. DOI:10.1029/2008JD011073.

Roh, M. K., Daigle, B. J., Gillespie, D. T., and Petzold, L. R. (2011). State-Dependent Doubly Weighted Stochastic Simulation Algorithm for Automatic Characterization of Stochastic Biochemical Rare Events. *J. Chem. Phys.*, 135 (23):234108. DOI:10.1063/1.3668100.

Seinfeld, J. H., and Pandis, S. N. (2006). *Atmospheric Chemistry and Physics: From Air Pollution to Climate Change*. J. Wiley, New York.

Shekar, S., Sander, M., Riehl, R. C., Smith, A. J., Braumann, A., and Kraft, M. (2012). Modelling the Flame Synthesis of Silica Nanoparticles from Tetraethoxysilane. *Chem. Eng. Sci.*, 70(0):54–66. DOI:10.1016/j.ces.2011.06.010.

Shima, S., Kusano, K., Kawano, A., Sugiyama, T., and Kawahara, S. (2009). The Super-Droplet Method for the Numerical Simulation of Clouds and Precipitation: A Particle-Based and Probabilistic Microphysics Model Coupled With a Non-Hydrostatic Model. *Q. J. R. Meteorol. Soc.*, 135(642, A):1307–1320.

Sorensen, C. (2001). Light Scattering by Fractal Aggregates: A Review. *Aerosol Sci. Technol.*, 35(2):648–687.

Sorensen, C. M. (2011). The Mobility of Fractal Aggregates: A Review. *Aerosol Sci. Technol.*, 45:765–779.

Tian, J., Riemer, N., West, M., Pfaffenberger, L., Schlager, H., and Petzold, A. (2014). Modeling the Evolution of Aerosol Particles in a Ship Plume Using PartMC-MOSAIC. *Atmos. Chem. Phys.*, 14(11):5327–5347. DOI:10.5194/acp-14-5327-2014.

Ulrich, G. D., and Subramanian, N. S. (1977). III. Coalescence as a Rate-Controlling Process. *Combust. Sci. Technol.*, 17 (3–4):119–126. DOI:10.1080/00102207708946822.

van de Vate, J. F., and ten Brink, H. M. (1980). The Boundary Layer for Diffusive Aerosol Deposition Onto Walls, in *Proceedings of the CSNI Specialists Meeting on Nuclear Aerosols in Reactor Safety*. Gaitlinburg, U.S.A., pp. 162–170.

Vemury, S., and Pratsinis, S. (1995). Self-Preserving Size Distributions of Agglomerates. *J. Aerosol Sci.*, 26(2):175–185. DOI:10.1016/0021-8502(94)00103-6.

Verheggen, B., and Mozurkewich, M. (2006). An Inverse Modeling Procedure to Determine Particle Growth and Nucleation Rates From Measured Aerosol Size Distributions. *Atmos. Chem. Phys.*, 6:2927–2942.

Wells, C., Morgan, N., Kraft, M., and Wagner, W. (2006). A New Method for Calculating the Diameters of Partially-Sintered Nanoparticles and Its Effect on Simulated Particle Properties. *Chem. Eng. Sci.*, 61(1):158–166. DOI:10.1016/j.ces.2005.01.048.

Wentzel, M., Gorzawski, H., Naumann, K., Saathoff, H., and Weinbruch, S. (2003). Transmission Electron Microscopical and Aerosol Dynamical Characterization of Soot Aerosols. *J. Aerosol Sci.*, 34(10):1347–1370.

Wu, M., and Friedlander, S. (1993). Enhanced Power Law Agglomerate Growth in the Free Molecule Regime. *J. Aerosol Sci.*, 24(3):273–282. DOI:10.1016/0021-8502(93)90002-Q.

Zaveri, R. A., Barnard, J. C., Easter, R. C., Riemer, N., and West, M. (2010). Particle-Resolved Simulation of Aerosol Size, Composition, Mixing State, and the Associated Optical and Cloud Condensation Nuclei Activation Properties in an Evolving Urban Plume. *J. Geophys. Res.*, 115:D17210. DOI:10.1029/2009JD013616.

Zaveri, R. A., Easter, R. C., Fast, J. D., and Peters, L. K. (2008). Model for Simulating Aerosol Interactions and Chemistry (MOSAIC). *J. Geophys. Res.*, 113(D13). DOI:10.1029/2007JD008782.

Appendix E

A plume-exit approach to determine cloud condensation nuclei activity of aerosols from residential biofuel combustion

Francisco Mena, Tami C. Bond, Nicole Riemer

Submitted to Atmospheric Chemistry and Physics (in revision)

ABSTRACT. Residential biofuel combustion is an important source of aerosols and gases in the atmosphere. The change in cloud characteristics due to biofuel burning aerosols is uncertain, in part, due to the uncertainty in the added number of cloud condensation nuclei (CCN) from biofuel burning. We provide estimates of the CCN activity of biofuel burning aerosols by explicitly modeling plume dynamics (coagulation, condensation, chemical reactions, and dilution) in a young biofuel burning plume from emission until plume-exit, defined here as the condition when the plume reaches ambient temperature and specific humidity through entrainment. We found that aerosol-scale dynamics affect CCN activity only during the first few seconds of evolution, after which the CCN efficiency reaches a constant value. Homogenizing factors in a plume are co-emission of SVOCs or emission at small particle sizes; SVOC co-emission can be the main factor determining plume-exit CCN for hydrophobic or small particles. Coagulation limits emission of CCN to about 10^{16} per kg of fuel. Depending on emission factor, particle size, and composition, some of these particles may not activate at low s_{sat}. Hygroscopic Aitken mode particles can contribute to CCN through self-coagulation, but have a small effect on the CCN activity of accumulation-mode particles, regardless of composition differences. Simple models (monodisperse coagulation and average hygroscopicity) can be used to estimate plume-exit CCN within about 20% if particles are unimodal and have homogeneous composition, or when particles are emitted in the Aitken mode even if they are not homogeneous. On the other hand, if externally-mixed particles are emitted in the accumulation mode without SVOCs, an average hygroscopicity overestimates emitted CCN by up to a factor of 2. This work has identified conditions under which particle populations become more homogeneous during plume processes. This homogenizing effect requires the components to be truly co-emitted, rather than sequentially emitted.

1. Introduction

Residential combustion of biofuels (including wood, dung, agricultural residues, and charcoal) is an important source of trace gases that play a role in atmospheric chemistry (Chuen-Yu et al., 2011; Williams et al., 2012). Ludwig et al. (2003) estimated that domestic biofuel combustion contributes 7-20% of the global budget of CO_2, CO, and NO. Akagi et al. (2011) estimated that biofuel burning emits 150 Tg/yr of non-methane organic compounds.

Biofuel combustion is also an important source of particles, contributing 20% of primary organic carbon (OC) and black carbon (BC) globally (Bond et al., 2004). These particles affect radiative transfer through interactions with sunlight and clouds. Scattering and absorption of solar radiation by aerosol particles is known as the "direct effect" of aerosols on climate, while the "indirect effect" refers to changes in radiation as aerosol particles alter cloud characteristics. The indirect effect can counteract the warming due to greenhouse gases and absorbing aerosols by increasing the cloud albedo.

Improving model estimates of Earth's radiative response to changes in human activities requires a better understanding of how aerosols with different compositions and mixing states can act as CCN and, hence, influence cloud properties. The overall climate impact of biofuel combustion aerosols is still uncertain because, although biofuel emissions contain BC, an important warming agent (Jacobson, 2000), the magnitude of the indirect effect of biofuel

combustion aerosols is still unknown. Jacobson (2010) found that eliminating biofuel soot and gases in addition to fossil fuel soot emissions resulted in a cooling effect and reduced surface air temperatures by 0.4 – 0.7 K, whereas eliminating fossil fuel soot emissions alone decreased air temperatures by only 0.3 – 0.5 K. In contrast, Bauer et al. (2010) found that reducing biofuel emissions of black and organic carbon aerosols by 50% decreased the number concentration of cloud condensation nuclei (CCN), leading to an increase in radiative forcing of 0.13 W/m^2, and therefore led to an overall warming effect. Koch et al. (2011) summarized multiple model results showing that eliminating biofuel burning soot would reduce CCN concentrations and lead to a warming effect. The reason for the discrepancy in these studies lies, in part, in estimating the indirect effect. Both Bauer et al. (2010) and Koch et al. (2011) highlighted the sensitivity of their results to assumptions about aerosol properties such as size distribution and mixing state, that is, how chemical species are distributed across the particle population. Mann et al. (2014) compared models with observations under the AeroCom initiative and reported that some differences might be attributable to missing particle growth or assumptions in size distribution of emissions. Seinfeld et al. (2016) identified the necessity of assessing the level of detail in aerosol microphysical and chemical properties required to represent aerosol-cloud interactions.

In this work, we examine combustion of biofuel to provide energy rather than open biomass burning. The latter refers to large open fires of natural origin or for deforestation and agricultural clearing. Although both activities combust cellulosic fuels, residential biofuel burning plumes dilute to ambient conditions within seconds to minutes. In contrast, biomass burning plumes from an individual event result from uncontrolled combustion of a large area of fuel, and can extend for several kilometers (Trentmann et al., 2006). Open biomass burning contributes 74% of primary OC and 42% of BC to the global budget (Bond et al., 2004). Biofuel burning contributes a smaller fraction (20% of primary OC and BC globally) but represents still a large fraction of global emissions that dominates some regions.

In global models of atmospheric chemistry, emissions are instantaneously diluted into the large grid boxes in which the emissions occur. Therefore, plume-scale processes of coagulation, condensation and evaporation, chemical reactions, entrainment of dry air, and dilution, are neglected (Poppe et al., 1998; Gao et al., 2003; Jost et al., 2003), although they may affect the properties of aerosols in the plume (Trentmann et al., 2005). In young plumes, defined here as conditions where within-plume concentrations and temperatures are greatly elevated above background, high gas and particle concentrations intensify these processes. Within the first hour, it is common to observe increases in inorganic aerosol mass by factors of 2-10 (Gao et al., 2003; Hobbs et al., 2003), and increases in organic aerosol mass by factors of 1.6-4 (Alvarado and Prinn, 2009; Vakkari et al., 2014). Chemical and physical processes that occur during the early evolution of the plume affect aerosol composition, size, and hygroscopicity, and, thereby, the aerosols' ability to become cloud droplets, known as activation. Research on activation properties within young plumes has examined large-scale biomass burning plumes (*e.g.*, Mason et al. 2001; Trentmann et al. 2002, 2005, 2006; Gao et al. 2003; Jost et al. 2003; Alvarado et al., 2009). To our knowledge, no study has investigated the plume dynamics that affect aerosol evolution within small-scale, young biofuel burning plumes.

The objective of this study is to address this research gap for the specific case of residential biofuel combustion. We model the evolution of particles within biofuel burning plumes from emission until plume exit, defined here as the condition when the plume reaches ambient temperature and specific humidity. These simulations are performed for a range of

combustion and plume scenarios to estimate likely plume-exit properties and to understand the level of detail required for estimating CCN concentrations.

2. Methodology

A young plume is a rapidly changing environment. After emission, the plume rises due to thermal convection, and entrainment of background air lowers the plume temperature as well as the gas and particle concentration. The decrease in temperature increases relative humidity (RH), but the entrainment of background air counteracts this by decreasing the water content (Trentmann et al., 2006; Shrivastava et al., 2006). The following sections explain how we modeled each of these processes.

2.1. Modeling aerosol evolution and CCN activation: PartMC-MOSAIC

We modeled the aerosol dynamics within the plume with the Particle Monte Carlo (PartMC) model (Riemer et al., 2009) coupled to the Model for Simulating Aerosol Interactions and Chemistry (MOSAIC) (Zaveri et al., 2008). PartMC-MOSAIC is a box model that tracks the composition of individual particles within a Lagrangian air parcel as they evolve due to Brownian coagulation, condensation and evaporation (*i.e.* gas-particle partitioning), chemical reactions, and dilution. Whereas coagulation and dilution are modeled as stochastic processes with a Poisson distribution, MOSAIC simulates the gas and particle-phase thermodynamics, and gas-particle mass transfer (Riemer et al., 2009; Zaveri et al., 2008). MOSAIC uses the SORGAM scheme to model the formation of low- and semi-volatility products from the oxidation of precursors, and their gas-particle partitioning (Schell et al., 2001; Zaveri et al., 2010). PartMC-MOSAIC simulates the mixing ratio of 77 gases and the mass concentration of 20 aerosol species in the plume. For each simulation we used a time-step of 0.005 s and 10^5 computational particles, each one representing a number of simulated particles in the plume.

The high concentrations of gases and particles in a biofuel burning plume, as well as rapid temperature changes, lead to rapid condensation of semi-volatile species and aerosol coagulation. Since PartMC-MOSAIC is a particle-based method, which fully resolves the composition of a representative sample of individual particles in the plume, it is suited to study the evolution of complex biofuel burning aerosol distributions, and to investigate changes that may not be captured by moment-based (Whitby et al., 1997, McGraw et al., 1997) or sectional (Jacobson, 1997) schemes. While the latter two schemes have a long tradition in aerosol modeling studies, they approximate particle size and composition, and hence, their predictions are limited by the accuracy of the approximation. For scenarios where mixing state does not have an effect on particle properties, these approaches are sufficient; for instance, if mixing by coagulation can be neglected relative to the condensation rate and no fresh emissions are entering the aerosol population, then all particles evolve equally and a sectional or moment-based scheme will capture the particle evolution. However, in the rapid dilution of young biofuel burning plumes, high coagulation and condensation rates affect particles' composition and size. Capturing the evolution of the mixing state may be important for predicting CCN activity. To obtain confidence in modeled outcomes in a rapidly-changing environment, it is necessary to use a scheme, such as a particle-resolved model, that avoids a priori approximations for the particle mixing state and size, hence PartMC-MOSAIC is a uniquely-suited tool for our study.

PartMC-MOSAIC has been used to model aerosol dynamics in urban areas (Riemer et al., 2009, 2010; Zaveri et al., 2010), CCN activation (Ching et al., 2012; Fierce et al., 2013) and ship plumes (Tian et al., 2014). Within PartMC-MOSAIC, we also implemented a module that reproduces the entrainment of background air (Jones, 2014), which allows for a variable water content in the plume.

PartMC-MOSAIC uses prescribed temporal profiles of plume dilution rate, specific humidity, and temperature. Their derivation is detailed in Sect. 2.2. The initial conditions for the simulations are the particle size distribution, the particle composition at emission, and the gas mixing ratios in the plume at emission. To examine plume behavior and sensitivities, these initial conditions are specified and varied as described in Sect. 2.3. In the following section we explain how PartMC-MOSAIC outputs can be used to describe the evolution of the CCN activity of biofuel burning particles.

2.1.1. CCN activation

PartMC-MOSAIC returns the composition of individual particles in the plume for each time step of the simulation, which we use to calculate the hygroscopicity of each particle. We use the κ-Köhler model here to calculate particle hygroscopicity (Petters and Kreidenweis, 2007). The hygroscopicity parameter κ comes from a parameterization of Köhler theory (Petters and Kreidenweis, 2007) and represents the hygroscopicity of a substance, that is, its capacity to uptake water. The value of κ for a particle is calculated as the volume-average of the κ of each aerosol component. With the value of κ and the particle size, the critical supersaturation at which each particle activates can be calculated using the κ-Köhler model

We also use several metrics to quantify CCN activity. First, the CCN efficiency is the fraction of particles that activate at a given supersaturation (s_{sat}). At a sufficiently large s_{sat}, all the particles activate and the CCN efficiency is one. Secondly, we calculate the critical supersaturation of the particle population, consisting of the supersaturation at which 5% ($ssat_5$), 50% ($ssat_{50}$), and 95% ($ssat_{95}$) of the plume particles activate. We also evaluate the Emission Index of CCN (EI_{CCN}), which is the total number of CCN present at plume-exit per mass of fuel burnt (units of kg^{-1}).

In laboratory or field measurements the particle population is not sampled directly at the flame but after a period of cooling, so we use 325 K as a reference temperature. We label parameters at this temperature with a '325' subscript, *e.g.* the particle number concentration N_{325}, or count median diameter CMD_{325}. We also calculate the number of CCN at plume-exit normalized to the number of particles at a plume temperature of 325 K, which we term CCN_{exit}/N_{325}. This parameter indicates the fraction of emitted particles that result in cloud-active particles, accounting for losses due to coagulation and lack of activity due to small size or hydrophobic nature. Similarly, we calculate the fraction of plume particles that reach plume-exit (N_{exit}/N_{325}). In the calculation, we normalize initial and final plume concentrations by the concentration of carbon monoxide (CO) to account for the plume dilution. Since coagulation is modeled as a stochastic process, repeated simulations are not identical, but EI_{CCN} differences are within about 3%.

2.2. Prescribed plume profiles used in PartMC-MOSAIC

2.2.1. Plume entrainment

Buoyancy-induced convection induces both vertical and horizontal dispersion (Trentmann et al., 2005, 2006). A higher dilution rate cools the plume faster, which lowers the saturation vapor pressure of semi-volatile organic compounds (SVOCs) and favors partitioning to the particle phase, but also lowers the concentration of SVOCs in the plume, which favors partitioning to the gas phase (Shrivastava et al., 2006). Hence, dilution influences the predicted concentration of species (Poppe et al., 1998; Mason et al., 2001; Shrivastava et al., 2006; Donahue et al., 2006).

We use the two-parameter dilution model from Von Glasow et al. (2003) to represent plume entrainment. This model describes a rising ellipsoidal plume as it rises. The gas or aerosol species concentration dilutes according to

$$\frac{dC_{pl}}{dt} = \frac{\alpha+\beta}{t}\left(C_{bg} - C_{pl}\right), \tag{1}$$

where C_{pl} and C_{bg} are the species' plume and background mass concentration, respectively, t is the time since emission, and α and β are empirical parameters describing the dilution in the horizontal and vertical direction, respectively. The solution to this equation is

$$C_{pl}(t) = C_{bkg} - \left(C_{bkg} - C_{pl}(t_0)\right) \times \left(\frac{t_0}{t}\right)^{\alpha+\beta}, \tag{2}$$

where t_0 is a reference time for the emission of the plume. Because we model dilution, rather than plume shape, we set $\alpha = \beta$ since one can choose different dilution rates by varying only one of the parameters.

2.2.2. Specific humidity profile

Combustion of biofuel produces water due to: (a) oxidation of the hydrogen contained in the fuel, also termed 'combustion moisture', which can be calculated from the stoichiometry of the combustion reaction, and (b) the release of the water present in the fuel that is not chemically bound to the organic molecules of the fuel. The latter is also termed 'fuel moisture', expressed as a percentage of the fuel mass (Parmar et al., 2008).

Combustion moisture ranges from 0.53 to 0.83 moles of water per mole of CO_2 emitted, depending on the type of biofuel (Parmar et al., 2008); we use 0.72 according to the fuel composition in Nussbaumer et al. (2003). A fuel moisture (wet basis) of 50% gives a total of 1.54 kg of water emitted per kg of biofuel combusted. This corresponds to a water mixing ratio of 4 x 10^4 ppm_v after stoichiometric combustion and complete evaporation, similar to the value Mason et al. (2001) used for a fresh biomass burning plume (10^4 ppm_v). The specific humidity profile (Figure 1a) is derived by using the dilution model (Eq. (1)) with an initial and background specific humidity of 0.15 and 0.01 kg/kg, respectively.

2.2.3. Temperature profile

The lower heating value of the fuel (16,000 kJ/kg; Boundy et al., 2011) combined with an energy balance gives the initial temperature of the parcel (1560 K) after stoichiometric combustion. The dilution model (Eq. (1)) provides the mass of air entrained from the background

at each time step. By combining this mass balance with an energy balance, one can derive the temperature at each condition. Discretizing the plume evolution in k = 1, 2, …, N time steps of width Δt = 0.05 s gives an equation for the temperature profile:

$$\mathrm{T}_{k+1} = \mathrm{T}_k \times \left(\frac{\mathrm{T}_k}{\mathrm{T_a}} \frac{\Delta t\,(\alpha+\beta)}{t_k} + \left(1 - \frac{\Delta t\,(\alpha+\beta)}{t_k}\right)\right)^{-1}, \tag{3}$$

where t_k is the time after emission at the k-th time step, $\mathrm{T_a}$ is the ambient temperature, and $\mathrm{T_1}$ is the stoichiometric combustion temperature. As explained in Sect. 2.2.1, we assume $\alpha = \beta$. Within 15 s the plume reaches ambient temperature and specific humidity (*i.e.*, plume-exit), so this time period is used for presentation.

2.2.4. Background species

Background aerosols and gases are brought into the plume by entrainment. The background gas composition is the same as in the work of Riemer et al. (2009), and there are no additional sources of particles or gases. Background aerosols are composed of 50% ammonium sulfate and 50% OC, are lognormally distributed with a count median diameter (CMD) of 500 nm, geometric standard deviation (GSD) of 1.3, and number concentration of 2.8 x 10^8 m^{-3}. We chose this low concentration, characteristic of a clean atmosphere, to focus on the evolution of the plume rather than the effects of background aerosols, since they can significantly affect the CCN activity of plume particles (Fierce et al., 2013).

2.3. Study design

About 300 PartMC-MOSAIC simulations with varying initial conditions were conducted, as summarized in Table 1. These initial conditions do not reproduce conditions exactly at the flame exit, because all reported measurements occur after some dilution and cooling. Instead, we chose initial conditions that produce plume-exit properties consistent with reported measurements. This allows an evaluation of how plume-exit properties are affected by in-plume dynamics. This section describes how initial conditions or other model parameters were varied to explore the sensitivities of plume-exit CCN. Table 1 also identifies an "illustrative case" which is used to introduce general plume behavior.

2.3.1. Initial condition: particle composition

The initial composition of the plume aerosols is taken from laboratory experiments of biomass combustion of chamise, ponderosa pine, and palmetto reported by Lewis et al. (2009). Composition of biofuel emissions other than BC and OC has not been reported, and, although biomass and biofuel aerosol emissions are not identical (Hays et al., 2002), the composition is similar (Woo et al., 2003); we use a range of compositions in this work. Since potassium is not represented in PartMC-MOSAIC, all potassium was apportioned as sodium (Na) following the work of Hand et al. (2010) and Zaveri et al. (2008). Detailed composition is given in Table 2. BC/OC ratios from in-use cooking with biofuel have been measured between about 0.05 and 0.6 (Roden et al., 2006), consistent with the values used here. Aerosols from the combustion of ponderosa pine have a lower BC/OC ratio and inorganic content than those from combustion of chamise, and aerosols from combustion of palmetto have a large inorganic content. The variability in inorganic content gives a wide range of hygroscopicities, as shown in Table 2.

In the initial model input, the aerosol is assigned the composition in Table 2. Some of the constituents may partition to the gas phase at high temperatures (Knudsen et al., 2004), and MOSAIC brings the system to equilibrium within 0.2 s.

2.3.2. Initial condition: particle size distribution

Particles at emission are assumed to follow a lognormal size distribution described by a Count Median Diameter (CMD) and Geometric Standard Deviation (GSD). Studies on residential stove emissions report measured CMD values between 50 and 300 nm, and GSD values between 1.3 and 2.2 (*e.g.*, Dasch et al., 1982; Hedberg et al., 2002; Tissari et al., 2007). For the initial size distribution we modeled a unimodal distribution with CMD_0 of 25, 50, 100, or 300 nm, and GSD_0 of 1.3. The corresponding initial particle number concentration was calculated using an emission factor of particulate matter (EF_{PM}) of 2, 4, 8, or 12 g/kg. We also modeled scenarios with GSD_0 of 1.1, 1.3, or 1.6, each with a CMD_0 of 25, 50, or 100 nm, each with EF_{PM} of 4 g/kg.

2.3.3. Initial condition: Gases and semi-volatile organic compounds

Table 3 presents EFs of the major gas species in the plume. To assemble a plume composition from diverse reports, we used the ratio between the EF of each species and the EF of CO, and multiplied it by a central estimate of EF_{CO} (42 g/kg, Akagi et al., 2011).

SVOCs affect the particle size and composition of emitted aerosols (Martin et al., 2013; Vakkari et al., 2014). The exact chemical identification of secondary organic species is not necessary for our purposes, instead only the volatility is important to describe partitioning in the plume (Donahue et al., 2006) because the short residence time in the plume precludes significant photochemical reactions. The species SVOC1 and SVOC2 in Table 3 are proxies for two SVOCs that we use to explore the effects of gases with different volatilities in the plume. MOSAIC uses the SORGAM scheme to model the formation and partitioning of low-volatility gas species. SVOC1 and SVOC2 correspond to two of eight model species specified in SORGAM with vapor pressures of 4.0×10^{-6} Pa and 1.2×10^{-4} Pa at 298 K, respectively.

To model different situations of total mass released, we used two values of emission factors (EF_{SVOC}) for all non-methane hydrocarbons: EF_{SVOC} of zero, representing a combustion event with no or negligible emissions of SVOCs, and 5.62 g/kg, a low estimate for cooking stoves (Akagi et al., 2011). Simulations with higher EF_{SVOC} values lead to the same conclusions.

2.3.4. Plume dilution rate

Dilution rate influences the predicted concentration of species in the plume, and hence, can affect the resulting particle composition and size. We model the range of dilution that could be expected in a biofuel burning plume, represented by the parameter α in Eq. (1). We estimate a value of α between 1 and 2 by comparing modeled and measured temperature profiles of a plume from a wood heating stove, as shown in Fig. S1. This is equivalent to a dilution rate between 1.0 and 2.7 s^{-1} when the plume reaches 325 K. Values of α smaller than 0.5 are not likely since this would correspond to dilution rate below 0.02 s^{-1} at 325 K, or a dilution ratio smaller than 5:1, and would take the plume more than 30 s to reach ambient temperature. On the other hand, values of α greater than 1 do not affect the mass of SVOC condensed, but reduce the coagulation rate so that changes in particle size and mixing state are less prounounced. Hence, simulations with α greater than 1 do not yield different CCN activity at plume-exit, although the

plume reaches ambient temperature faster. Therefore, we present scenarios modeled with $\alpha = \beta =$ 0.5, 0.7, and 1.0.

2.3.5. Mixing state: external vs. internal mixture as initial condition

Biofuel combustion is a dynamic process, varying between flaming and smoldering. Hence, the composition of the particles emitted is not perfectly homogeneous and might change with time. To assess the effect of the initial mixing state on plume-exit CCN we used as initial condition an external mixture containing three unimodal populations: an inorganic mode composed of ammonium sulfate, one of non-volatile OC, and one of BC. The three populations have the same CMD_0 and GSD_0, and the mass of each population follows the composition in Table 2 for κ_o of 0.11. We compare and contrast the results of the external mixture with a case where we assume an internal mixture of the same components as initial condition, with the same mass fractions as the external mixture case.

2.4. Role of Aitken mode particles in determining plume-exit CCN

Biofuel burning aerosols often have bimodal size distributions, containing an Aitken mode (particles less than 100 nm) and an accumulation mode (particles larger than 100 nm and less than one micrometer) (*e.g.*, Hedberg et al., 2002; Li et al., 2007). The particles in the Aitken mode have a high coagulation rate, and inorganic species are usually more abundant in this mode (Torvela et al., 2014).

We modeled a plume in which the initial distribution contained an Aitken mode with CMD_1 = 30 nm and an accumulation mode with CMD_2 = 100 nm. We studied two different cases: an internal mixture in which particles in both modes have the same composition, and an external mixture in which the Aitken mode is composed of only ammonium sulfate and the accumulation mode is composed of a mixture of BC and OC. We call these the 'homogeneous' and 'heterogeneous' bimodal distribution scenarios, respectively. In both cases the mass fractions of BC, OC, and ammonium sulfate of the overall population are the same. To study the effect of small particles on plume-exit CCN we also varied the initial concentration of the Aitken mode ($N_{0,Aitken}$), and changed the concentration of the accumulation mode to keep the same particulate mass emitted (EF_{PM} of 4 g/kg). Since the mass of ammonium sulfate varies with $N_{0,Aitken}$, the modeled composition differs from those described in Table 2 in these cases.

We also repeated simulations with either the Aitken or accumulation mode removed, leaving only the remaining mode as a unimodal distribution. By comparing the resulting activation properties of these simulations, we assessed the role of the Aitken mode aerosols on the resulting CCN concentration.

2.5. Simple estimates of condensation and coagulation

While PartMC-MOSAIC models the aerosol population in great detail, this detail may not be necessary to capture all aerosol evolution. We assess the plume processes that can be simplified or parameterized by comparing simple estimates of the evolution of particle properties with PartMC-MOSAIC predictions. These simple estimates are described below.

For coagulation, we estimated the number of particles lost at each time step using the formulation for a monodisperse aerosol distribution (Seinfeld and Pandis, 2006),

$$\frac{\mathrm{d}N}{\mathrm{dt}} = 4\sqrt{\frac{6k_{\mathrm{B}}\mathrm{T}D}{\rho}}\,N^2$$

where N is the particle number concentration, k_{B} is Boltzmann's constant, T is the plume's temperature, and D and ρ are the particle diameter and density, respectively.

Regarding condensation, from the total mass condensed determined by PartMC-MOSAIC, we derived the consequent increase in particle size (CMD) by assuming that the GSD stays constant. We also calculated an average hygroscopicity κ for all the plume particles to assess whether it could reproduce the results obtained with PartMC-MOSAIC. With the derived CMD, average κ, and particle number concentration, we estimated the plume-exit CCN and compared with PartMC-MOSAIC predictions. This discussion is presented in Sect. 3.1.

3. Results

We begin the discussion of results with an illustrative case (Sect. 3.1) that demonstrates the evolution within the plume for a reference case, and then evaluate how this evolution changes with variations in the initial conditions (Sections 3.2 through 3.5). Inputs for the illustrative case are listed in Table 1.

3.1. Illustrative case

Figure 1b shows the evolution of the mass concentration of the main aerosol species for the illustrative case. SVOCs condense within the first two seconds of the plume's evolution, driven by the rapid drop in temperature (Figure 1a). The increase in inorganic species shortly after SVOC condensation consists mostly of NH_4Cl that condenses at temperatures below 340 K (Zaveri et al., 2008). Condensation of NO_3 constitutes only 10% of the inorganic mass. Number concentration is also shown in Fig. 1b; it decreases faster than mass concentration due to coagulation.

The effect of the rapid condensation of SVOCs and inorganic species on particle size and hygroscopicity can be seen in Fig. 1c. CMD increases from 100 to 140 nm (black line), and the average κ of the plume aerosols increases from 0.004 to 0.06 (blue line). By repeating the simulations with either condensation or coagulation disabled and comparing the results, we conclude that about 20% of the increase in CMD can be attributed to coagulation, and the remaining 80% is from condensation of SVOCs. In this scenario, where the particles begin with a homogeneous composition, κ of individual particles changes only by condensation. Once the plume cools below 350 K (t=2.4 s), the CMD and average κ change by less than 1% and 3%, respectively. Since most particle sampling occurs at conditions below 300-325 K, aerosol properties measured at this temperature are sufficient to represent particles later in the evolution of a young plume.

Since condensation is the main cause of increased particle size and hygroscopicity, it is also the main factor driving particle activation. Coagulation increases CCN efficiency by about 20% by increasing particle size, but it also lowers plume-exit CCN by 25% due to the decrease in particle number. The increase in particle size and hygroscopicity leads to an increase in the fraction of particles that can become CCN, as shown in Fig. 1d for different s_{sat} values. About

half of the plume particles can activate at s_{sat} of 0.3%, while most, but not all, particles activate at s_{sat} of 0.5%. Regardless of the value of s_{sat} chosen, $CCN(t)/N_{325}$ changes by less than 3% after the initial rapid evolution of the plume.

Transformation in this illustrative case can be summarized as a rapid increase in particle size and hygroscopicity dominated by SVOC condensation, and a decrease in particle number concentration determined by the coagulation rate and plume dilution. Since condensation is the main factor, one can estimate activation with a simple analysis as described in Sect. 2.5. Using only the condensed SVOC mass to derive the increase in particle size, and both the condensed SVOC and inorganic mass to derive the increase in hygroscopicity, one can estimate a CCN efficiency within 15% of PartMC-MOSAIC's result, the mismatch being due to neglecting the growth by coagulation. Furthermore, using the monodisperse coagulation model to estimate the particle loss, one can estimate CCN_{exit}/N_{325} within 19%. Despite the complexity of the processes occurring in a fresh plume, at least in this illustrative case they can be qualitatively described with simple models.

3.2. Initial size and hygroscopicity, without co-emitted SVOCs

In this section we analyze the sensitivity of plume-exit CCN to initial particle size and composition, when SVOCs are not emitted simultaneously. Figure 2a to 2c show the scenarios analyzed: CMD_0 of 25, 50, 100, and 300 nm, and κ_0 of 0.004, 0.11, and 0.2.

Particles in all scenarios follow an evolution similar to that of the illustrative case: a rapid increase in hygroscopicity due to condensation of inorganic species (from κ_o = 0.004, 0.11, and 0.2, to κ_{325} = 0.02, 0.13, and 0.25, respectively), and in size due to the high coagulation rate, especially for small particles (from CMD_0 = 25, 50, 100, and 300 nm to CMD_{325} = 60, 78, 111 and 304 nm, respectively). In particular, it is not possible to obtain a CMD_{325} of 50 nm or smaller with an EF_{PM} above 3 g/kg due to the high coagulation rate. Below 325 K there is no more condensation, and coagulation is the only process affecting particle size. During the short time between this temperature and plume-exit, size changes by less than 5%.

Figure 2a shows the critical supersaturations of the particle populations at plume-exit for these scenarios. The mid-point is the supersaturation at which 50% of the plume particles become CCN ($ssat_{50}$), and the error bars indicate the supersaturation at which 5% ($ssat_5$) and 95% ($ssat_{95}$) of the particles become CCN. Despite the high critical supersaturations of small particles, *e.g.*, CMD_{325} below 100 nm in Fig. 2a, they can contribute substantially to CCN for supersaturations above 0.3%, as shown in Fig. 2b and Table 4. This is because more small particles are emitted for a given EF_{PM}. However, small particles with low inorganic content form CCN with low efficiency, with CCN_{exit}/N_{325} differing by up to a factor of 7 in the scenarios with κ_{325} of 0.02 and 0.25 (black columns in Fig. 2c).

We also conducted simulations using size distributions with GSD_0 of 1.1, 1.3, and 1.6, each with CMD_0 of 25, 50, or 100 nm. As with the CMD and κ, the GSD changes less than 5% below 325 K. Regarding CCN activity, the scenario with GSD_0 of 1.1 can have EI_{CCN} up to twice as large as with GSD_0 of 1.6. This is because a wider size distribution allocates some of the mass to particles too small to become CCN.

3.3. Effects of co-emitted SVOCs

The scenarios described in the previous sections were also modeled with co-emitted SVOCs (EF_{SVOC} of 5.62 g/kg). Results appear in Fig. 2d, 2e, and 2f. The main effect of co-emitted SVOCs is the particle size increase due to the added mass, and the consequent decrease in critical supersaturation as shown in Fig. 2d and Table 5. The change in hygroscopicity is more varied; simulations with EF_{SVOC} of 5.62 g/kg and an initial hygroscopicity κ_0 of 0.004, 0.11, and 0.20 changed to κ_{325} of 0.06, 0.11, and 0.16, respectively. Engelhart et al. (2012) observed a similar change in aged biomass burning plumes; condensation of organic species increases the hygroscopicity of hydrophobic particles, but decreases it for more hygroscopic particles. This is because SVOC condensation decreases the volume fraction of the (more hygroscopic) inorganic species. Hence, the inorganic content plays less of a role in determining the CCN activity of small particles when SVOCs are co-emitted, as can be seen by comparing Fig. 2c and 2f. Results of simulations with SVOC1 and SVOC2 are the same within a few percent.

For EF_{SVOC} above about 3 g/kg, condensation dominates the in-plume increase in particle size, change in hygroscopicity, and hence, critical supersaturation. This is shown in Table 5 for $ssat_{50}$ and different values of EF_{SVOC} and EF_{PM}. Changes in EF_{PM}, and hence, particle number emitted and their coagulation rate, have a small effect in $ssat_{50}$. For EF_{SVOC} smaller than about 3 g/kg, particles grow more by coagulation.

These results indicate that co-emission of SVOC material can be the main factor determining the CCN activity of biofuel burning aerosols. The CCN-modifying effect may be achieved only when SVOCs and primary aerosols are emitted simultaneously; it is not enough for them to be emitted from the same fire at different times.

3.4. Initial mixing state

In the previous scenarios, all particles had the same composition at emission. In this section we study the importance of the initial mixing state for plume-exit CCN. As initial condition we use an external mixture of three modes, OC, BC, and ammonium sulfate, all with the same size distribution, and we analyze how results differ from the case in which the initial aerosols are internally mixed, corresponding to κ_0 of 0.11 in Table 2. Unless otherwise stated, no SVOCs are co-emitted.

The particle size distribution follows the same evolution as in the previous scenarios. The hygroscopicity, however, is much more varied. Since PartMC-MOSAIC keeps track of the mode where each particle started, as well as each coagulation event, we can derive the fraction of particles that have coagulated with a particle from another mode. This is presented in Fig. 3, which shows pairs of graphs for four scenarios, with the left figure of each pair demonstrating the evolution of coagulated particles with time, and the right figure showing the plume-exit distribution of CCN as a function of supersaturation and particle type. Fig. 3b shows that coagulated and inorganic particles contribute the most to plume-exit CCN. Particles in the OC and BC mode that do not coagulate remain too hydrophobic or too small, and contribute to CCN only at supersaturations close to 1%.

The fraction of particles that coagulate with another mode is sensitive to initial size: about 1% for CMD_0 of 300 nm (CMD_{325} of 303 nm), 17% for CMD_0 of 100 nm (CMD_{325} of 110 nm, Figure 3a and 3b), and 97% for CMD_0 of 25 nm (CMD_{325} of 70 nm, Figure 3g and 3h). Slower dilution rates (Figure 3c) and higher EF_{PM} (Figure 3e) also increase the coagulation

between modes, but these factors affect plume-exit CCN substantially less than initial particle size, as can be seen by comparing Fig. 3d and 3f with Fig. 3h. A higher dilution rate ($\alpha = 1$) actually decreases the coagulation rate, hence it affects plume-exit CCN by just a few percent. While other research has indicated that dilution is an important factor in plume chemistry and aerosol composition (Shrivastava et al., 2006; Poppe et al., 2000; Donahue et al., 2006), their work addresses large plumes aging over hours, while our work focuses on small plumes and aging time scales of seconds.

As shown in Fig. 3a, most of the coagulation between modes occurs early in the evolution of the plume. This fraction of coagulated particles increases by less than 16% below 325 K. This implies that activation properties are set early in the plume evolution, with $ssat_{50}$ changing by only 10% between 325 K and plume exit.

Figure 4 shows how EI_{CCN} differs when particles of different size are externally mixed at emission, as compared with the internal mixture case (solid and dashed lines, respectively). For CMD_0 of 50 nm (black lines), EI_{CCN} of both mixing states is within 20%. For CMD_0 of 300 nm (blue lines) EI_{CCN} is the same within 5% for s_{sat} above 0.2%. The deviation grows with decreasing supersaturation, up to a factor of 2.5 at s_{sat} of 0.1%. This low sensitivity to initial mixing state occurs because small particles have a higher coagulation rate and hence have a more homogeneous composition at plume-exit. This is consistent with Che et al. (2016), who observed that particles growing in the Aitken mode become more internally mixed in part due to coagulation. On the other hand, large particles have a low critical supersaturation, regardless of mixing state. For intermediate particles with CMD_0 of 100 nm (red lines) EI_{CCN} differs by up to a factor of 4, indicating that particles are still externally mixed by plume-exit. However, when SVOCs are co-emitted (red dotted line), the two scenarios differ by only 5% to 20% (red dashed line), because the added SVOC mass also has a homogenizing effect on the composition of the particle population. Hence, the initial mixing state has a smaller effect on plume-exit CCN when SVOCs are co-emitted.

Figure 5 shows the distribution of critical supersaturation at plume-exit, similar to the presentation in Fig. 2. The distribution calculated using the composition from PartMC-MOSAIC is compared with the one using an average hygroscopicity for all particles. The use of an average hygroscopicity for particles that started with an external mixture leads to overestimating the κ of OC and BC particles, and hence, their contribution to CCN. This is consistent with the field studies of Wang et al. (2010) and Che et al. (2016), who found that the internal mixture assumption overestimates CCN number by 10% to 45%. Figure 5 shows that an average hygroscopicity underestimates $ssat_{50}$ by at least 60% in the scenarios with CMD_{325} of 110 nm, α of 0.5, or EF_{PM} of 12 g/kg. Since an average κ implies that all particles have the same hygroscopicity, its use also narrows the range of critical supersaturations (*i.e.*, $ssat_{95} - ssat_5$) by up to 80% for these scenarios. On the other hand, an average hygroscopicity is correct to within 10% for the case of small particles (CMD_{325} of 70 nm, top of Fig. 5) and 29% for a case with co-emitted SVOCs (EF_{SVOC} of 5.62 g/kg). Hence, there is less need to understand the initial mixing state when plume particles have either a small size at emission, or SVOCs are co-emitted. This is consistent with the findings of Fierce et al. (2013) in their study of CCN formation from diesel emissions under atmospheric aging, that is, that CCN number is less sensitive to initial mixing state under rapid aging by condensation.

3.5. Role of Aitken mode particles in determining plume-exit CCN

In Sect. 3.2 we showed that small particles, *i.e.*, those with a CMD_{325} smaller than 100 nm, can substantially contribute to plume-exit CCN (Figure 2). In this section we examine the CCN activity of these small particles when they are emitted in a bimodal distribution. We differentiate between homogeneous distributions, in which all particles have the same composition, or heterogeneous distributions, in which the Aitken mode is composed of ammonium sulfate and the accumulation mode contains BC and OC. For most of the simulations, we exclude co-emitted SVOCs in order to focus only on how the differently sized particles interact. All simulations use EF_{PM} of 4 g/kg.

Figure 6 shows EI_{CCN} for different initial relative concentrations of the Aitken ($N_{0,Aitken}$) and accumulation mode ($N_{0,Acc}$). We use the ratio between the two ($R_{Ait} = N_{0,Aitken}/N_{0,Acc}$) to indicate it. The figure also shows whether plume-exit CCN originate in the accumulation mode, the Aitken mode, or both (colored areas). When particles are heterogeneously mixed at emission, EI_{CCN} change by up to a factor of 2 from R_{Ait} of 0.25 (Figure 6a) to 8.4 (Figure 6c).

Figure 6 also shows the CCN spectra if the same size distribution were emitted with a homogeneous composition (black dashed lines). When the homogeneous-composition curves differ from the heterogeneous scenario (area graph), then identifying compositional differences between Aitken and accumulation mode is important. Also shown in the Figure are the CCN if the accumulation mode component of the size distribution were emitted alone (red dotted lines), and if the Aitken mode component were emitted alone (blue dashed lines). Comparison between the bimodal result and the accumulation or Aitken mode spectra shows how the interaction between the modes affects plume-exit CCN. When these curves differ, plume-exit CCN would differ if the two modes were emitted simultaneously or sequentially.

For R_{Ait} less than 1 (Figure 6a), most of the CCN originate with accumulation-mode particles. EI_{CCN} decreases by less than 17% when the simulation is repeated with the Aitken mode removed (red dashed line). On the other hand, when $N_{0,Aitken}$ is similar to $N_{0,Acc}$ (Figure 6b), most of the CCN have a component from the Aitken mode. A simulation using only the Aitken mode gives EI_{CCN} within a few percent of the bimodal distribution (blue dashed line), indicating that the accumulation mode does not contribute much to EI_{CCN}. When the Aitken-mode number concentration is much higher than that in the accumulation mode (Figure 6c), most CCN also have a component from the Aitken mode, and the presence of the accumulation mode can actually decrease EICCN due to the higher coagulation rate and particle loss, as shown by the comparison with the Aitken-only simulation (blue dashed line). Increasing $N_{0,Aitken}$ increases plume-exit CCN because it increases the inorganic mass in the plume (by a factor of 4 in Fig. 6c compared to Fig. 6b), and also the hygroscopicity of OC and BC particles that coagulate with inorganic particles, as discussed in Sect. 3.4.

When particles are initialized with a homogeneous composition (black lines in Fig. 6), the number of particles originally in the Aitken mode has a small effect on EI_{CCN}. Varying R_{Ait} from the minimum (Figure 6a) to the maximum case (Figure 6c) changes EI_{CCN} by 7%, because the accumulation mode is already hygroscopic enough to become CCN.

Figure 7 summarizes plume-exit properties for simulations in which the initial distribution is a bimodal, heterogeneous distribution. Figure 7a shows the critical supersaturation distribution within each particle population for the composition from PartMC-MOSAIC (blue), beginning with either a homogeneous or a heterogeneous population. The critical saturation that

would be predicted with the use of an average κ across all particles is also shown (red). Accumulation-mode (squares) and Aitken mode (triangles) are separated. In the heterogeneous case, the inorganic mass is found in the Aitken mode; artificially spreading this mass across the entire particle distribution with an average κ leads to overestimating the critical supersaturation of the Aitken mode and underestimating that of the accumulation mode.

Figures 7b and 7c summarize EI_{CCN} for two atmospherically-relevant values of s_{sat}: 0.3% and 0.7%. At s_{sat} of 0.3% (Figure 7b), the use of an average κ disagrees with PartMC results by 61% for R_{Ait} of 8.4, to a factor of 47 for R_{Ait} of 0.25. This occurs because the uncoagulated particles emitted at R_{Ait} of 0.25 have a great diversity in composition. When SVOCs are co-emitted, particles become hygroscopic and also reduce the diversity in κ; the estimated EI_{CCN} agrees within 48% at s_{sat} of 0.3%. At higher supersaturations (s_{sat} of 0.7% in Fig. 7c), most particles can function as CCN, and the disagreement in EI_{CCN} is at most 27%.

4. Summary and conclusion

We modeled the evolution of a biofuel burning plume from emission until it reaches ambient temperature and RH, for a variety of initial conditions and plume properties, with the objective of improving estimates of emitted CCN from residential biofuel combustion. The main findings of this study are:

- After the plume dilutes and temperature drops below 350 K (t = 2.4 s for $\alpha = \beta = 0.7$), particle size and κ values change by less than 5%. This is observed in all scenarios.
- Co-emission of SVOCs can be the main factor determining plume-exit CCN for hydrophobic or small particles, increasing EI_{CCN} by up to three orders of magnitude. If particles are already large and hygroscopic enough to activate at emission, co-emission of SVOCs has a small effect on EI_{CCN} (less than 5%).
- Some combinations of emission factor and size are impossible because of rapid plume coagulation. The upper limit of EI_{CCN} is about 10^{16} kg^{-1}. Depending on emission factor, particle size, and composition, some of these particles may not activate at low s_{sat}. For EF_{PM} greater than 3 g/kg, plume-exit CMD is at least 50 nm.
- When particles are emitted with smaller diameters, more CCN result from the same emitted mass, yet these particles activate at higher supersaturations. For particle diameters below 100 nm, 10-80% of the particles can serve as CCN at atmospheric supersaturations. This dependence on initial particle size and hygroscopicity is shown in Fig. 2.
- When particles are emitted as a bimodal distribution, the Aitken mode contributes less than 2% to the plume-exit CCN if both modes have the same composition.
- When the number concentration of more-hygroscopic Aitken mode particles is high compared to less-hygroscopic accumulation mode particles, the Aitken mode particles can create additional CCN through self-coagulation, but they have little effect on the CCN activity of accumulation-mode particles despite a large number of coagulation events between Aitken mode and accumulation mode particles.
- A simple model (monodisperse coagulation and average hygroscopicity) can be used to estimate plume-exit CCN within about 20% if particles are unimodal and have homogeneous composition. The simple model would underestimate particle loss by coagulation in a bimodal distribution by at least an order of magnitude.

- External mixtures become more internally mixed when particles are emitted in the Aitken mode, due to the higher coagulation rate, or with co-emitted SVOCs due to the homogenizing effect of the added mass.
- Plume-exit average hygroscopicity can be used to estimate EI_{CCN} within 5-20% if particles are emitted in the Aitken mode, even if externally-mixed subpopulations exist within the Aitken mode. This is also true when SVOCs are co-emitted. The estimate improves as the particle size decreases, EF_{PM} increases, or EF_{SVOC} increases, since these factors enhance internal mixing in the particle population.
- On the other hand, if externally-mixed particles are emitted in the accumulation mode without SVOCs, an average κ overestimates hygroscopicity, and hence overestimate EI_{CCN} by up to a factor of 2.

This work has identified conditions under which particle populations become more homogeneous during plume processes. This homogenizing effect requires the components to be truly co-emitted. Sequential emission, even if separated by a few seconds, results in greater heterogeneity.

Atmospheric aging through coating or coagulation also affects the relationship between emitted particles and cloud influence (e.g. Fierce et al., 2014). The findings here are important because they describe (1) limitations in the emitted size distributions of primary particles, (2) the nature of directly-emitted particles near sources, before atmospheric aging has occurred, and (3) the nature of atmospheric particles when other atmospheric aging is slow.

Experimental verification of the important findings could include observations of EI_{CCN} using a CCN counter, compared with gaseous carbon emissions, to demonstrate that EI_{CCN} is limited to 10^{16} kg^{-1}. The effect of co-emitted SVOCs could be evaluated by comparing CCN activity of a plume at different dilution ratios, where SVOCs would be expected to partition to the gas phase in the most dilute environments. The conditions under which the average-hygroscopicity assumption is expected to fail could be confirmed by performing CCN closure studies on aerosol generated with those specific characteristics; that is, aerosol size and composition could be measured with an Aerodyne Mass Spectrometer, and then CCN predicted from those values could be compared to measurements. Because biofuel emissions vary during the course of combustion, and because simultaneous emission affects the particle properties, these experiments should be conducted in real-time or on emissions from isolated phases of burning.

5. References

Akagi, S. K., Yokelson, R. J., Wiedinmyer, C., Alvarado, M. J., Reid, J. S., Karl, T., Crounse, J. D., and Wennberg, P. O.: Emission factors for open and domestic biomass burning for use in atmospheric models, Atmospheric Chemistry and Physics, 11, 4039-4072, 10.5194/acp-11-4039-2011, 2011.

Alvarado, M. J., and Prinn, R. G.: Formation of ozone and growth of aerosols in young smoke plumes from biomass burning: 1. Lagrangian parcel studies, Journal of Geophysical Research-Atmospheres, 114, D0930610.1029/2008jd011144, 2009.

Bailis, R., Cowan, A., Berrueta, V., and Masera, O.: Arresting the Killer in the Kitchen: The Promises and Pitfalls of Commercializing Improved Cookstoves, World Development, 37, 1694-1705, 10.1016/j.worlddev.2009.03.004, 2009.

Bauer, S. E., Menon, S., Koch, D., Bond, T. C., and Tsigaridis, K.: A global modeling study on carbonaceous aerosol microphysical characteristics and radiative effects, Atmospheric Chemistry and Physics, 10, 2010.

Boman, C., Pettersson, E., Westerholm, R., Bostrom, D., and Nordin, A.: Stove Performance and Emission Characteristics in Residential Wood Log and Pellet Combustion, Part 1: Pellet Stoves, Energy & Fuels, 25, 307-314, 10.1021/ef100774x, 2011.

Bond, T. C., Streets, D. G., Yarber, K. F., Nelson, S. M., Woo, J. H., and Klimont, Z.: A technology-based global inventory of black and organic carbon emissions from combustion, Journal of Geophysical Research-Atmospheres, 109, D1420310.1029/2003jd003697, 2004.

Boucher, O., Randall, D., Artaxo, P., Bretherton, C., Feingold, G., Forster, P., Kerminen, V. M., Kondo, Y., Liao, H., and Lohmann, U.: Clouds and aerosols, in: Climate change 2013: The physical science basis. Contribution of working group I to the fifth assessment report of the intergovernmental panel on climate change, Cambridge University Press, 571-657, 2013.

Boundy, R. G., Diegel, S. W., Wright, L. L., and Davis, S. C.: Biomass energy data book, 2011.

Burling, I. R., Yokelson, R. J., Griffith, D. W. T., Johnson, T. J., Veres, P., Roberts, J. M., Warneke, C., Urbanski, S. P., Reardon, J., Weise, D. R., Hao, W. M., and de Gouw, J.: Laboratory measurements of trace gas emissions from biomass burning of fuel types from the southeastern and southwestern United States, Atmospheric Chemistry and Physics, 10, 11115-11130, 10.5194/acp-10-11115-2010, 2010.

Che, H. C., Zhang, X. Y., Wang, Y. Q., Zhang, L., Shen, X. J., Zhang, Y. M., Ma, Q. L., Sun, J. Y., Zhang, Y. W., and Wang, T. T.: Characterization and parameterization of aerosol cloud condensation nuclei activation under different pollution conditions, Scientific Reports, 6, 2016.

Ching, J., Riemer, N., and West, M.: Impacts of black carbon mixing state on black carbon nucleation scavenging: Insights from a particle-resolved model, Journal of Geophysical Research-Atmospheres, 117, 10.1029/2012jd018269, 2012.

Christian, T. J., Yokelson, R. J., Cardenas, B., Molina, L. T., Engling, G., and Hsu, S. C.: Trace gas and particle emissions from domestic and industrial biofuel use and garbage burning in central Mexico, Atmospheric Chemistry and Physics, 10, 565-584, 2010.

Chuen-Yu, C., Guenter, E., Xuefang, S., and Ting, Z.: Biofuel Combustion Emissions - Chemical and Physical Smoke Properties, Environmental Impact of Biofuels, 2011.

Clark, M. L., Reynolds, S. J., Burch, J. B., Conway, S., Bachand, A. M., and Peel, J. L.: Indoor air pollution, cookstove quality, and housing characteristics in two Honduran communities, Environmental Research, 110, 12-18, DOI: 10.1016/j.envres.2009.10.008, 2010.

Crutzen, P. J., and Andreae, M. O.: Biomass burning in the tropics: impact on atmospheric chemistry and biogeochemical cycles, Science (New York, NY), 250, 1669, 1990.

Cynthia, A. A., Edwards, R. D., Johnson, M., Zuk, M., Rojas, L., Jimenez, R. D., Riojas-Rodriguez, H., and Masera, O.: Reduction in personal exposures to particulate matter and carbon monoxide as a result of the installation of a Patsari improved cook stove in Michoacan Mexico, Indoor Air, 18, 93-105, 10.1111/j.1600-0668.2007.00509.x, 2008.

Dasch, J. M.: Particulate and gaseous emissions from wood-burning fireplaces, Environmental Science & Technology, 16, 639-645, 1982.

Dentener, F., Kinne, S., Bond, T., Boucher, O., Cofala, J., Generoso, S., Ginoux, P., Gong, S., Hoelzemann, J. J., Ito, A., Marelli, L., Penner, J. E., Putaud, J. P., Textor, C., Schulz, M., van der Werf, G. R., and Wilson, J.: Emissions of primary aerosol and precursor gases in the years 2000 and 1750 prescribed data-sets for AeroCom, Atmospheric Chemistry and Physics, 6, 4321-4344, 2006.

Donahue, N. M., Robinson, A. L., Stanier, C. O., and Pandis, S. N.: Coupled partitioning, dilution, and chemical aging of semivolatile organics, Environmental Science & Technology, 40, 2635-2643, 10.1021/es052297c, 2006.

Donahue, N. M., Robinson, A. L., Pandis, S. N., Kroll, J. H., and Worsnop, D. L.: Rethinking organic aerosols: Semivolatile emissions and photochemical aging, Geochimica Et Cosmochimica Acta, 73, A299-A299, 2009.

Engelhart, G. J., Hennigan, C. J., Miracolo, M. A., Robinson, A. L., and Pandis, S. N.: Cloud condensation nuclei activity of fresh primary and aged biomass burning aerosol, Atmospheric Chemistry and Physics, 12, 7285-7293, 2012.

Ezzati, M., Mbinda, B. M., and Kammen, D. M.: Comparison of emissions and residential exposure from traditional and improved cookstoves in Kenya, Environmental Science & Technology, 34, 578-583, 2000.

Ezzati, M., and Kammen, D. M.: The health impacts of exposure to indoor air pollution from solid fuels in developing countries: Knowledge, gaps, and data needs, Environmental Health Perspectives, 110, 1057-1068, 2002.

Fierce, L., Riemer, N., and Bond, T. C.: When is cloud condensation nuclei activity sensitive to particle characteristics at emission?, Journal of Geophysical Research: Atmospheres, 2013.

Fierce, L., Riemer, N., and Bond, T.: Explaining variance in black carbon's aging timescale, Atmos. Chem. Phys. Discuss., 14, 18703-18737, 10.5194/acpd-14-18703-2014, 2014.

Forster, P., Ramaswamy, V., P., A., Berntsen, T., Betts, R., Fahey, D. W., Haywood, J., Lean, J., Lowe, D. C., Myhre, G., Nganga, J., Prinn, R., Raga, G., Schulz, M., and Van Dorland, R.: Changes in Atmospheric Constituents and in Radiative Forcing. In: Climate Change 2007: The Physical Science Basis. Contribution of Working Group I to the Fourth Assessment Report of the Intergovernmental Panel on Climate Change, 2007.

Gao, S., Hegg, D. A., Hobbs, P. V., Kirchstetter, T. W., Magi, B. I., and Sadilek, M.: Water-soluble organic components in aerosols associated with savanna fires in southern Africa: Identification, evolution, and distribution, Journal of Geophysical Research-Atmospheres, 108, 10.1029/2002jd002324, 2003.

Garba, M. U., Ingham, D. B., Ma, L., Porter, R. T. J., Pourkashnian, M., Tan, H. Z., and Williams, A.: Prediction of Potassium Chloride Sulfation and Its Effect on Deposition in Biomass-Fired Boilers, Energy & Fuels, 26, 6501-6508, 10.1021/ef201681t, 2012.

Grieshop, A. P., Reynolds, C. C. O., Kandlikar, M., and Dowlatabadi, H.: A black-carbon mitigation wedge, Nature Geosci, 2, 533-534, 2009.

Grieshop, A. P., Marshall, J. D., and Kandlikar, M.: Health and climate benefits of cookstove replacement options, Energy Policy, 39, 10.1016/j.enpol.2011.03.024, 2011.

Gustafsson, O., Krusa, M., Zencak, Z., Sheesley, R. J., Granat, L., Engstrom, E., Praveen, P. S., Rao, P. S. P., Leck, C., and Rodhe, H.: Brown Clouds over South Asia: Biomass or Fossil Fuel Combustion?, Science, 323, 495-498, 10.1126/science.1164857, 2009.

Hand, J. L., Day, D. E., McMeeking, G. M., Levin, E. J. T., Carrico, C. M., Kreidenweis, S. M., Malm, W. C., Laskin, A., and Desyaterik, Y.: Measured and modeled humidification factors of fresh smoke particles from biomass burning: role of inorganic constituents, Atmos. Chem. Phys. Discuss., 10, 4225-4269, 10.5194/acpd-10-4225-2010, 2010.

Hays, M. D., Geron, C. D., Linna, K. J., Smith, N. D., and Schauer, J. J.: Speciation of gas-phase and fine particle emissions from burning of foliar fuels, Environmental Science & Technology, 36, 2281-2295, 2002.

Hedberg, E., Kristensson, A., Ohlsson, M., Johansson, C., Johansson, P. A., Swietlicki, E., Vesely, V., Wideqvist, U., and Westerholm, R.: Chemical and physical characterization of emissions from birch wood combustion in a wood stove, Atmospheric Environment, 36, 4823-4837, 2002.

Hindiyarti, L., Frandsen, F., Livbjerg, H., Glarborg, P., and Marshall, P.: An exploratory study of alkali sulfate aerosol formation during biomass combustion, Fuel, 87, 1591-1600, 10.1016/j.fuel.2007.09.001, 2008.

Hobbs, P. V., Sinha, P., Yokelson, R. J., Christian, T. J., Blake, D. R., Gao, S., Kirchstetter, T. W., Novakov, T., and Pilewskie, P.: Evolution of gases and particles from a savanna fire in South Africa, Journal of Geophysical Research-Atmospheres, 108, 10.1029/2002jd002352, 2003.

Jacobson, M. Z.: Development and application of a new air pollution modeling system .2. Aerosol module structure and design, Atmospheric Environment, 31, 131-144, 10.1016/1352-2310(96)00202-6, 1997.

Jacobson, M. Z.: A physically-based treatment of elemental carbon optics: Implications for global direct forcing of aerosols, Geophysical Research Letters, 27, 217-220, 2000.

Jacobson, M. Z.: Effects of externally-through-internally-mixed soot inclusions within clouds and precipitation on global climate, Journal of Physical Chemistry A, 110, 6860-6873, 10.1021/jp056391r, 2006.

Jacobson, M. Z.: Short-term effects of controlling fossil-fuel soot, biofuel soot and gases, and methane on climate, Arctic ice, and air pollution health, Journal of Geophysical Research-Atmospheres, 115, D1420910.1029/2009jd013795, 2010.

Johnson, M., Edwards, R., Frenk, C. A., and Masera, O.: In-field greenhouse gas emissions from cookstoves in rural Mexican households, Atmospheric Environment, 42, 1206-1222, 10.1016/j.atmosenv.2007.10.034, 2008.

Johnson, M., Edwards, R., Ghilardi, A., Berrueta, V., Gillen, D., Frenk, C. A., and Masera, O.: Quantification of Carbon Savings from Improved Biomass Cookstove Projects, Environmental Science & Technology, 43, 2456-2462, 10.1021/es801564u, 2009.

Johnson, M., Edwards, R., and Masera, O.: Improved stove programs need robust methods to estimate carbon offsets, Climatic Change, 2010.

Jones, A.: Investigating the impacts of entrainment on nucleation scavenging of black carbon particles through particle-resolved simulations, M.S., Atmospheric Sciences, University of Illinois at Urbana Champaign, http://hdl.handle.net/2142/49492, 2014.

Jost, C., Trentmann, J., Sprung, D., Andreae, M. O., McQuaid, J. B., and Barjat, H.: Trace gas chemistry in a young biomass burning plume over Namibia: Observations and model simulations, Journal of Geophysical Research-Atmospheres, 108, 848210.1029/2002jd002431, 2003.

Knudsen, J. N., Jensen, P. A., and Dam-Johansen, K.: Transformation and release to the gas phase of Cl, K, and S during combustion of annual biomass, Energy & Fuels, 18, 1385-1399, 10.1021/ef049944q, 2004.

Koch, D., Balkanski, Y., Bauer, S. E., Easter, R. C., Ferrachat, S., Ghan, S. J., Hoose, C., Iversen, T., Kirkevag, A., Kristjansson, J. E., Liu, X., Lohmann, U., Menon, S., Quaas, J., Schulz, M., Seland, O., Takemura, T., and Yan, N.: Soot microphysical effects on liquid clouds, a multi-model investigation, Atmospheric Chemistry and Physics, 11, 10.5194/acp-11-1051-2011, 2011.

Legros, G., Havet, I., Bruce, N., and Bonjour, S.: The Energy Access Situation in Developing Countries. World Health Organization and UNDP http://www.who.int/indoorair/publications/energyaccesssituation/en/index.html, 2009.

Lewis, K., Arnott, W., Moosmüller, H., Chakrabarty, R., Carrico, C., Kreidenweis, S., Day, D., Malm, W., Laskin, A., and Jimenez, J.: Reduction in biomass burning aerosol light absorption upon humidification: roles of inorganically-induced hygroscopicity, particle collapse, and photoacoustic heat and mass transfer, Atmos. Chem. Phys, 9, 8949-8966, 2009.

Li, X., Duan, L., Wang, S., Duan, J., Guo, X., Yi, H., Hu, J., Li, C., and Hao, J.: Emission characteristics of particulate matter from rural household biofuel combustion in China, Energy Fuels, 21, 845-851, 2007.

Lim, S. S., Vos, T., and Flaxman, A. D.: A comparative risk assessment of burden of disease and injury attributable to 67 risk factors and risk factor clusters in 21 regions, 1990-2010: a systematic analysis for the Global Burden of Disease Study 2010 (vol 380, pg 2224, 2012), Lancet, 381, 1276-1276, 2013.

Liousse, C., Penner, J. E., Chuang, C., Walton, J. J., Eddleman, H., and Cachier, H.: A global three-dimensional model study of carbonaceous aerosols, Journal of Geophysical Research-Atmospheres, 101, 19411-19432, 10.1029/95jd03426, 1996.

Ludwig, J., Marufu, L. T., Huber, B., Andreae, M. O., and Helas, G.: Domestic combustion of biomass fuels in developing countries: A major source of atmospheric pollutants, Journal of Atmospheric Chemistry, 44, 23-37, 10.1023/a:1022159910667, 2003.

Mann, G. W., Carslaw, K. S., Reddington, C. L., Pringle, K. J., Schulz, M., Asmi, A., Spracklen, D. V., Ridley, D. A., Woodhouse, M. T., Lee, L. A., Zhang, K., Ghan, S. J., Easter, R. C., Liu, X., Stier, P., Lee, Y. H., Adams, P. J., Tost, H., Lelieveld, J., Bauer, S. E., Tsigaridis, K., van Noije, T. P. C., Strunk, A., Vignati, E., Bellouin, N., Dalvi, M., Johnson, C. E., Bergman, T., Kokkola, H., von Salzen, K., Yu, F., Luo, G., Petzold, A., Heintzenberg, J., Clarke, A., Ogren, A., Gras, J., Baltensperger, U., Kaminski, U., Jennings, S. G., O'Dowd, C. D., Harrison, R. M., Beddows, D. C. S., Kulmala, M., Viisanen, Y., Ulevicius, V., Mihalopoulos, N., Zdimal,

V., Fiebig, M., Hansson, H. C., Swietlicki, E., and Henzing, J. S.: Intercomparison and evaluation of global aerosol microphysical properties among AeroCom models of a range of complexity, Atmospheric Chemistry and Physics, 14, 4679-4713, 2014.

Martin, M., Tritscher, T., Juranyi, Z., Heringa, M. F., Sierau, B., Weingartner, E., Chirico, R., Gysel, M., Prevot, A. S. H., Baltensperger, U., and Lohmann, U.: Hygroscopic properties of fresh and aged wood burning particles, Journal of Aerosol Science, 56, 15-29, 10.1016/j.jaerosci.2012.08.006, 2013.

Mason, S. A., Field, R. J., Yokelson, R. J., Kochivar, M. A., Tinsley, M. R., Ward, D. E., and Hao, W. M.: Complex effects arising in smoke plume simulations due to inclusion of direct emissions of oxygenated organic species from biomass combustion, Journal of Geophysical Research-Atmospheres, 106, 12527-12539, 10.1029/2001jd900003, 2001.

McGraw, R.: Description of aerosol dynamics by the quadrature method of moments, Aerosol Science and Technology, 27, 255-265, 10.1080/02786829708965471, 1997.

Nussbaumer, T.: Combustion and co-combustion of biomass: fundamentals, technologies, and primary measures for emission reduction, Energy & Fuels, 17, 1510-1521, 10.1021/ef030031q, 2003.

Parmar, R. S., Welling, M., Andreae, M. O., and Helas, G.: Water vapor release from biomass combustion, Atmospheric Chemistry and Physics, 8, 6147-6153, 2008.

Petters, M., and Kreidenweis, S.: A single parameter representation of hygroscopic growth and cloud condensation nucleus activity, Atmospheric Chemistry and Physics, 7, 1961-1971, 2007.

Poppe, D., Koppmann, R., and Rudolph, J.: Ozone formation in biomass burning plumes: Influence of atmospheric dilution, Geophysical Research Letters, 25, 3823-3826, 10.1029/1998gl900046, 1998.

Pratt, K. A., S. M. Murphy, R. Subramanian, P. J. DeMott, G. L. Kok, T. Campos, D. C. Rogers, A. J. Prenni, A. J. Heymsfield, J. H. Seinfeld, and K. A. Prather, 2011, Flight-based chemical characterization of biomass burning aerosols within two prescribed burn smoke plumes: Atmospheric Chemistry and Physics, v. 11.

Ramanathan, V., and Carmichael, G.: Global and regional climate changes due to black carbon, Nature Geoscience, 1, 221-227, 10.1038/ngeo156, 2008.

Rau, J. A.: Composition And Size Distribution Of Residential Wood Smoke Particles, Aerosol Science and Technology, 10, 181-192, 10.1080/02786828908959233, 1989.

Riemer, N., West, M., Zaveri, R. A., and Easter, R. C.: Simulating the evolution of soot mixing state with a particle-resolved aerosol model, Journal of Geophysical Research-Atmospheres, 114, 10.1029/2008jd011073, 2009.

Riemer, N., West, M., Zaveri, R., and Easter, R.: Estimating black carbon aging time-scales with a particle-resolved aerosol model, Journal of Aerosol Science, 41, 143-158, 10.1016/j.jaerosci.2009.08.009, 2010.

Robinson, A. L., Donahue, N. M., Shrivastava, M. K., Weitkamp, E. A., Sage, A. M., Grieshop, A. P., Lane, T. E., Pierce, J. R., and Pandis, S. N.: Rethinking organic aerosols: Semivolatile emissions and photochemical aging, Science, 315, 1259-1262, 10.1126/science.1133061, 2007.

Roden, C. A., Bond, T. C., Conway, S., Benjamin, A., and Pinel, O.: Emission factors and real-time optical properties of particles emitted from traditional wood burning cookstoves, Environmental Science & Technology, 40, 6750-6757, 10.1021/es052080i, 2006.

Schell, B., Ackermann, I. J., Hass, H., Binkowski, F. S., and Ebel, A.: Modeling the formation of secondary organic aerosol within a comprehensive air quality model system, Journal of Geophysical Research-Atmospheres, 106, 28275-28293, 10.1029/2001jd000384, 2001.

Seinfeld, J. H. and Pandis, S. N.: Atmospheric chemistry and physics: from air pollution to climate change, Atmospheric chemistry and physics: from air pollution to climate change, xxviii + 1203 pp., 2006.

Seinfeld, J. H., Bretherton, C., Carslaw, K. S., Coe, H., DeMott, P. J., Dunlea, E. J., Feingold, G., Ghan, S., Guenther, A. B., Kahn, R., Kraucunas, I., Kreidenweis, S. M., Molina, M. J., Nenes, A., Penner, J. E., Prather, K. A., Ramanathan, V., Ramaswamy, V., Rasch, P. J., Ravishankara, A. R., Rosenfeld, D., Stephens, G., and Wood, R.: Improving our fundamental understanding of the role of aerosol-cloud interactions in the climate

system, Proceedings of the National Academy of Sciences of the United States of America, 113, 5781-5790, 2016.

Shrivastava, M. K., Lipsky, E. M., Stanier, C. O., and Robinson, A. L.: Modeling semivolatile organic aerosol mass emissions from combustion systems, Environmental Science & Technology, 40, 2671-2677, 10.1021/es0522231, 2006.

Textor, C., Schulz, M., Guibert, S., Kinne, S., Balkanski, Y., Bauer, S., Berntsen, T., Berglen, T., Boucher, O., Chin, M., Dentener, F., Diehl, T., Easter, R., Feichter, H., Fillmore, D., Ghan, S., Ginoux, P., Gong, S., Kristjansson, J. E., Krol, M., Lauer, A., Lamarque, J. F., Liu, X., Montanaro, V., Myhre, G., Penner, J., Pitari, G., Reddy, S., Seland, O., Stier, P., Takemura, T., and Tie, X.: Analysis and quantification of the diversities of aerosol life cycles within AeroCom, Atmospheric Chemistry and Physics, 6, 1777-1813, 2006.

Tian, J., Riemer, N., Pfaffenberger, L., Schlager, H., and Petzold, A.: Modeling the evolution of aerosol particles in a ship plume using PartMC-MOSAIC, Atmos. Chem. Phys. Discuss., 13, 16733-16774, 10.5194/acpd-13-16733-2013, 2013.

Tissari, J., Hytönen, K., Lyyränen, J., and Jokiniemi, J.: A novel field measurement method for determining fine particle and gas emissions from residential wood combustion, Atmospheric environment, 41, 8330-8344, 2007.

Tissari, J., Lyyränen, J., Hytönen, K., Sippula, O., Tapper, U., Frey, A., Saarnio, K., Pennanen, A., Hillamo, R., and Salonen, R.: Fine particle and gaseous emissions from normal and smouldering wood combustion in a conventional masonry heater, Atmospheric Environment, 42, 7862-7873, 2008.

Torvela, T., Tissari, J., Sippula, O., Kaivosoja, T., Leskinen, J., Virén, A., Lähde, A., and Jokiniemi, J.: Effect of wood combustion conditions on the morphology of freshly emitted fine particles, Atmospheric Environment, 87, 65-76, http://dx.doi.org/10.1016/j.atmosenv.2014.01.028, 2014.

Trentmann, J., Andreae, M. O., Graf, H. F., Hobbs, P. V., Ottmar, R. D., and Trautmann, T.: Simulation of a biomass-burning plume: Comparison of model results with observations, Journal of Geophysical Research-Atmospheres, 107, 10.1029/2001jd000410, 2002.

Trentmann, J., Andreae, M. O., and Graf, H. F.: Chemical processes in a young biomass-burning plume, Journal of Geophysical Research-Atmospheres, 108, 10.1029/2003jd003732, 2003.

Trentmann, J., Yokelson, R. J., Hobbs, P. V., Winterrath, T., Christian, T. J., Andreae, M. O., and Mason, S. A.: An analysis of the chemical processes in the smoke plume from a savanna fire, Journal of Geophysical Research-Atmospheres, 110, D1230110.1029/2004jd005628, 2005.

Trentmann, J., Luderer, G., Winterrath, T., Fromm, M. D., Servranckx, R., Textor, C., Herzog, M., Graf, H. F., and Andreae, M. O.: Modeling of biomass smoke injection into the lower stratosphere by a large forest fire (Part I): reference simulation, Atmospheric Chemistry and Physics, 6, 5247-5260, 2006.

Vakkari, V., Kerminen, V.-M., Beukes, J. P., Tiitta, P., van Zyl, P. G., Josipovic, M., Venter, A. D., Jaars, K., Worsnop, D. R., Kulmala, M., and Laakso, L.: Rapid changes in biomass burning aerosols by atmospheric oxidation, Geophysical Research Letters, 41, 2644-2651, 10.1002/2014gl059396, 2014.

Venkataraman, C., Habib, G., Eiguren-Fernandez, A., Miguel, A. H., and Friedlander, S. K.: Residential biofuels in south Asia: Carbonaceous aerosol emissions and climate impacts, Science, 307, 10.1126/science.1104359, 2005.

von Glasow, R., Lawrence, M. G., Sander, R., and Crutzen, P. J.: Modeling the chemical effects of ship exhaust in the cloud-free marine boundary layer, Atmospheric Chemistry and Physics, 3, 233-250, 2003.

Wang, J., Cubison, M. J., Aiken, A. C., Jimenez, J. L., and Collins, D. R.: The importance of aerosol mixing state and size-resolved composition on CCN concentration and the variation of the importance with atmospheric aging of aerosols, Atmospheric Chemistry and Physics, 10, 7267-7283, 2010.

Whitby, E. R., and McMurry, P. H.: Modal aerosol dynamics modeling, Aerosol Science and Technology, 27, 673-688, 10.1080/02786829708965504, 1997.

Williams, A., Jones, J. M., Ma, L., and Pourkashanian, M.: Pollutants from the combustion of solid biomass fuels, Progress in Energy and Combustion Science, 38, 113-137, 10.1016/j.pecs.2011.10.001, 2012.

Wiinikka, H., Gebart, R., Boman, C., Bostrom, D., Nordin, A., and Ohman, M.: High-temperature aerosol formation in wood pellets flames: Spatially resolved measurements, Combustion and Flame, 147, 278-293, 10.1016/j.combusflame.2006.08.009, 2006.

Woo, J. H., Streets, D. G., Carmichael, G. R., Tang, Y. H., Yoo, B., Lee, W. C., Thongboonchoo, N., Pinnock, S., Kurata, G., Uno, I., Fu, Q. Y., Vay, S., Sachse, G. W., Blake, D. R., Fried, A., and Thornton, D. C.: Contribution of biomass and biofuel emissions to trace gas distributions in Asia during the TRACE-P experiment, Journal of Geophysical Research-Atmospheres, 108, 2003.

Zaveri, R. A., Easter, R. C., Fast, J. D., and Peters, L. K.: Model for Simulating Aerosol Interactions and Chemistry (MOSAIC), Journal of Geophysical Research-Atmospheres, 113, 10.1029/2007jd008782, 2008.

Zaveri, R. A., Barnard, J. C., Easter, R. C., Riemer, N., and West, M.: Particle-resolved simulation of aerosol size, composition, mixing state, and the associated optical and cloud condensation nuclei activation properties in an evolving urban plume, Journal of Geophysical Research-Atmospheres, 115, D1721010.1029/2009jd013616, 2010.

Tables

Table 1. Range of initial conditions and plume parameters analyzed to determine sensitivity. The "Illustrative Case" is a simulation used to present the general features observed in the plume evolution.

Parameter	**Scenarios**	**Illustrative Case**
Initial hygroscopicity	κ_0 = 0.004 (ponderosa pine), κ_0 = 0.11 (chamise), κ_0 = 0.20 (palmetto)	κ_0 = 0.004
Initial CMD and GSD	CMD_0 = 25, 50, 100, 300 nm GSD_0 = 1.1, 1.3, 1.6	100 nm 1.3
EF_{PM}	2, 4, 8, 12 g/kg	4 g/kg
Dilution rate	$\alpha = \beta$ = 0.5, 0.7, 1.0	0.7
SVOC volatility	SVOC1 (saturation vapor pressure[1] = 4.0×10^{-6} Pa) or SVOC2 (saturation vapor pressure[1] = 1.2×10^{-4} Pa)	SVOC1
SVOC emission factor (EF_{SVOC})	0 (no SVOCs), 5.62 g/kg	5.62 g/kg
Initial aerosol distribution	Unimodal or bimodal distribution	Unimodal
Initial mixing state	External mixture of OC, BC, and ammonium sulfate, or internally mixed	Internal mixture

[1]saturation vapor pressure at 298 K

Table 2. Initial composition of aerosols emitted from the combustion of three fuels, from Lewis et al. (2009), and the corresponding volume-average hygroscopicity parameter κ (Petters and Kreidenweis, 2007). OC specified here is assumed to be non-volatile.

Component	Mass Fraction [%]		
	Ponderosa Pine	Chamise	Palmetto
OC	97.8	48.8	42.8
BC	1.2	27	4.4
SO_4	0.25	12.1	1.32
NO_3	0.25	1.21	0
Cl	0.25	4.84	33
NH_4	0.12	0	13.2
K	0.1	6.05	2.64
Na	0.03	0	2.64
κ_o	0.004	0.11	0.20

Table 3. Emission factor of plume gases

Gas	Emission Factor [g/kg]	Reference
CO_2	1626	Akagi et al. (2011)
NO_x (as NO_2)	2.04	Christian et al. (2010)
CO	42	Akagi et al. (2011)
NH_3	0.947	Akagi et al. (2011)
SO_2	0.57	Burling et al. (2010)
HCl	0.139	Burling et al. (2010)
CH_4	2.32	Akagi et al. (2011)
SVOC1, SVOC2	0, 5.62	Akagi et al., (2011)

Table 4. EI_{CCN} [kg^{-1}] at s_{sat} of 0.7% for scenarios with CMD_0 = 25, 50, 100, and 300 nm (*i.e.*, CMD_{325} = 60, 78, 111, and 304 nm), and κ_0 = 0.004, 0.11, and 0.2 (κ_{325} = 0.02, 0.13, and 0.25), and no co-emitted SVOCs.

EI_{CCN} at a s_{sat} of 0.7% (x 10^{15})			
	κ_0		
CMD_0 [nm]	0.004	0.11	0.2
25	1.05	5.73	7.44
50	1.86	6.54	7.84
100	2.57	3.46	3.14
300	0.21	0.17	0.15

Table 5. Median critical supersaturation ($ssat_{50}$) from simulations with EF_{PM} of 2, 4, or 8 g/kg, and EF_{SVOC} of 0, 3, 5.62, and 10 g/kg. An initial size of CMD_0 of 25 nm was used to model a high coagulation rate.

$ssat_{50}$ [%]				
	EF_{SVOC} [g/kg]			
EF_{PM} [g/kg]	0	3	5.62	10
2	>1	0.65	0.48	0.36
4	>1	0.64	0.48	0.38
8	0.91	0.63	0.49	0.38

Figures

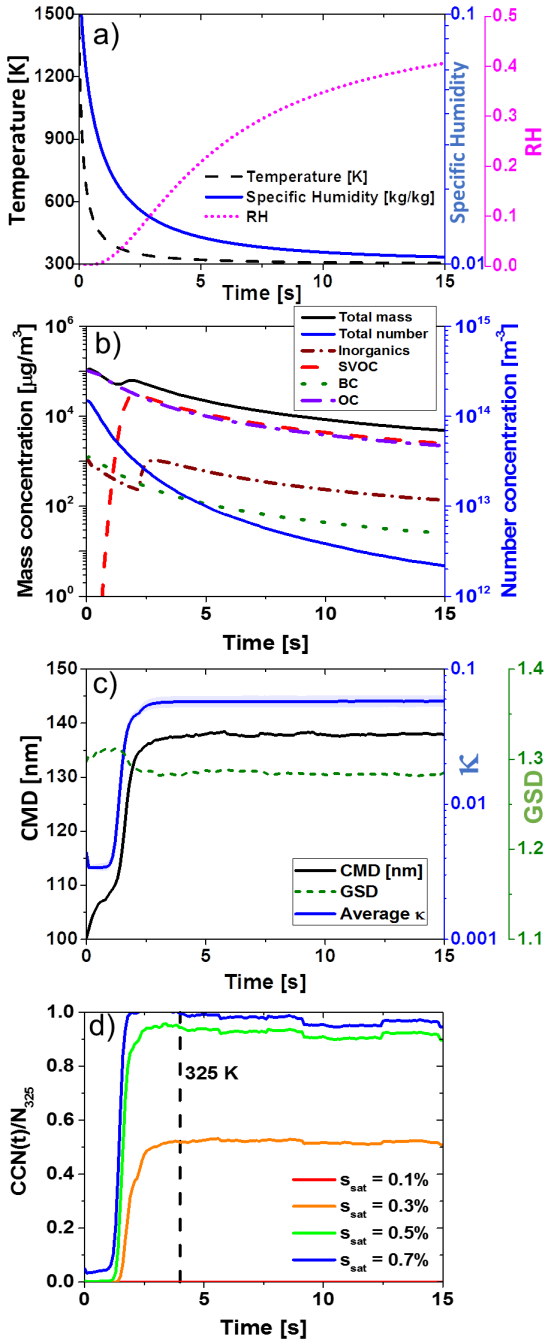

Figure 1. a) Prescribed profiles of specific humidity (left axis) and temperature (right axis). From these profiles, PartMC-MOSAIC calculates the plume RH (right axis). Time series of b) mass concentration of plume aerosol species (left axis) and number concentration (right axis), c) CMD (left axis), GSD and the average κ of all plume particles (right axis). The shaded area in κ is one standard deviation from the average. d) CCN(t)/N_{325} for s_{sat} of 0.1, 0.3, 0.5, and 0.7%. The vertical black line highlights when the plume temperature is 325 K. Although we modeled the first 30 seconds, we present results until the plume reaches ambient temperature and RH (plume-exit), *i.e.*, t = 15 s.

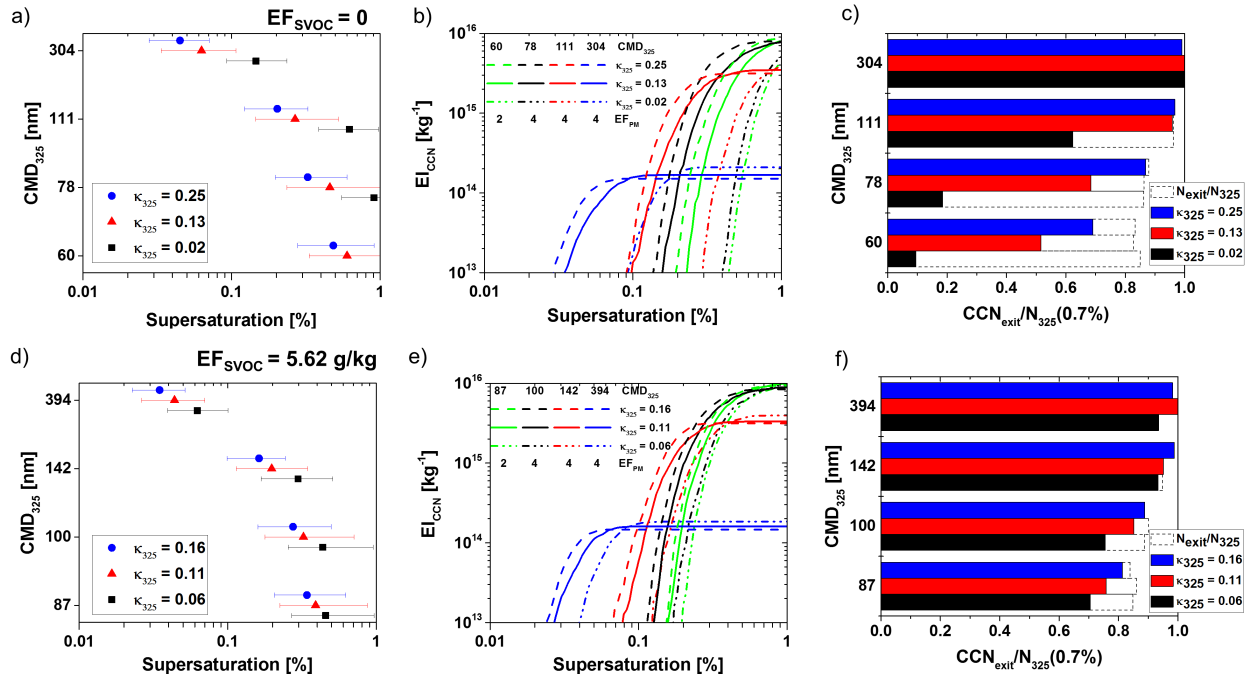

Figure 2. (a) Critical supersaturation of particle populations ($ssat_5$, $ssat_{50}$, and $ssat_{95}$), (b) EI_{CCN}, and (c) CCN_{exit}/N_{325} at s_{sat} of 0.7% for four different initial sizes (CMD_0 = 25, 50, 100, and 300 nm) and compositions (κ_0 = 0.004, 0.11, and 0.20). Labels show CMD and κ at 325 K. No SVOCs are co-emitted (EF_{SVOC} = 0). Figures (d), (e), and (f) show the same scenarios but for EF_{SVOC} = 5.62 g/kg. The scenario with CMD_0 = 25 nm uses EF_{PM} of 2 instead of 4 g/kg to achieve smaller CMD_{325} at plume exit.

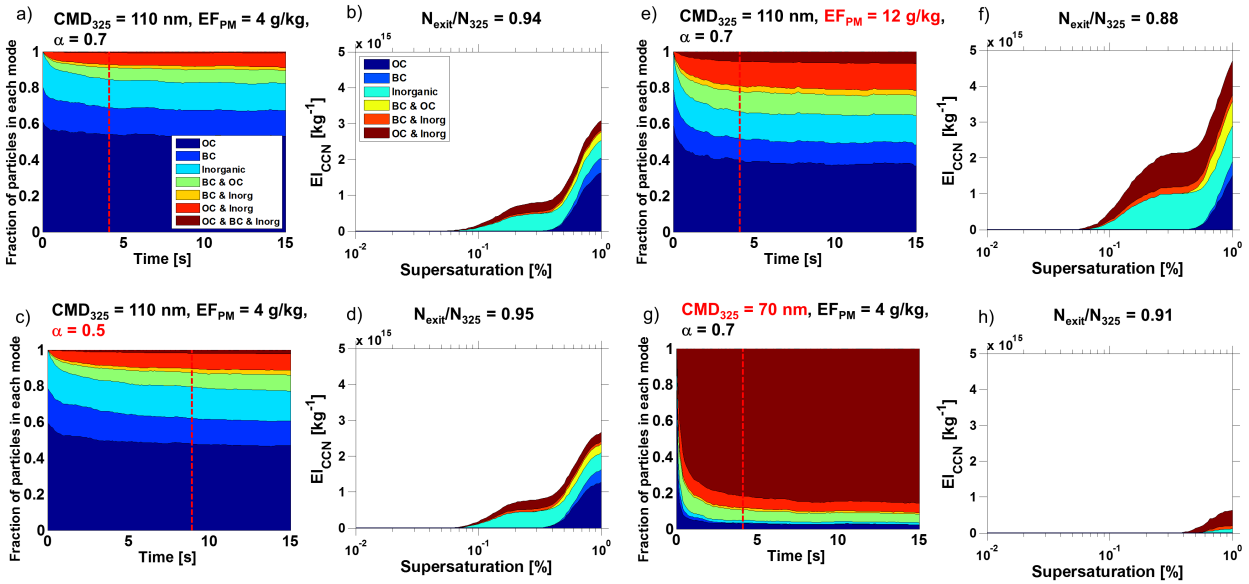

Figure 3. Fraction of particles in each mode (OC, BC, inorganic, or coagulated) as the plume evolves, showing how different initial conditions affect the coagulation between modes in an external mixture. a) Scenario with CMD_0 of 100 nm and GSD_0 of 1.3, EF_{PM} of 4 g/kg, α of 0.7, and no SVOCs. The other figures are the same scenario modified with (c) slower dilution (α = 0.5), (e) EF_{PM} of 12 g/kg, or (g) CMD_0= 25 nm (CMD_{325}= 70 nm). The vertical red line highlights when the plume temperature is 325 K. Figures (b), (d), (f), and (h) are the corresponding EI_{CCN} graphs to scenarios (a), (c), (e), and (g), respectively.

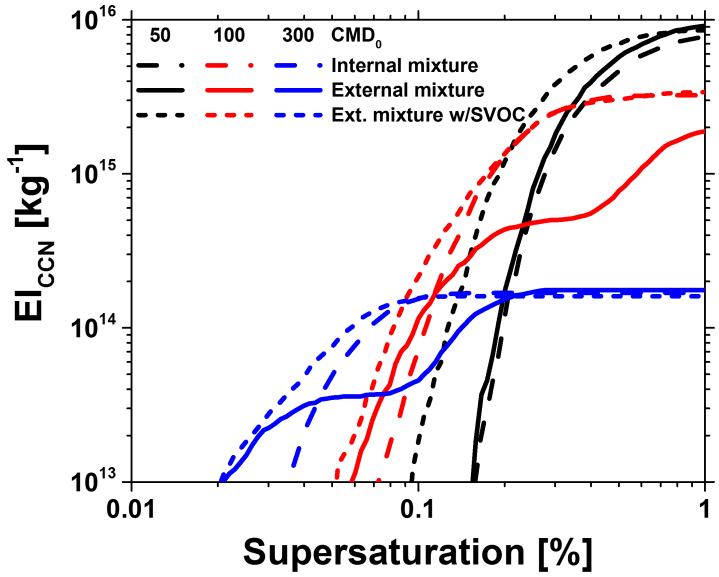

Figure 4. EI_{CCN} for different initial mixing states and initial CMD_0 of 50 nm (black), 100 nm (red), or 300 nm (blue). In the internal mixture case (dashed lines) all particles have the same initial composition, and no co-emitted SVOCs. The external mixture scenarios (solid lines) have an initial composition of three modes (OC, BC, and inorganic) with the same mass fraction as in the internal mixture, and no co-emitted SVOCs. The dotted line is the same external mixture scenario but now with co-emitted SVOCs (EF_{SVOC} = 5.62 g/kg).

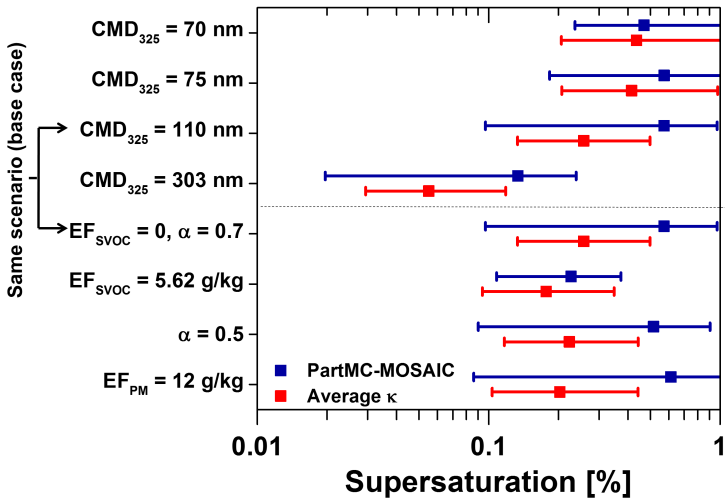

Figure 5. Critical supersaturation of particle populations ($ssat_5$, $ssat_{50}$, and $ssat_{95}$), calculated with either the particle composition from PartMC-MOSAIC (blue), or an average κ for all plume particles (red). The arrow highlights a "base case" simulation, *i.e.*, an external mixture with EP_{PM} of 4 g/kg, CMD_{325} of 110 nm, α = 0.7, and EF_{SVOC} = 0. All other cases shown here are variations of this base case, obtained by changing one of the parameters as indicated in the labels. The horizontal dotted line separates scenarios testing the sensitivity to initial size (above), or SVOCs, dilution rate, or EF_{PM} (below).

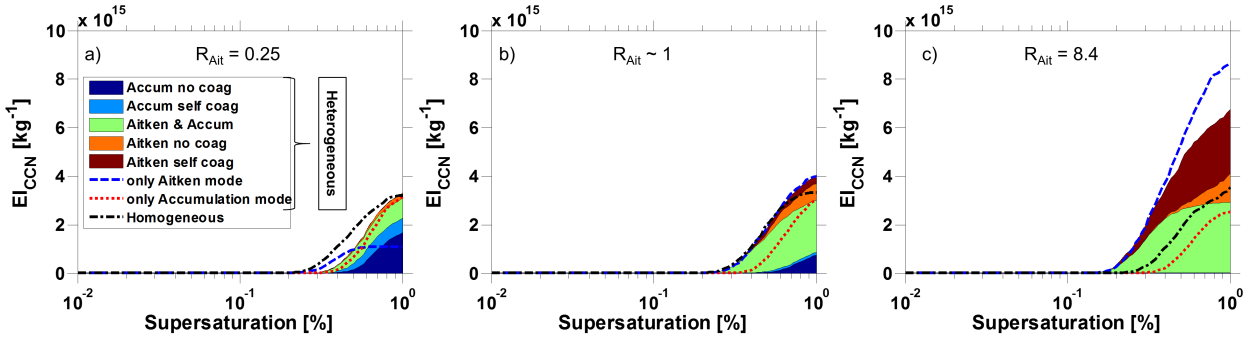

Figure 6. EI_{CCN} for three different $R_{Ait} = N_{0.Ait}/N_{0,Acc}$ values. The scenario with R_{Ait} ~ 1 has $N_{0,Aitken}$ = 1.6x10^{14} m^{-3} and $N_{0,Acc}$ = 1.2x10^{14} m^{-3}. The colored area corresponds to a heterogeneous bimodal distribution, each color describing the source of the particle that is CCN-active at plume exit. The label *'self coag'* refers to particles that have coagulated only with particles from the same mode. *'no coag'* refers to particles that have not coagulated with any other particle type. The dashed blue and red lines correspond to a repetition of the simulation but with either the accumulation or Aitken mode removed, respectively. The black line corresponds to a homogeneous bimodal distribution, using the same R_{Ait} values.

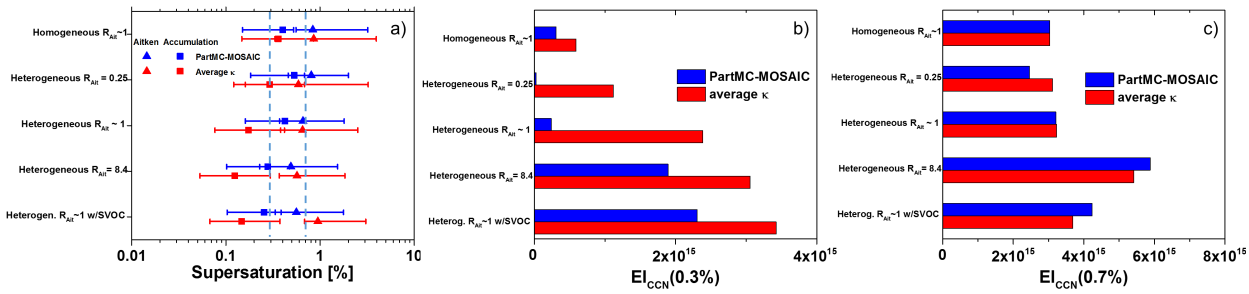

Figure 7. a) $ssat_5$, $ssat_{50}$, and $ssat_{95}$ of homogeneous and heterogeneous bimodal distributions with different R_{Ait} values, calculated separately for the Aitken mode (triangles) and accumulation mode (squares). Calculations were made with either the composition from PartMC-MOSAIC (blue), or using an average κ for all particles (red). The vertical blue lines highlight s_{sat} of 0.3% and 0.7%. b) EI_{CCN} for the same scenarios for s_{sat} of 0.3%, and (c) s_{sat} of 0.7%.

Appendix F

Implementation of the volatility basis set (VBS) approach into PartMC-MOSAIC to simulate the chemical aging of primary organic aerosol

Journal article: J. Ching, J. Tian, N. Riemer, J. Fast, M. Srivastava, and R. Zaveri. Particle-resolved modeling and measurements of aerosol mixing state during CARES, 2017, in preparation for Atmos. Chem. Phys.

As part of this project, we implemented the "volatility basis set" framework in the particle-resolved box model PartMC-MOSAIC. The implementation follows the approach by Srivastava et al. (2011) and is described in detail in Tian (2016). Instead of treating primary organic aerosols (POA) as non-volatile and non-reactive, we now classify POA into nine volatility bins by assuming that they are semi-volatile and the evaporated gas phase species can undergo further oxidation to form secondary organic aerosols (SOA). This approach can increase the level of SOA concentration, which is usually underestimated in existing aerosol models. The contribution of this work is to extend the capability of PartMC-MOSAIC on simulating aging of organic aerosols, including, but not limited to, biomass burning aerosol. While most previous studies only focused on the bulk concentration of SOA production, the new model capability uniquely provides particle-level information and mixing state of SOA-containing particles.

The updated PartMC-MOSAIC model with VBS framework was applied to the simulations of air trajectories obtained from the CARES field campaign conducted in California in June 2010. A blend of measurement and model data were used as input to setup the case studies. We also adjusted the POA emissions to consider the semi-volatile nature of POA. We then conducted model simulations on five air trajectories from CARES campaign on June 15, 2010.

The results were compared to the aircraft measurement for gas and aerosol mass concentrations and aerosol number concentrations. For a representative trajectory starting at 10 am local time at T0 in Sacramento, PartMC-MOSAIC was able to simulate gas and aerosol concentrations at similar levels compared to the observational data. Moreover, the simulation with VBS enabled produced additional 2 μg m^{-3} of SI-SOA which brought the total OA concentration closer to the observed values, as shown in the figure below.

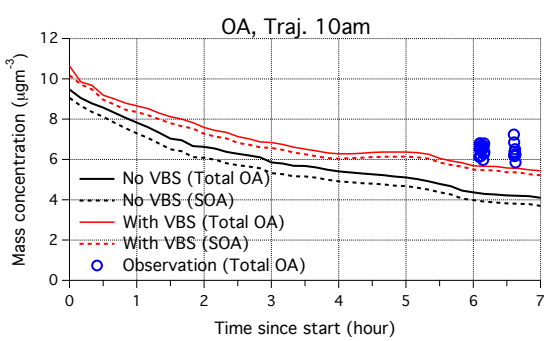

Figure 1: Evolution of the mass concentration of total organic aerosol. The trajectory started at 10am in Sacramento.

References

M. Shrivastava, J. Fast, R. Easter, W. I. Gustafson, Jr., R. A. Zaveri, J. L. Jimenez, P. Saide, and A. Hodzic. Modeling organic aerosols in a megacity: comparison of simple and complex representations of the volatility basis set approach. Atmos. Chem. Phys., 11(13):6639–6662, 2011. DOI: 10.5194/acp-11-6639-2011.

J. Tian, Investigation of the evolution of atmospheric particles with integration of the stochastic particle-resolved model PartMC-MOSAIC and atmospheric measurements, Ph.D. Thesis, 2016, http://hdl.handle.net/2142/90588